THE GlueX LEAD-SCINTILLATING FIBRE ELECTROMAGNETIC CALORIMETER

A Thesis
Submitted to the Faculty of Graduate Studies and Research
In Partial Fulfillment of the Requirements
For the Degree of
Doctor of Philosophy
In
Physics
University of Regina

by
Blake D. Leverington
Regina, Saskatchewan
June, 2010

Abstract

The work that comprises this thesis focuses on the design and performance of the electromagnetic barrel calorimeter for the GLUEX experiment. The calorimeter is designed to measure photon four-momenta for energies from a few tens of MeV up to 4 GeV.

Monte Carlo simulations were done to study the effects of the internal geometry of the lead/scintillating fibre matrix on the energy resolution and energy sampling fraction of the calorimeter.

The Monte Carlo work was congruent with a photon beam test at Jefferson Lab where the energy and time difference resolutions, and the number of photoelectrons produced, were measured for a prototype module. The results of the beam test are presented herein.

The attenuation lengths of PHT-044 and BCF-20 scintillating fibres were extracted from measurements of the optical spectra at multiple positions along the length of the fibre. The bulk attenuation lengths were then estimated based on the quantum efficiencies of a conventional photomultiplier tube and a prototype solid-state silicon photomultiplier.

A prototype acrylic light-guide was designed to meet the requirements of transmitting light from the fibres in the barrel calorimeter to the large area silicon photomultipliers. Studies of the efficiency and transmission angles are presented.

Using the data gathered from stand-alone Monte Carlo, simulations, and measurements of readout detector properties, the results were used as parameters for a larger detector simulation, HDGEANT, which contains all the other detectors within GLUEX. Studies of the reconstruction efficiency and resolutions for single photons are presented.

To conclude the thesis work, a first attempt was made at reconstructing a physics reaction with a recoil proton and four photons from meson decays using the kinematic fitter that is part of the GLUEX reconstruction software package. A point was made to determine the hadronic background which may be included in the signal reconstruction. The process of producing the signal and background are discussed with some initial analysis of the results. As the reconstruction software is not a final version, some deficiencies were found and are discussed.

Acknowledgements

Dedication

This thesis is dedicated to my parents who taught me that "if you are

going to do something, try to do it right the first time."

And to my friends, who won't call me Doctor, because they know me

too well.

Contents

List of Figures

List of Tables

Chapter 1

Introduction

In the study of the physics of the universe, it has been shown that there exist four fundamental forces that act on the constituent matter of the universe. These forces behave in their own distinct ways but have similarities in their interactions with matter, aside from gravity, and are well described by the Standard Model of Elementary Particle Physics [1]. Among these, quantum electrodynamics (QED), which describes the interaction of light and matter, combined relativity and quantum theory. It was a great success in the early half of the 20th century in that it described the interaction of photons and electrons (and other charged particles) with the electric field to better than one part in a billion. Subsequent success with the unifying of QED at higher energies with the weak nuclear force, which describes radioactive decays, resulted in the modern electro-weak theory. As such, QED has become the model for the strong interaction which describes quarks and gluons, the fundamental constituent particles of hadrons and mesons, called quantum chromo-dynamics (QCD).

At present, our understanding of strong interactions is described by a non-Abelian gauge field theory which we call QCD [2–4], though we know little about the physical states of the theory. Until we can compare the properties of the physical states of

the theory to those seen in experiment, it is difficult to say, as a physics community, that we fully understand QCD[1]. Fortunately, we do have a good system for studying QCD in the non-perturbative regime: the mesons. They offer an ideal mechanism for studying the strong interactions of quarks and the gluons that bind them.

Current theoretical understanding of hadron physics is generally derived from phenomenological models, and in particular, the constituent quark model [5,6]. The constituent quark model describes meson and baryon spectroscopy quite well, by treating these as objects made of constituent objects, otherwise referred to as valence quarks. Hadrons constructed with only valence quark configurations are referred to as "conventional". This is done as many QCD models predict hadronic states with explicit gluonic degrees of freedom, usually in addition to the valence quark degrees of freedom, and are *not* "conventional". States that consist of only gluonic fields and no constituent quarks are called *glueballs*. States that consist of both constituent quarks and excited gluonic degrees of freedom are called *hybrids*. Hybrids are the focus of the GLUEX experiment.

1.1 GlueX Physics

1.1.1 Quarks and Gluons in the Standard Model

Within the standard model, hadronic states are described by the interactions of spin-1/2 fermions, called quarks, and spin-1 bosons, called gluons. There are many ways to group the six quarks that have been discovered so far. They can be separated individually as "flavours" with the common names up (u), down (d), strange (s),

---

[1]QCD is well understood in the dynamical asymptotic region of perturbative QCD. However, in the non-perturbative region, specific components of the QCD Lagrangian prevent analytical solutions.

charmed (c), top (t) and bottom (b). These can then be grouped into light flavours (u, d, s) and heavy (c, t, b), in respect to their constituent quark masses. The quarks carry electrical charge like the electron and are subject to QED but also possess a colour charge, a property of the strong interaction. This colour charge has three values commonly denoted 'red', 'blue' and 'green' in analogy to colour in optics. Where photons[2] are the field carriers of the electromagnetic interaction, gluons are the field particles of the strong interaction. Gluons are massless, flavourless, vector bosons which are defined to carry both a colour and anti-colour charge. Also, colour charge is not directly observable as only colour singlet[3] combinations of colour charged objects have been seen to exist experimentally though this is not a fundamental property of QCD. Since gluons carry colour charge, they can interact strongly with other gluons. This self-interaction of the gluons is the driving mechanism for glueballs and hybrids.

1.1.2 Lattice QCD

Lattice quantum chromodymanics (LQCD) is QCD formulated on a regular Euclidean space time grid. The lattice is characterized by the lattice spacing, a, the distance between neighbouring sites. The major benefit of LQCD is that, since no new parameters or field variables are introduced in this discretization, LQCD retains the fundamental characteristics of QCD. The regularization of QCD on the lattice allows for non-perturbative features of the strong interaction to be studied, the original reason that Wilson introduced LQCD, which went on to show confinement of quarks in the strong coupling regime. As well, unlike certain phenomenological models, the only tuneable input parameters in LQCD are the strong coupling constant and the

---

[2]Photons are massless neutral vector bosons. Because they are neutrally charged, they do not interact with other photons.

[3]A colour singlet refers to the state where there is no net colour charge and is colourless. (i.e. red + anti-red = colourless, or red + blue + green = colourless).

bare masses of the quarks[4]. Since these quantites can be determined from experiment and used as inputs to LQCD, any predictions made by LQCD must match experimental data if QCD is the theory of strong interactions. One drawback of LQCD is that the discretization of the lattice spacing induces a cutoff on the momenta on the order $1/a$, and therefore extrapolations to the continuum must be made to estimate real values. Computer resources generally limit the lattice spacing and, as such, calculations are generally made with heavy quarks and/or large pion masses. However, ongoing improvements in computer development will allow for further reductions of the lattice spacing and pion mass. Good reviews of LQCD and its successes and problems are found in Refs. [7] and [8].

1.1.3 $q\bar{q}$ Meson and Baryon Symmetries

Ignoring the three heaviest quarks, the three lightest quarks (u, d, s) will form an $SU(3)_f$ symmetry group[5] [6]. The result of this symmetry is that the dimensionalities of the combinations of quarks may be determined. In an $SU(3)_f$ symmetric description of quarks, a quark is denoted as 3 for $(u, \ d, \ or \ s)$ and an anti-quark as $\tilde{3}$ for $(\bar{u}, \ \bar{d} \ or \ \bar{s})$. In the case of baryons, a combination of three constituent quarks, the dimensionalities of the states are given by

$$3 \otimes 3 \otimes 3 = 1 \oplus 8 \oplus 8 \oplus 10 \tag{1.1}$$

where a singlet state (1), two octets (8) and a decuplet (10) should all be observed. Initially, Gell-Mann and Zweig had independently postulated a model where three

---

[4]One of the important features of LQCD is that in addition to testing QCD it can make detailed predictions of the dependence of quantities on α_s and the quark masses. These predictions can then be used to constrain effective theories like chiral perturbation theory, heavy quark effective theory, and various phenomenological models.

[5]The f denotes flavour symmetry.

constituents with an $SU(3)_f$ symmetry explained the observed spectra of hadrons. This led to the search for the $\Omega^-(sss)$ to fill the decuplet and it was a major success for the quark model when it was found experimentally [9].

In the case of mesons, a quark and anti-quark pair, the dimensionality of states is given as

$$3 \otimes 3 = 1 \oplus 8 \tag{1.2}$$

A quark (q) and anti-quark ($\bar{q}$) will form a singlet state (1) or an octet (8). This combination is collectively referred to as a nonet. A nonet is characterized by the quantum numbers J^{PC} which are determined by the rules for adding the quarks' spins ($\vec{S_q}$) to their relative orbital angular momenta ($\vec{L}$). Thusly, $\vec{J} = \vec{L} + \vec{S}$ where $\vec{S} = \vec{S_q} + \vec{S_{\bar{q}}}$. The parity, P, for this $q\bar{q}$ system is given by $(-1)^{L+1}$ and the charge conjugation (*C-Parity*), C, which is defineable only for neutral self-conjugate mesons, where $C = (-1)^{L+S}$. These rules for spin, angular momentum and parity restrict the available J^{PC} states through quark degrees of freedom only. Allowed conventional J^{PC} states are in the set $\{0^{-+}, 0^{++}, 1^{++}, 1^{+-}, 1^{--}, \dots\}$. States such as $\{0^{--}, 1^{-+}, \dots\}$ cannot be constructed solely from a $q\bar{q}$ pair and are said to be *exotic*.

1.2 Non-$q\bar{q}$ Mesons

Mesons that consist of more than conventional $q\bar{q}$ states are predicted by QCD models [1, 10–16]. The non-$q\bar{q}$ meson states are characterized by their different quark and gluon configurations; these are classified as glueballs (made primarily of gluons), multi-quark states and hybrids which have both valence quarks and gluonic degrees of freedom.

1.2.1 Glueballs

While glueballs will not be seen in the GLUEX experiment, it is important to discuss them briefly for the sake of completeness. From the gluon's self-interaction due to carrying colour charge, bound quark-less states are formed: the glueballs. The glueball is predicted by many different QCD models: bag models [13, 17, 18], constituent glue models [19], flux tube models [20–22], QCD sum rules [23] and lattice gauge theory (LGT). It is expected that lattice calculations will provide the best predictions for glueball states as these calculations originate from QCD itself.

Since gluons have colour symmetry $SU(3)_c$ and only colour singlet states have been observed to exist as free particles, any possible glueball must consist of at least two valence gluons (in the sense that hadrons consist of valence quarks) such that the net colour of the state is colourless.

The previously stated models predict the mass of the lightest glueball, a 0^{++} state, to lie between 1500 MeV and 1700 MeV [24–27]. The next lightest states, 0^{++} and 2^{++}, have mass estimates between 2000 MeV and 2500 MeV [24, 25, 28]. These light glueballs have non-exotic J^{PC} quantum numbers and, as such, make it difficult to separate them from standard $q\bar{q}$ mesons. Glueballs with exotic quantum numbers are expected to have masses above 3–4 GeV. The glueball spectrum is graphed in Fig. 1.1.

A proposed method to isolate the glueball is to study glueball decays having quark-flavour symmetric couplings to final state hadrons. These "flavour-blind", decays produce a characteristic flavour-singlet branching fraction to pseudoscalar pairs which can be experimentally measured [29]. In addition, a measurement of the electromagnetic coupling to glueball candidates would provide clues about the nature of the state. Radiative transition rates of a relatively pure glueball would be
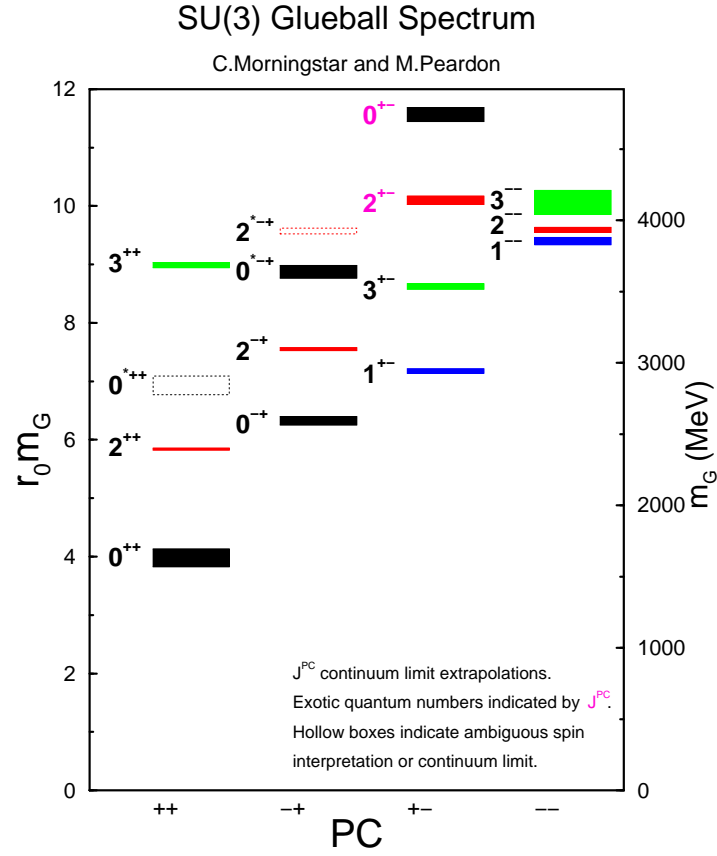
Figure 1.1: The mass of the glueball states. The scale is set by r_0 with $1/r_0 = 410(20)$ MeV. Figure from [27]. *(original in colour)*

quite different from that of conventional $q\bar{q}$ states, with glueballs having a suppressed coupling to $\gamma\gamma$. However, everything is rendered more complicated by the possibility that any glueball state could be a mixture of underlying states with the same quantum numbers which significantly affects the properties of the state [30]. This leads to inherent difficulties and controversy when interpreting various observed states.

1.2.2   Hybrids

The simple description of the hybrid meson is a quark anti-quark pair with an additional gluonic degree of freedom. Compared to glueballs, hybrids have a few additional features that makes their detection much easier. Not only do they cover complete flavour nonets, the lightest hybrid multiplet $J^{PC} = \{2^{+-},\ 1^{-+},\ 0^{+-},\ 0^{--}\}$ contains at least one hybrid meson with exotic J^{PC} quantum numbers forbidden in conventional $q\bar{q}$ states, the 1^{-+}. This gives a much larger field to explore experimentally than glueballs.

Hybrids can be sought in an over-population of states compared to those predicted by the quark model. However, this depends on a good model to predict the population of conventional quark states and a good understanding of hadron spectroscopy in a specific mass region. Currently, the phenomenological models have not been tested well enough against experiment to reliably exclude a given state as "conventional", due to the lack of experimental data on hybrid mesons. Further complicating this search is the expected mixing between hybrid and conventional states. A second approach is to search for hybrid mesons that do not have the same J^{PC} quantum numbers as conventional $q\bar{q}$ mesons. A discovery of exotic hybrid mesons would be key evidence for hadron spectroscopy beyond the simple quark model.

Insight into the physics of hybrids can be gleaned from the heavy-quark results of

lattice QCD [31]. In lattice calculations, the quark and anti-quark are spatially fixed colour sources with the energy level of the glue determined by the quark separation. Potentials are determined by the gluon energy level and can be calculated from lattice QCD. The ground state potential corresponds to the glue being symmetric along the quark anti-quark axis. The lowest lying gluonic excitation corresponds to one unit of angular momentum along the quark-antiquark axis. Thus, conventional mesons are based on the lowest lying potential when there is no excitation of the glue, and hybrid states emerge from the the excited potentials. The combinations of the excited flux tubes ($J^{PC} = 1^{+-}$ and 1^{--}) with the quark and antiquark spins produce a set of eight degenerate hybrid states with $J^{PC} = \{1^{--}, 0^{-+}, 1^{-+}, 2^{-+}\}$, and $\{1^{++}, 0^{+-}, 1^{+-}, 2^{+-}\}$, respectively. Among these, the $J^{PC} = \{1^{-+}, 0^{+-}, 2^{+-}\}$ states are exotic. The degeneracy is expected to be broken by differences in excitation energies of $J^{PC} = 1^{+-}$ (magnetic) and 1^{-+} (pseudo-electric) gluonic excitations, spin-orbit terms as well as by mixing between conventional and non-exotic hybrid mesons. While it may be reasonable to extend this picture to the light quark masses, it must be taken into account that these lattice calculations work well only for heavy quarks and decidedly less so for the light quark sector where relativistic effects are more predominant. The bag model [13, 14, 18, 32, 33] also predicts hybrid mesons but only predicts four degenerate states, $\{2^{-+}, 1^{-+}, 1^{--}$, and $0^{-+}\}$. This is due to the inherent differences between the two models.

Exotic hybrid mesons have been experimentally elusive. One reason why this may be is that there appears to be a selection rule for hybrid mesons: that gluonic excitations cannot transfer angular momentum to the final states as relative angular momentum and must instead appear as internal angular momentum of the $q\bar{q}$ pair [34–36]. However, this rule does not appear to be absolute, with the flux tube,

constituent glue and bag models allowing certain cases[6] where it is broken. Another possible explanation is that hybrids may not couple strongly to simple final states. For example, the hybrid ρ meson ($\hat{\rho}$) decays predominantly through $b_1\pi$ and $f_1\pi$ modes. Its decay into two pseudoscalars, $\hat{\rho} \to \pi\eta$ or $\hat{\rho} \to \pi\eta'$, provides a unique signature for the 1^{-+} state.

1.2.3 Masses and Widths

The flux tube model predicts [22,37] that many hybrids (or their final state mesons) have too broad a resonance to be observed, with only a few hybrids narrow enough to be easly observed. The $\hat{a_0}, \hat{f_0}, \hat{f_0'}$ hybrids are too broad themselves while the $\hat{\omega}_1$ and $\hat{\phi}_1$ will most likely be too difficult to find due to the width of their final state decays. From flux tube model predictions, the hybrids that should be easiest to find are:

$$
\begin{aligned}
\hat{\rho}_1 &\to [b_1\pi]_S & (\Gamma \approx 150 \text{ MeV}) \\
&\to [f_1\pi]_S & (\Gamma \approx 50 \text{ MeV}) \\
\hat{a}_2 &\to [a_2\pi]_P & (\Gamma \approx 200 \text{ MeV}) \\
\hat{f}_2 &\to [b_1\pi]_P & (\Gamma \approx 250 \text{ MeV}) \\
\hat{f}_2' &\to [K^*(1430)_2\bar{K}]_P & (\Gamma \approx 90 \text{ MeV}) \\
&\to [\bar{K}K_1]_P & (\Gamma \approx 100 \text{ MeV})
\end{aligned}
$$

One of the earliest predictions for hybrids comes from the flux-tube model in which all eight hybrid nonets are degenerate with a mass of about $1.9\,GeV/c^2$. Lattice QCD calculations, however, regularly show that the exotic 1^{-+} nonet is the lightest.

---

[6]The rule can be broken by wave function and relativistic effects in the flux tube and constituent quark models while the bag model allows for an excited quark to lose its angular momentum to orbital angular momentum.

Table 1.1 lists predictions made previous to 2004, though lattice calculations are ongoing. The results fall in the range of 1.8 to $2.1\,GeV/c^2$ with an average similar to that of the flux-tube model. A more thorough discussion of hybrid masses is available in Ref. [38] and includes an extensive table of predicted hybrid mass widths. Predictions of photoproduction rates of hybrids by Close and Dudek are found in Ref. [39].

Author			1^{-+} Mass (GeV/c^2)	
Collab.	Year	Ref.	$u\bar{u}/d\bar{d}$	$s\bar{s}$
UKQCD	(1997)	[40]	1.87 ± 0.20	2.0 ± 0.2
MILC	(1997)	[41]	$1.97 \pm 0.09 \pm 0.30$	$2.170 \pm 0.080 \pm 0.30$
MILC	(1999)	[42]	$2.11 \pm 0.10 \pm (sys)$	
SESAM	(1998)	[43]	1.9 ± 0.20	
Mei& Luo	(2003)	[44]	$2.013 \pm 0.026 \pm 0.071$	
Bernard *et al.*	(2004)	[45]	1.792 ± 0.139	2.100 ± 0.120

Table 1.1: Lattice results for the light-quark 1^{-+} hybrid meson masses. This table is taken from Ref. [38].

The predictions for masses the mass of other exotic quantum numered states are few and far between. Using lattice QDC, Bernard [41] calculates the splitting between the 0^{+-} and the 1^{-+} state to be about 0.2 GeV/c^2 with large errors. They later calculate this with a clover action [42] and find a splitting of 0.270 ± 0.2 GeV/c^2. The SESAM collaboration [43] has also calculated masses for three exotic hybrids J^{PC} states on the lattice, the results of which are shown in Table 1.2.

J^{PC}	Mass
1^{-+}	$1.9 \pm 0.2\,GeV/c^2$
2^{+-}	$2.0 \pm 0.11\,GeV/c^2$
0^{+-}	$2.3 \pm 0.6\,GeV/c^2$

Table 1.2: Estimates of the masses of exotic quantum number hybrids. This table is taken from Ref. [38].

1.3 Hybrid Production

In the search for hybrid mesons, the production mechanism is as important as the final state detection. Similar to glueball searches, gluon rich environments like J/Ψ decays or $p\bar{p}$ annihilation are good places to look. Hadronic production via pion or kaon beams have been attempted, with some preliminary (if ambiguous) results [46–51]. Photoproduction is also an important mechanism, as hybrids could be produced at tremendous rates via off-shell ρ, ω or ϕ via vector meson dominance interacting with an off-shell exchanged π [52]. However, it should be noted that an experiment with a spin-0 beam (in the entry channel of the reaction), such as a pion beam, cannot produce an exotic signal directly (only through second order processes), though an experiment like GLUEX with a photon beam (spin-1) can. A hadronic beam would require a spin-flip of one of the quarks. In any case, a high statistics experiment is needed that can produce many of the possible exotic J^{PC} states.

1.3.1 Peripheral Production

Peripheral reactions are characterized by a large impact parameter (the distance of closest approach to the nucleus) and the square of the exchanged four-momentum, t, between the beam and the resonant state, X such that $t \equiv (p_{beam} - p_X)^2$. A diagram of the hadronic peripheral production process is shown in Fig. 1.2. Peripheral reactions, where a pseudoscalar meson (π, η, K) or vector meson (M) (ρ, ω, ϕ) is incident on a nucleon (B), will generally produce a resonance in the meson (M^*) or baryon (B^*) through the exchange of a meson with some small fraction of events producing a resonance in both the meson and baryon:

$$MB \quad \rightarrow \quad M^*B$$

$$MB \quad \rightarrow \quad MB^*$$

$$MB \quad \rightarrow \quad M^*B^*.$$

The non-resonant background is small. The cross sections for different exchanged particles in Fig. 1.2, as well as interferences between particular channels, show a strong dependence on t [53]. Therefore, analysis is typically done for different ranges of $-t$ to try to understand the exchange mechanism[7]. Reactions in GLUEX will generally have a small $-t$, less than 1 $(\text{GeV/c})^2$, where one pion exchange typically dominates.

Beam Particle   **X**   Decay products

Exchange particle

Target Nucleon   **Recoil Nucleon**
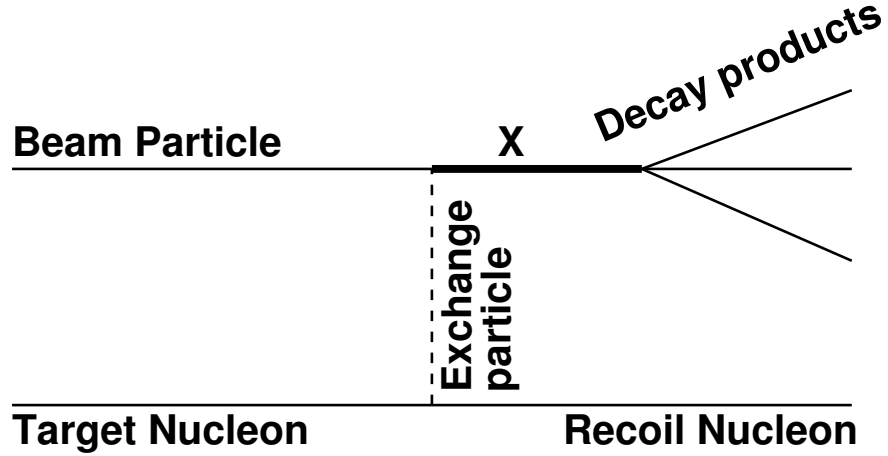
Figure 1.2: Schematic diagram of a hadronic peripheral production process. The exchange particle is an off-mass-shell particle, such as a π or a_1.

---

[7]The value of t is negative in the relativistic limit since mass can be neglected. Therefore, $t = -2p_{beam} \cdot p_X$.

1.3.2 Hadronic Production

The majority of data on light meson spectroscopy are from experiments with multi-GeV pion or kaon beams incident on nucleon or nuclear targets. The beam particle is excited in the interaction and exchanges momentum and quantum numbers with the recoiling nucleon. Most of the products of the interaction are mesons at forward angles with a ground- or exited-state baryon recoiling at at large angle. The E852 experiment [46], VES at IHEP/Serpukhov [47,48] and NENKEI at KEK [49,50] all used a π^- beam. LASS [51] had a K^- beam. An example reaction would have an excited meson state X, where its quantum numbers have been determined by the exchange, which subsequently decays into two or more stable mesons. In the case of E852, this would look something like $\pi^- p \to X^- p \to \rho^0 \pi^- p \to \pi^- \pi^+ \pi^- p$. Positively charged pion or kaon beams would also produce peripheral hadronic reactions. While hadronic beams have provided important data due to their high cross sections and availability, the hybrid spectrum has yet to be unambiguously identified, possibily due to the supression of hybrids in these channels.

1.3.3 Photoproduction

Peripheral photoproduction, however, appears to be a better production mechanism. Lattice QCD and phenomenological models argue that the hadronic properties of the photon will enhance the probability of producing hybrid mesons [54, 55]. However, there is a significant lack of data regarding the photo-production of data [56] in the mass regions where hybrids are expected to be produced. Almost all of what is known comes from bubble chamber measurements at SLAC [57–62].These experiments were among the first exploratory studies of the photoproduction of meson and baryon resonances at these energies, and although they suffer from low-statistics, they have

good acceptance, except for events with multiple neutrals. The absence of any new photoproduction data is due to the lack of quality, high intensity photons beams and a suitable experimental apparatus since then.

For about 70% of the total photoproduction cross section, from $E_\gamma = 7 \rightarrow 12$ GeV, there is very little information, and for multi-neutral states almost none exists [57]. Due to the usage of hydrogen-filled bubble chambers, the SLAC experiments in the late 1960's and early 1970's were unable to measure photons from decays of η and π^0 mesons, though a zero-constraint kinematic fit was applied to identify the missing mass from a single π^0 or neutron [63]. Nearly 85% of the total cross-section (124μb at $E_\gamma = 9.3$ GeV) is in the three, five or seven-prong[8] samples and of this sample, more than 60% have multi-neutrals (η, π^0 or neutron). Refs. [63, 64] summarize the the available photoproduction data relevant to GLUEX. Extrapolating from what is known from the final states that have been identified and studied, the bulk of the unknown processes are expected to involve final states with combinations of π^0 and η mesons. The discovery potential is likely to be highest in these multi-prong states. Table 1.3 summarizes the photoproduction cross sections for various charged particle topologies, with and without neutrals, at $E_\gamma = 9.3$ GeV [57]. Predictions of photoproduction rates of hybrids by Close and Dudek are found in Ref. [39].

1.3.4 Exotic Hybrids from Photoproduction

The hadronic properties of the photon are given by the *vector dominance* model [65]. The photon coupling to hadrons is that of a superposition of vector meson states. In this case, Fig. 1.2 still applies, but the incoming beam particle is now a spin *triplet* ground state, rather than the spin singlet state of the hadronic peripheral production

---

[8]A prong refers to the number of charged tracks in each reaction.

Topology	σ (μb)	% of σ with neutrals
1-prong	8.5 ± 1.1	100
3-prong	64.1 ± 1.5	76 ± 3
5-prong	34.2 ± 0.9	86 ± 4
7-prong	6.8 ± 0.3	86 ± 6
9-prong	0.61 ± 0.08	87 ± 21
With visible strange decay	9.8 ± 0.4	-
Total	124.0 ± 2.5	82 ± 4

Table 1.3: Topological photoproduction cross sections for γp interactions at 9.3 GeV from Ref. [57]. Also shown are the percent of the cross section with neutral particles for each topology.

case. As a consequence, the preferred excitations are likely to be much different, producing the 0^{+-} , 1^{-+} and 2^{+-} exotic meson states in the lowest excited state of the flux tube ($J^{PC} = 1^{+-}$ and 1^{--}). The suppression of these exotic hybrids in π-induced reactions is not surprising considering that a spin-flip of one of the quarks is required. Phenomenological studies quantitatively support this picture predicting that the photoproduction crossections for exotic mesons are comparable to those for copiously produced mesons such as the $a_2(1320)$ [55, 66].

1.3.5   The $\eta\pi^0$ system

The reaction $\gamma p \to \eta\pi^0 p$ is of particular interest for exotic hybrid searches since the $\eta\pi^0$ system has well-defined charge conjugation quantum value (C = +) and if the η and π^0 resonate in a P-wave then the resonance has an exotic $J^{PC} = 1^{-+}$. The branching fractions for decays to $\gamma\gamma$ for the η and π^0 are 39% and 99%, respectively. The detection of the photons from these decays are of great importance for the GLUEX experiment in searching for an exotic hybrid signal. For this reason, the calorimeters are emphasised in this work with studies of the BCAL dominating the majority of it. This decay channel is also the focus of physics reconstruction work presented in later chapters.

1.4   Partial Wave (Amplitude) Analysis

The extraction of quantum numbers for the physics of interest from data gathered by the GLUEX detector, will be accomplished using a method known as Partial Wave Analysis (PWA), which is sometimes more accurately referred to as Amplitude Analysis. PWA is a technique used in hadron spectroscopy to extract information about the spin-parity and decay properties of resonances produced in hadronic inter-

actions. For this type of analysis to be successful, a detector with good acceptance in phase-space is required, along with adaquate four-momentum resolution and good statistics such that the data can be binned in terms of mass and four-momentum transfer-squared, t.

PWA involves the parameterization of the intensity distribution in terms of variables that have physical meaning when interpreted as properties of intermediate states in a particular reaction. Any complete set of functions can be used, as long as they cover the appropriate phase-space, but some are much more complicated than others. For instance, a moment[9] analysis requires a complicated mapping from moments to physical states to understand the results in all but the simplest of cases. However, an expansion in terms of intermediate resonances and their decays is simpler where conservations laws limit the number of terms in the expansion and the results can be interpreted directly.

In any reference frame, where the z-axis is in the production plane, the most general angular distribution of the intensity of a resonant X system can be written, according to parity conservation, as a sum of the real parts of the spherical harmonic moments, $\Re(Y_l^m)$. In a moments analysis [67], the angular distribution of the produced events can then be written as

$$I(\tau) = \sum_{l=0}^{\infty} \sum_{m=0}^{l} t_l^m Y_l^m(\theta_{GJ}, \phi_{GJ}) \tag{1.3}$$

where t_l^m are the normalized moments, l is the angular momentum quantum number, m is the magnetic quantum number; t_l^m contains the angular momentum quantum number j and $\Re(Y_l^m)$ is just written as Y_l^m. The variable τ defines the phase space necessary to determine a configuration of the final state being investigated. Generally

---

[9]the influence that produces a change in a physical quantity

τ includes, the momentum transfer squared t, the invariant masses, and the polar and azimuthal angles in the Gottfried-Jackson frame[10].

The simpler expansion, based on work by of Chung [68] and Chung and Trueman [69] in terms of intermediate resonances, results in slightly different expression for the intensity distribution [70]:

$$I(\tau) \;=\; \sum_{\alpha} \left\{ \left| \sum_{\beta} {}^{\alpha}\psi_{\beta}(\tau) \right|^{2} \right\} \tag{1.4}$$

where one of the terms is squared to account for interference. Again, τ represents the phase-space. The subscripts α and β are the parameters that describe the partial wave decomposition being used, where α specifies the properties of the different intermediate states that do not interfere, such as the spin states of the incoming or outgoing particles in the detector. The subscript β, on the other hand, represents the properties whose differing values *do* interfere, such as the spin states of broad resonances produced as intermediate states in a sequential decay.

In a peripheral production experiment, the amplitudes in the expansion can be drawn as shown in Fig. 1.3. Following this diagram, the amplitude ${}^{\alpha}\psi_{\beta}(\tau)$ is factored into two parts: V, the amplitude to produce the state X, and A, the amplitude for the state X to decay into the final state observed.

These amplitudes are written in the reflectivity basis [69], which takes into account parity conservation in the production process by writing the amplitudes in terms of eigenstates of reflection through the production plane, where the reflectivity of the amplitude is denoted as ϵ. Waves of differing ϵ do not interfere. The spin configuration of the amplitudes is labeled k. Amplitudes with different relative spin

---

[10]The Gottfried-Jackson frame is the CM-frame of the X resonance rotated so that its z-axis is parallel to the incident photon beam direction.
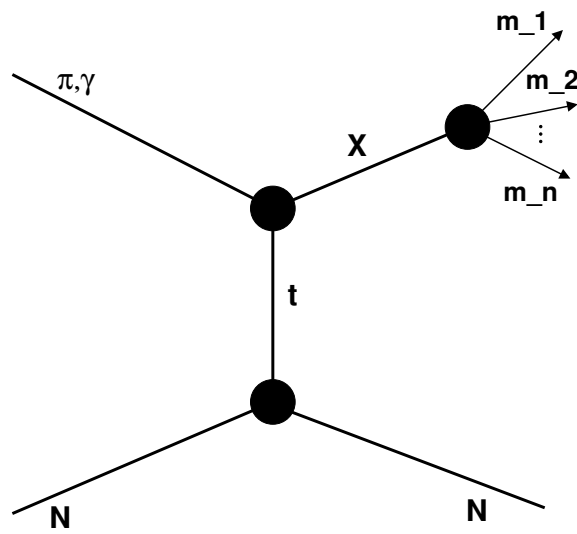
Figure 1.3: Diagram representing the amplitude $\psi_{\alpha\beta}(\tau)$.

configurations for the incoming and outgoing baryon will not interfere either. It can be seen from this that Amplitude Analysis is the more accurate name for this particular technique that GLUEX will use.

In the reflectivity basis, the sum over amplitudes splits into four non-interfering sets of fully interfering amplitudes [69], or $\alpha = \{\epsilon, k\}$. While both the production and decay amplitudes depend on ϵ, the decay amplitude does not depend on k, since the decay amplitude for a particular state X cannot depend on the nucleon spin during the production process. Similarly, the production amplitude has no dependence on τ, the configuration (phase-space) that the final state X decays into.

The intensity distribution now becomes

$$I(\tau) = \sum_{\epsilon,k} \left\{ \left| \sum_{\beta} {}^{\epsilon}V_{k\beta}{}^{\epsilon}A_{\beta}(\tau) \right|^2 \right\}. \tag{1.5}$$

where ${}^{\epsilon}A_{k\beta}(\tau)$ and ${}^{\epsilon}V_{k\beta}$ are the decay and production amplitudes, respectively, which are described by parameters such as J^{PC}, ϵ, orbital angular momentum, l, the spin of the isobar resonance, s, and its mass. The decay amplitudes can be calculated but the production amplitudes must be determined from a fit to data. This is done by examining an extended maximum likelihood of the fit, while varying the parameters in the production amplitude.

The maximum likelihood requires that the acceptance of the detector be understood for each of the phase-space parameters in the production amplitude. This requires a good Monte Carlo detector simulation, which accurately predicts the acceptance for these phase-space parameters. During the fitting process, the finite acceptance of the detector is taken into account on a term by term basis. (*i.e.*, each term contains a pair of decay amplitudes with a unique shape in τ, and the

acceptance for each term is determined separately.)

1.4.1 Unbinned Likelihood Fitting

Ref. [71] describes the likelihood fitting process as follows. In an experiment, N_d events will be detected where each event is described by a vector $\vec{x}_j^d$. In Monte Carlo, N_m events are generated over the appropriate phase-space, to determine the acceptance of the detector, where each event is described by the vector $\vec{x}_j^m$. The Monte Carlo events are passed though the detector simulation to determine the acceptance for each event, η_j, resulting in N_a accepted events. $\eta_j = 1$ for an accepted event and $\eta_j = 0$ otherwise. With the Monte Carlo and experimental data events, an amplitude hypothesis $I(\vec{\alpha}, \vec{x}_i)$ can be tested for the likelihood with which I fits the data. $\vec{\alpha}$ will be the parameters varied in the fit to maximize the likelihood.

The *standard* likelihood function is given as in Eq. 1.6 where p is a probability function:

$$L = \Pi_{i=1}^{N_d} p(\vec{x}_i^d).$$
(1.6)

p can be built from the physics hypothesis I, by normalizing I over all phase space:

$$p(\vec{\alpha}, \vec{x}) = \frac{I(\vec{\alpha}, \vec{x}_i)\eta_i}{\int I(\vec{\alpha}, \tau)\eta(\tau)d\tau}$$
(1.7)

The normalization integral can be computed via Monte Carlo techniques. The total phase space is defined as:

$$\Omega_{tot} = \int d\tau,$$
(1.8)

such that the normalization integral can be computed as:

$$\int I(\vec{\alpha}, \tau)\eta(\tau)d\tau \;\; = \;\; \frac{\Omega_{tot}}{N_m}\sum_{j}^{N_m} I(\vec{\alpha}, \vec{x}_j^m)\eta_j \;. \tag{1.9}$$

Using the fact that η is 1 for accepted events, and zero otherwise, Eq. 1.9 can be rewritten as a sum over the accepted Monte Carlo events as:

$$\int I(\vec{\alpha}, \tau)\eta(\tau)d\tau \;\; = \;\; \frac{\Omega_{tot}}{N_m}\sum_{j}^{N_a} I(\vec{\alpha}, \vec{x}_j^a) \;. \tag{1.10}$$

Assuming that the acceptance of each event datum is also 1, then the standard likelihood function in Eq. 1.6 is:

$$L \;\; = \;\; \Pi_{i=1}^{N_d} \frac{I(\vec{\alpha}, \vec{x}_i)}{\frac{\Omega_{tot}}{N_m}\sum_{j}^{N_a} I(\vec{\alpha}, \vec{x}_j^a)} \tag{1.11}$$

Then, one can take the negative of the natural logarithm of Eq. 1.11:

$$-\ln(L) \;\; = \;\; N_d \ln\left[\frac{\Omega_{tot}}{N_m}\sum_{j}^{N_a} I(\vec{\alpha}, \vec{x}_j^a)\right] - \sum_{i}^{N_d} \ln\left[I(\vec{\alpha}, \vec{x}_i)\right] \;. \tag{1.12}$$

Maximizing the likelihood of the fit then involves minimizing Eq. 1.12 with respect to $\vec{\alpha}$. The first part of the sum (inside the logarithm) is known as the normalization integral, and can often be precomputed before any fitting. It should be noted that the standard likelihood function will result in the correct shape for the distribution, but it is not necessarily constrained to preserve the normalization.

In the case where N_d events are measured, and the expected number of events $< n >$ can be determined as a function of the fit parameters, $\vec{\alpha}$, a *generalized*

likelihood function can be determined from Eq. 1.6 as follows:

$$L = \left(\frac{<n>^{N_d}}{N_d!} e^{-<n>} \right) \cdot \Pi_i^{N_d} \frac{I(\vec{\alpha}, \vec{x}_i^d)}{\int I(\vec{\alpha}, \tau)\eta(\tau)d\tau} . \tag{1.13}$$

This equation describes the probability of observing N_d events when $<n>$ are expected and that the observed events are described by the distribution function, $I(\vec{\alpha}, \vec{x})$.

The generalized likelihood is derived similarly to Eq. 1.12 [71] and is given as:

$$
\begin{aligned}
-\ln(L) &= N_d \left[\ln(N_d) - 1\right] + \frac{1}{2}\ln(2\pi N_d) \\
&+ \frac{\Omega_{tot}}{N_m} \sum_j^{N_a} I(\vec{\alpha}, \vec{x}_j^a) - \sum_i^{N_d} \ln\left[I(\vec{\alpha}, \vec{x}_i^d)\right]
\end{aligned} \tag{1.14}
$$

The full derivation can be found in Ref. [71]. The first line contains only numerical constants that depend solely on the number of data events, N_d. The first term in the second line is the normalization integral, which can be precomputed, while the last term requires the larger fraction of computational resources. Unlike the standard likelihood function, the generalized likelihood function will guarantee that the Monte Carlo will normalize to the number of data events.

1.4.2   Fitting

The actual process of fitting involves incorporating a set of waves, or the hypothesis, which are fit to the data in bins of momentum transfer and invariant mass. The production amplitudes are allowed to vary in an iterative algorithm, where each wave is characterized by the isobar parameters such as J^{PC}, ϵ, l, s, its mass and the polar and azimuthal angles in the Gottfried-Jackson frame. This is straight-forward for

simple waves (few waves with low spins) with good statistics and tools exist at Indiana University and CMU to do this and are in use for other experiments. However, there are many difficulties associated with PWA. For example, it has been seen in E852 analyses [72] that by not choosing the appropriate set of waves to describe the data set, it is possible for some amount of amplitude to be associated with an incorrect wave giving rise to possible false signals. This has led to ambiguous claims of exotic signals. Including all possible waves in the set would be nearly impossible due to the extremely large amount of computational time needed; so the problem remains to choose the best possible wave set. However, with a correct wave set, a successful fit to the data will give the proper amplitudes such that waves with exotic quantum numbers should have amplitudes greater than zero if they exist and can be seen in the data. It should also prove stable against the addition of some higher waves, if the added waves do not contribute in strength.

One of the issues that makes unbinned likelihood fits difficult to use is the fact that the log-likelihood itself is not a goodness-of-fit estimator. Various goodness-of-fit estimators have been proposed but there is no clear solution to this problem. One such method is to first note that ratios of likelihoods, or differences in log-likelihoods can be used as improvement measures for fits to the same data set. This leads to the idea of defining a likelihood measure based solely on the data set being used, and then compare the results of a fit to that of the data likelihood. Work is ongoing to determine the best method of determining a goodness-of-fit.

1.4.3 Computing Resources

Because the last term in Eqs. 1.12 and 1.14 is the CPU expensive part of the likelihood fitting procedure, there is an effort in the collaboration [73] to reduce the

resources needed to calculate this term. An amplitude analysis of 1×10^7 events, a small data set by GLUEX standards, would require nearly 10,000 CPU hours. Using parallel computing with graphical processor units (GPUs), this computing time can be reduced, due to the hundreds of cores on each GPU, and the associated software used to handle this parallel processing. The reduction of computing time is observed to be nearly a factor of 100 so far, without any serious optimization. Future hardware and software developments could reduce the computing time further. As well, the monetary cost for the GPUs is much less than the equivalent number of CPUs.

In conclusion, the intrinsic nature of Partial Wave (Amplitude) Analysis not only requires a detector with good acceptance in phase-space, good four-momentum resolution and adaquate particle identification, but also requires a good knowledge of that acceptance through Monte Carlo detector simulations. The design of the GLUEX experiment is expected to meet these needs. With these, it should be possible for GLUEX to extract exotic hybrid waves from the data.

Chapter 2

The GlueX/Hall-D Project

Based on the predictions of hybrid mesons and glueballs in lattice QCD and in various phenomenological models with guidance from previous experiments, the GlueX/Hall-D collaboration was formed to design a photon beam and detector to map the exotic hybrid spectrum [74]. Currently the experiment is in the detector construction phase having been approved for Critical Decision 3 (CD3)[1]. The experimental goals of the collaboration are to reach meson masses up to about 3 GeV/c^2 and collect sufficient statistics on the production of mesons with the ability to examine a wide variety of final state decays. Final analysis of the data to determine the J^{PC} quantum numbers to find exotic hybrids will be done through PWA. For PWA to be successful, the detector must be hermetic[2] with good rate capabilities and be able to kinematically identify exclusive reactions. A vanguard attempt to reconstruct reactions from simulated Monte Carlo data based on the full GlueX detector will be described later in this thesis.

---

[1]CD3 is a U.S. Department of Energy (DOE) milestone indicating that funds are available for construction.

[2]Sensitive and efficient over the required phase space.

2.1 CEBAF at Jefferson Lab and the 12 GeV Upgrade

The Continuous Electron Beam Accelerator Facility (CEBAF) was originally designed and constructed to accelerate an electron beam to 4 GeV by recirculating the electrons five times through two superconducting linear accelerators (linacs), each pass providing a 400 MeV energy boost. The maximum design current is 200 μA cw, corresponding to a beam loading current of 1 mA [75]. From the commissioning of the accelerator, CEBAF has consistently met or exceeded its design parameters such that with improvements to the helium processing of the cavities and power supplies, the energy of the accelerator improved to about 6 GeV before the current shutdown phase for further upgrades. Once upgrades are complete, the electron beam will have an energy of 12 GeV prior to entering the Hall-D facility and producing the photon beam for the hybrid meson search. A diagram of the accelerator layout is shown in Fig. 2.1.

Along with the creation of a new experimental hall at Jefferson Lab, Hall-D, the upgrade of the accelerator includes the boosting the energy of the beam by adding five new cryomodules to the existing 20 in each of the linacs of CEBAF. The space for the additional modules is already available, with space for further upgrades in the future. A tenth added arc will allow for 11 full passes of the electrons before delivery to Hall-D. Further upgrades to the accelerator are described in reference [76].

2.1.1 Hall-D

Hall-D is currently being built on the north-east corner of the accelerator site. Due to the lower radiation levels produced by the photon beam, the experimental hall is
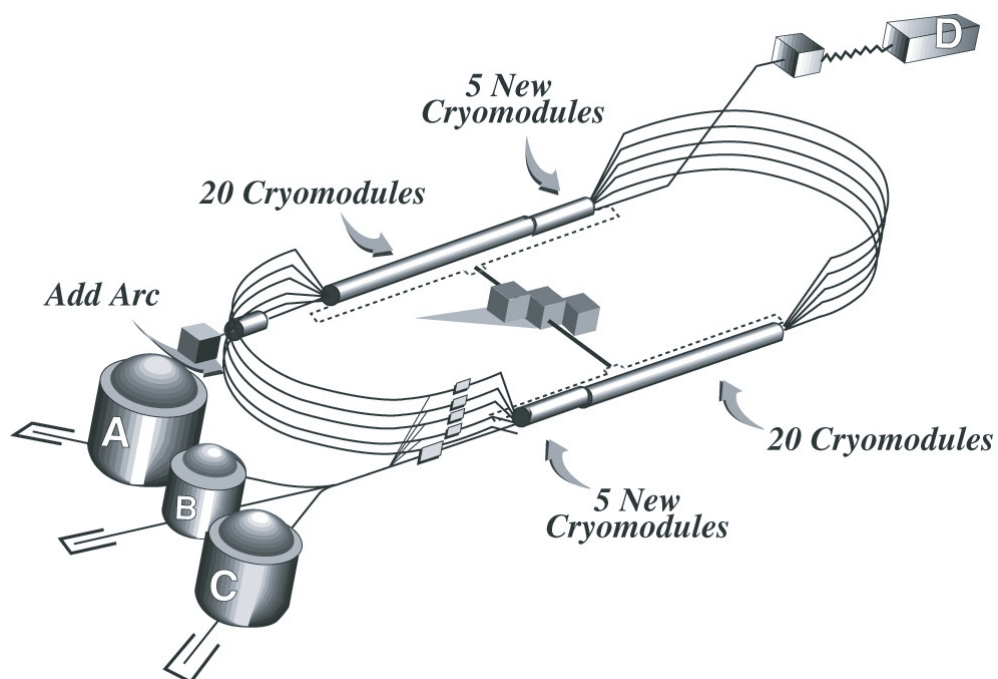
Figure 2.1: The proposed configuration for the 12 GeV upgrade of CEBAF at Jefferson Lab showing the additional new Hall D for the GlueX experiment. Details are given in the text.

built above ground, as shown in Fig. 2.1. The building in which the photon beam is tagged will exist separately from the building that will contain the detector elements. A drawing of the final building layout appears in Fig. 2.2. A horizontal schematic of the photon beam line is shown in Fig. 2.3 with the major components labelled.

Figure 2.2: A drawing of the Hall-D complex. The linac buildings are visible in the background.
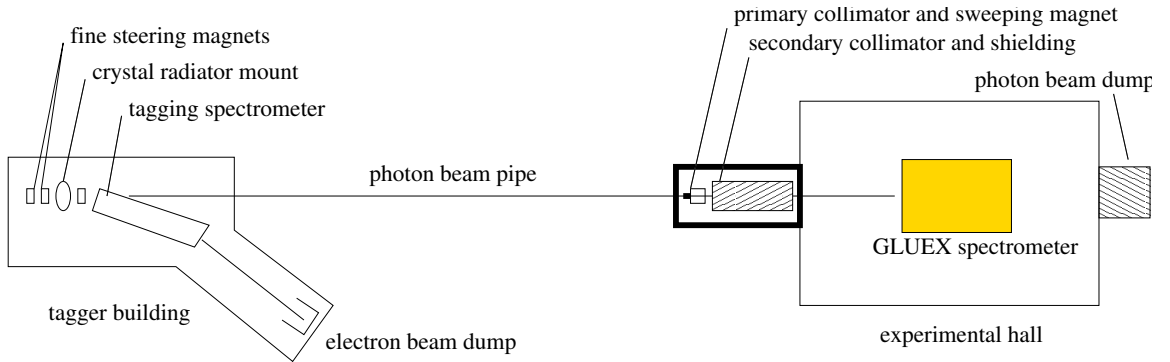
Figure 2.3: Schematic plan view of the photon beam line, shown in the horizontal plane as viewed from above. The objects in this figure are not drawn to scale. (from [77])

2.2   The Photon Beam

To produce and detect hybrid mesons in the mass region of interest, $1.5 - 3$ GeV/c^2, with sufficient resolution, the beam energy must allow the experiment to sample enough phase space to map out the spectral shape of the exotic hybrids up to 3 GeV/c^2. The beam energy must also be high enough to provide a large enough boost to the centre of mass in the lab frame. Both are accomplished with the proposed photon beam energy of 9 GeV. The photon beam must also be linearly polarized to satisfy the analysis requirements discussed later. This is related to the fact that states of linear polarization, in contrast to states of circular polarization, are eigenstates of parity. The linear polarization of the photon beam can also be used as an exotics filter, as the angular distributions of some states have terms that depend on polarization [78, 79].

2.2.1   Coherent Bremsstrahlung Photon Beam

To produce the needed linear polarization, coherent bremsstrahlung radiation is produced by scattering the 12 GeV electron beam off a thin diamond crystal radiator oriented in a particular way. For certain orientations of the crystal with respect to the electron beam, the atoms of the crystal can be made to recoil together from the radiating electron, leading to an enhanced emission at particular photon energies and yielding linearly polarized photons. The "coherent" in coherent bremsstralung does not indicate that the photons are in a coherent state, such as light from a laser. Rather, it refers to the coherent effect of the multiple atoms in a crystal lattice absorbing the momentum from a high energy electron when it radiates a bremsstrahlung photon. The uncertainty principle dictates that the position of each atom on the lattice undergoes fluctations about its mean position such that the discrete positions of

the lattice positions are somewhat smeared. The final photon spectrum then appears to be the sum of two parts: a discrete sum over the lattice positions and an integral over the continuum of momentum transfer values due to the smearing of the lattice positions. The latter is the incoherent part of the spectrum and appears as ordinary bremsstrahlung radiation proportional to the inverse momentum transfer and is invariant with respect to the crystal orientation. A typical coherent bremsstrahlung spectrum is shown in Fig. 2.4. The coherent peaks, due to the discrete crystal lattice, change in position and intensity depending on the crystal orientation.

Because of the relationship between angle and photon energy, a large portion of the incoherent spectrum can be removed by collimating the bremsstrahlung photon beam. A 3.4 mm hole, 76 m from the radiator, will not only collimate out much of the incoherent part of the beam, but will also increase the degree of linear polarization to about 40%. With the duty factor of the CEBAF electron beam being close to one, the resulting photon beam will be an excellent probe for hybrid mesons. The distribution of the energy within the collimated beam is centred around a single narrow peak which has a width at full-width half maximum (FWHM) of less than 10% of the peak energy. As well, the photons within this peak have a large degree of linear polarization. The power spectrum of the collimated beam is shown in Fig. 2.5. Note that the coherent peaks appear as enhancements on top of the incoherent bremsstrahlung continuum. The precise energy of each photon within the peak will be measured via a "tagging"spectrometer which measures the momentum of the recoil electron and thus directly determines (tags) the energy of the radiated photon.
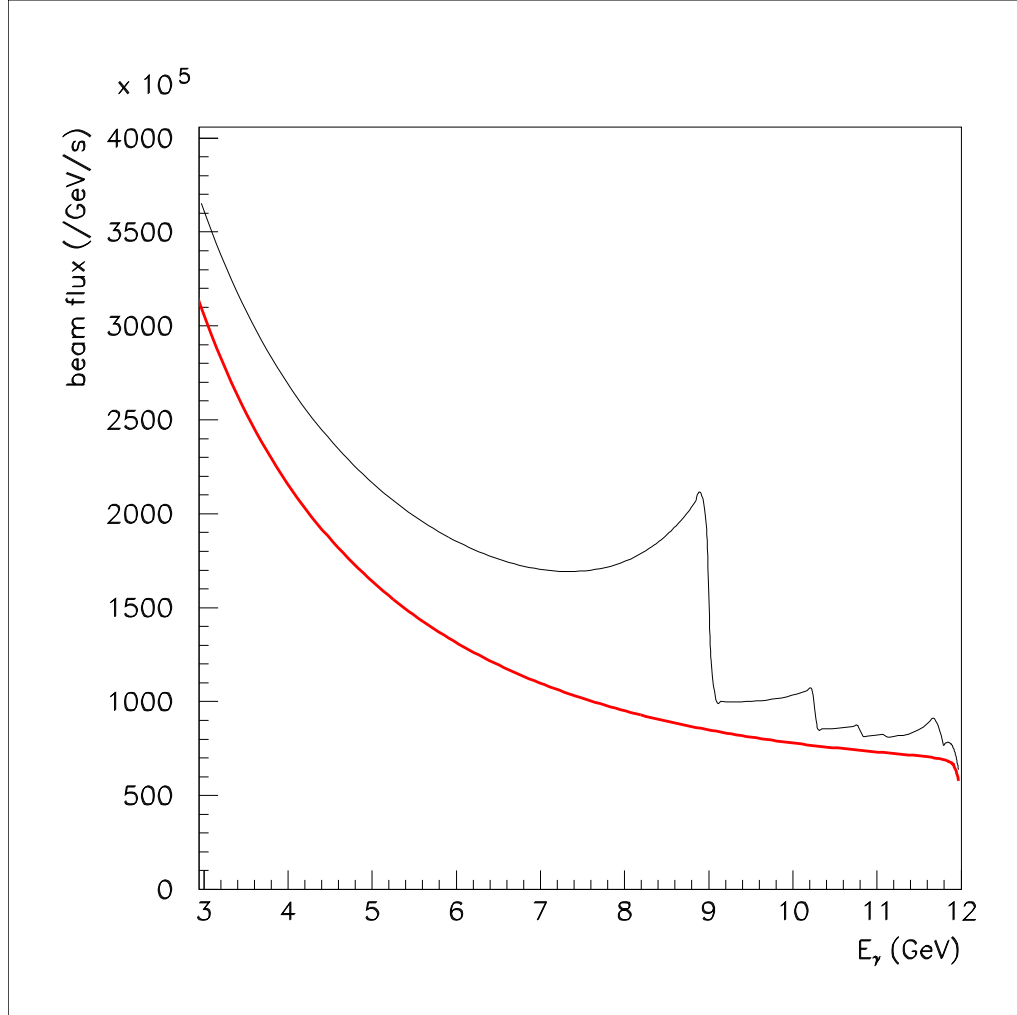
Figure 2.4: Typical coherent and incoherent bremsstrahlung spectrum from a discrete crystal lattice. The distinction between incoherent (thick line) and coherent (thin line) components in the figure is artificial; it is shown to distinguish the invariant part of the spectrum from the part that shifts as the crystal is rotated. The vertical scale in the figure gives the photon rate for a diamond crystal radiator 20 microns thick and a 1 μA electron beam of 12 GeV energy [80].
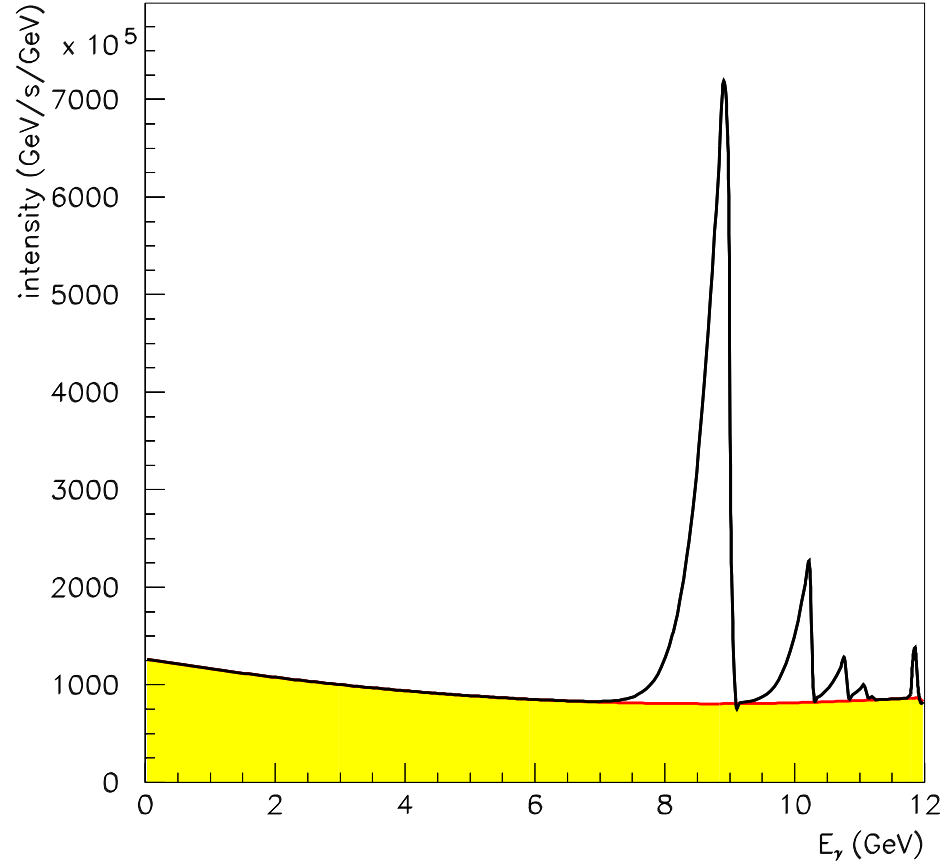
Figure 2.5: Photon power spectrum, after collimation, from an oriented diamond radiator 10^{-4} radiation lengths thick. The y axis is dP/dE with power P expressed in GeV/s and E in GeV . The electron beam current is 1 μA. Note that the coherent peaks appear as enhancements on top of the incoherent bremsstrahlung continuum [80].

2.2.2 Tagging Spectrometer

The tagging spectrometer is an Elbek-type[3] spectrometer and is shown schematically in Fig. 2.6. The 12 GeV electrons pass through the radiator target where a small fraction undergo a bremsstrahlung interaction. The electrons then pass through a focusing quadrupole before entering the dipole magnet. The majority of electrons do not interact and are bent a small angle toward the beam dump. Any recoil electrons from the bremsstrahlung interaction are bent towards a set of 190 fixed scintillation counters spanning the electron momentum range from 3.0 to 11.7 GeV, and a movable "microscope" of 500 scintillating fibres optimized for normal operation spanning the energy range from 8.3 to 9.1 GeV. The fixed array allows measurements over the entire operating range of energies, but with modest energy resolution of 0.25% and reduced rate capabilities. The microscope is needed in order to run the source in coherent mode at the highest polarization and intensities, and whenever energy resolution better than 0.25% is required. With the microscope, the source is capable of producing collimated photon intensities in excess of 2×10^8 photons/GeV/s. Further information about the radiator crystal, tagger, electron and photon beams is found in the GlueX Design report [80] and The Technical Design of the Hall-D Polarized Photon Beam [77].

---

[3]The exit face of an Elbek-type spectrometer is parallel to the entrance face of the analyzer.
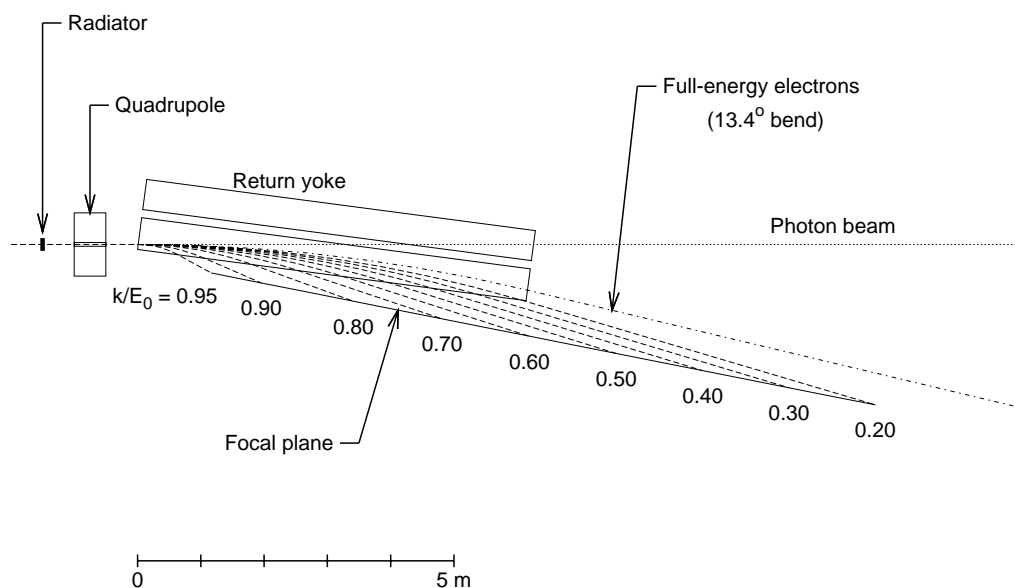
Figure 2.6: A planar view of the tagging spectrometer from above, showing the path of the primary beam and the trajectory of post-bremsstrahlung electrons of various recoil momenta. Taken from Ref. [77].

Chapter 3

The GlueX Detector

3.1 Overview

In order to achieve the primary physics goal of the GLUEX [81] experiment, that
of mapping the spectrum of gluonic excitations of light mesons, it is required that
photons and charged particles are measured with sufficient acceptance and resolu-
tion in order to be able to identify exclusive reactions, a requirement imposed by
PWA, needed to determine the J^{PC} quantum numbers of the produced mesons. The
photons of particular interest are those resulting from $\pi^0 \rightarrow \gamma\gamma$ and $\eta \rightarrow \gamma\gamma$ decays.
Photoproduction data at 9 GeV are sparse and are mainly from bubble chamber
experiments, in which the reconstruction of final states with multiple neutral par-
ticles is impossible. These all-neutral final states are expected to make up 60% of
the photoproduction cross section, underscoring both the need and discovery poten-
tial for neutral particle reconstruction. GLUEX will run in Hall-D, currently under
construction at Jefferson Lab as part of the 12 GeV upgrade to the lab.

The GLUEX detector design is ideally suited for a fixed-target photoproduction
experiment. The experimental apparatus includes: a 2.2 Tesla solenoid magnet,

with a start counter, central drift chamber (CDC), forward drift chambers (FDC) and a cylindrical lead/scintillating-fibre electromagnetic barrel calorimeter (BCAL), each inside the solenoid magnet bore, with a time-of-flight wall (TOF) and circular planar lead glass electromagnetic calorimeter downstream of the solenoid in a forward position (FCAL). A schematic of the detector is shown in Fig. 3.1. Future upgrades to the GLUEX detector may include a Cherenkov detector for enhancing particle identification (PID). The photon beam is incident on a 30 cm LH_2 target. The start counter, made of plastic scintillator that provides event timing information, surrounds the target. The FDC and CDC provide tracking information and the two electromagnetic calorimeters, the FCAL and BCAL, measure the four-momentum of decay photons with the BCAL also providing some proton/pion PID at large angles (greater than 11 degrees). The TOF, which sits immediately in front of the FCAL, provides timing information for particle identification at small angles. The dashed lines in Fig. 3.1, at angles (with respect to the beam direction) 10.8° and 126.4°, indicate the corners of the BCAL. The regions between the lines at angles 14.7° and 10.8°, and between 126.4° and 118.1°, are where the number of apparent radiation lengths is reduced due to the geometry at the ends of the module.

3.1.1 Coordinate System Definition for GlueX

The GLUEX coordinate system is typically defined in spherical coordinates when talking about a specific point (i.e. the target) along the axis of the detector, with $+z$ pointing downstream towards the FCAL along the central axis of the solenoid, with polar angle θ and azimuthal angle ϕ. When discussing the detector packages inside the solenoid, a cylindrical coordinate system is typically used, with a radius, r, defined as as the distance perpendicular to the z-axis. The origin of the global

CDC
Central Drift Chamber

118.1°

126.4°

FDC
Forward Drift Chambers

*Future
ParticleID*

TOF
Time-of-Flight

Solenoid

14.7°

10.8°

185 cm

*photon
beam*

BCAL

Barrel Calorimeter
*390 cm long
inner radius: 65 cm   outer radius: 90 cm*

FCAL

48 cm

342 cm

Forward
Calorimeter

*240 cm diameter
45 cm thick*

560 cm

30-cm target
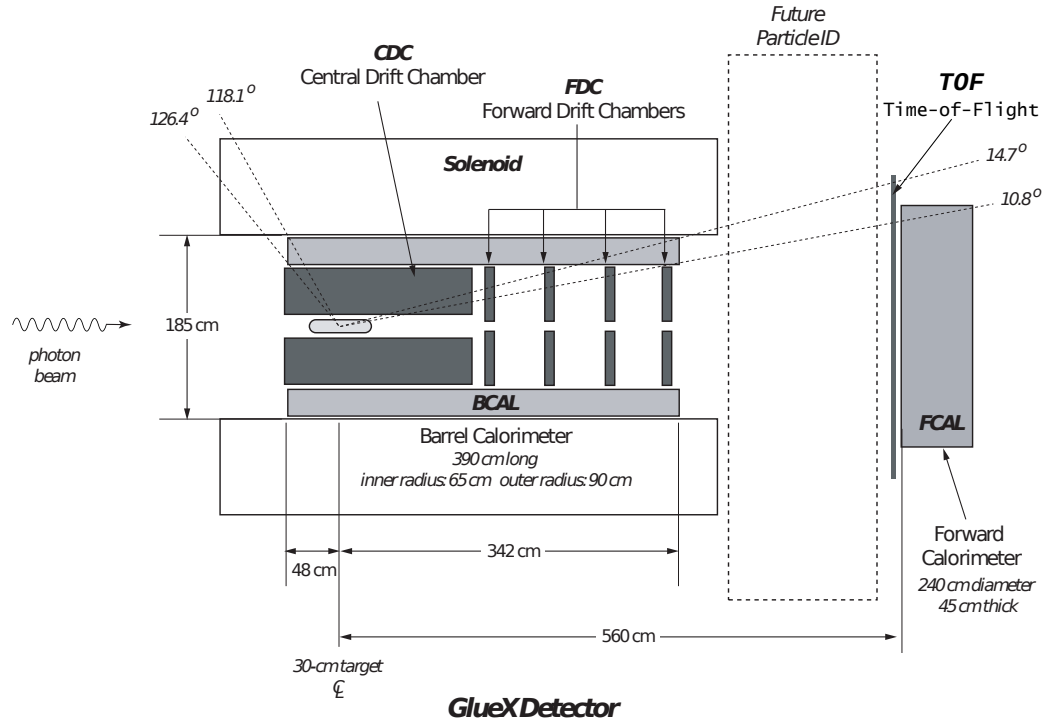
GlueX Detector

Figure 3.1: Schematic of the GLUEX Detector. The detector has cylindrical symmetry about the beam direction. The detector subsystems and dashed lines at angles (with respect to the beam direction) 10.8° through 126.4° are referenced in the text. The start counter is not shown for clarity. Taken from Ref. [80]

z-axis is defined as the upstream edge of the solenoid magnet, 65 cm upstream of the target centre and 17 cm before the upstream edge of the BCAL.

3.2 Solenoid Magnet

The 2.2 T magnetic field provided by the solenoid will perform two functions in the GLUEX experiment. The first is to provide momentum analysis for the charged particles produced. The field will curve the paths of the charged particles as they pass through the bore of the solenoid. The CDC and FDC tracking detectors will record hits where the charged particles passed though, and reconstruction software can then determine the momentum of the reconstructed tracks. The second function of the strong magnetic field is to sweep away any low-energy electromagnetic background (generally e^+e^- pairs) created due to the high intensity photon beam.

The solenoid that will be used for GLUEX was built at SLAC ca. 1970 for the LASS spectrometer and was subsequently moved to LAMPF in 1985 for inclusion in the MEGA spectrometer. The MEGA experiment and the solenoid were decommissioned in place in 1995. In 2002 the coils were examined and determined to be in good condition and could be reused. The solenoid was shipped from LANL to the Indiana University Cyclotron Facility (IUCF) in the fall of 2002 for testing and refurbishing of the four coils (this is now nearing completion). The inner bore diameter is 185 cm with an overall finished length of 495 cm. Within the clear bore region, the field homogeneity is $\pm 3\%$. Along the beam axis the field homogeneity improves to $\pm 1\%$. Table 3.1 summarizes the important parameters of the magnet.

A study of the solenoidal field and variations in the field are presented in Ref. [82].

Inside winding diameter of SC coils	203 cm
Clear bore diameter	185 cm
Overall length (iron)	495 cm
Coil-to-coil separation	28 cm
Total iron weight	210 tonnes
Central field	22 kGauss
Axial load per coil due to magnetic forces	255 tonnes
Conductor current	1500 A(nominal) 1800 A(max)
Total stored energy	36 MJoules
Inductance	22 H
Total helium volume (including reservoir)	5000 litres
Operating heat load (liquid He)	30 litres/hour
Operating heat load (liquid nitrogen)	30 litres/hour
Turn on time	20 minutes
Turn off time (normal)	20 minutes
Cool-down time	2 $weeks$

Table 3.1: Summary of characteristics of the GLUEX solenoid as used in the LASS configuration. Taken from Ref. [80] with units converted to metric.

3.3 Target

For the main physics program of GLUEX, a liquid hydrogen target will be used. The design is fairly simple as the photon beam will deposit only 100 mW in the target such that natural convection is enough to remove heat from the target cell. Because the solenoid magnet is supplied with 4.5 K helium, using this as a refrigerant for the target cell simplifies the cooling process and removes the need for a separate refrigerator for the target.

The target is a cylindrical mylar cell design with a liquid hydrogen volume 30 cm long and 3 cm in diameter. The mylar cell will be mounted on a metal base to provide for liquid entry ports and a reliable means of positioning the cell. The beam will enter through a thin window, where the diameter of the entrance window is large enough to allow the beam to enter the cell without scraping the edges of the window causing secondary particles. The area between the window and the outer wall of the cell is sufficiently large to allow for convection and to prevent bubbles from being trapped. A system such as this, containing a few hundred cm^3 of liquid hydrogen, would be considered "small" by Jefferson Laboratory standards.

3.4 Start Counter

The Start Counter will provide a fast timing signal used in the level-1 trigger of the experiment. As an element of the level-1 trigger, the Start Counter must have a moderate timing resolution (better than 5 ns) with a large solid angle coverage and a high degree of segmentation. Using tracking information, the Start Counter will be able to provide a modest time resolution of better than 0.5 ns, thus allowing for identification of the electron beam pulse associated with the event. The Start Counter

will consist of 40 plastic scintillator paddles, 5 mm thick, arranged cylindrically. The downstream side of the scintillators will be bent toward the beam line in order to increase the solid angle coverage while minimizing multiple scattering. This type of design will have a large light yield and should produce a good timing signal. Readout will be done with either magnetic-field resistant photomultiplier tubes (PMTs) or solid-state devices such as silicon photomultipliers (SiPM).

3.5 Charged Particle Tracking

3.5.1 Central Drift Chamber

The Central Drift Chamber (CDC) will consist of a 1.5 m straw-tube chamber that is located at the upstream end of the GLUEX solenoid and surrounds the liquid hydrogen target and Start Counter [83]. There are 24 layers of straw-tubes, starting at an inner radius of 10 cm up to an outer radius of about 54 cm, with 3098 readout channels in total. Each straw-tube is 1.6 cm in diameter constructed of aluminized Kapton[1] with a gold-plated tungsten sense wire strung down the middle. The tubes are filled with a gas mixture of $Ar/CO_2/CH_4$ with proportions 80/10/10 (appx.) for ionization by charged particles. This straw-tube design minimizes the amount of material in the detector and provides for a uniform electric field, thereby improving reconstruction capabilities. The downstream end-plate is constructed of carbon fibre, the upstream plate is aluminum, and the outer shell is fibre-glass – all of which minimize the available material in the detector. The chamber will detect charged particles coming from the GLUEX target with polar angles between about 6° and 165°, although the detection efficiency and resolution decrease at the extreme angles

---

[1]Kapton® is a registered trademark of E. I. du Pont de Nemours and Company or its affiliates.

due to fewer straw-tubes being crossed. Any particles going forward at angles less than 25° will also be seen in the FDC.

To achieve the physics goals of GLUEX, the CDC will require a position resolution perpendicular to the wires of $\sigma_{r\phi} \sim 150\mu$m, and a position resolution along the length of the wire $\sigma_z \sim 1.5$ mm [81], and be able to make dE/dx measurements that will allow for the separation of protons and pions below 450 MeV/c [84]. The desired $\sigma_{r\phi}$ resolution can be obtained arranging the straw tubes appropriately. The σ_z resolution will be achieved by placing about 1/3 of the straw tubes at stereo angles of ±6° relative to the straight wires. The dE/dx will be achieved by reading out the tubes using Flash ADCs (FADCs) and then accounting for the path length in the straw tube determined from the timing information of the signals.

In the GLUEX detector, particles which have small enough transverse momentum will be bent into circles and effectively stay within the tracking volume. In particular, many of these particles are slow protons, with momentum under 450 MeV/c, where the only particle identification system is the CDC. The purpose of the dE/dx measurement in the CDC is to separate these protons from similar momentum pions. Pions and protons with momentum greater than 450 MeV/c will also be detected in the BCAL, which can then also be used to aid particle identification.

3.5.2   Forward Drift Chambers

The Forward Drift Chamber system (FDC) is designed to track forward-going charged particles from the target ($1° < \theta < 20°$) in the 2.24 T magnetic field of the solenoid [85]. The choice of cathode chambers with wire readout has been made in order to provide a three-dimensional space point from each active chamber layer. Due to the spiraling trajectories of the charged particles and the high multiplicity of charged

tracks passing through the FDC, it is crucial for this system to be able to provide a sufficient number of measurements with appropriate redundancy to enable linking of the hits from the different tracks with high accuracy, while providing good spatial resolution with reasonable direction information.

The FDC system consists of four separate chamber packages. Each package consists of six cathode-wire-cathode plane groupings. Each chamber is 1.2 m in diameter and consists of a wire plane flanked on either side by cathode planes divided into thin strips. The strips are oriented at $\pm 75°$ with respect to the wires and $150°$ with respect to each other. Neighboring chamber layers will be rotated by $60°$ with respect to each other in order to improve track reconstruction decisions on the corresponding left/right ambiguities in the wire planes, hence improving the overall resolution. By charge interpolation of the electron avalanche image charge in the cathode strip readout, spatial resolutions at the cathode planes should achieve the design goal for resolution of 200 μm. The purpose of crossing the strips is to provide redundant coordinate information, as well as to aid in pattern recognition in the background environment expected in the spectrometer. The drift times from the wires will also be read out, giving a precision coordinate in the dimension perpendicular to the wires that should meet the design goal of 200 μm. The planned gas mixture for the FDC chambers consists of 40% Ar and 60% CO_2.

3.6 Calorimeters

The calorimeters of the GLUEX detector system play multiple roles and are emphasized in this thesis. Their principal role is to detect the photons from η and π^0 decays which, in turn, may be from other meson or excited baryon decays (N^* or Δ). The positions and energies of the photons must be determined with suffi-

cient accuracy and resolution to allow for a complete kinematic reconstruction of the event. The Forward Calorimeter (FCAL) and Barrel Calorimter (BCAL) will have complimentary functions in GLUEX for measuring the decay photons.

3.6.1 Forward Calorimeter

The Forward Calorimeter (FCAL) is a 2.4 m diameter circular stack of 2800 lead-glass blocks (see Fig. 3.2) whose front face is located 560 cm downstream of the GLUEX target center [86]. The design of the FCAL largely makes use of the experience gained in constructing and operating very similar lead-glass calorimeters for the E852 experiment at Brookhaven [87] and the RadPhi experiment in Hall-B at JLab. The lead glass blocks are recycled from the E852 experiment and have been refurbished and will be restacked.

The FCAL will measure the energy of decay photons by measuring the amount of Čerenkov light produced in the lead glass blocks from the decay photon passing through the dense material and creating an electromagnetic shower. The high atomic number, Z, of the lead in the lead glass results in a short radiation length. The charged particles produced in the electromagnetic shower are of sufficient momentum such that their velocities exceed the speed of light in the absorber and thus produce Čerenkov light as they pass through the lead glass [88]. The intensity of the Čerenkov light produced is proportional to the energy deposited in the lead glass, and therefore the total amount of light produced in the lead glass calorimeter is a direct measurement of the total energy of the incident decay photon.

The glass, manufactured in Russia, is designated as type F8-00 glass with a chemical composition of 45% PbO, 42.8% SiO_2, 10.4% K_2O and 1.8% Na_2O. The glass has a density of 3.6 g/cm^3, a radiation length of 3.1 cm and an index of refraction

of 1.62. The lead glass blocks have transverse dimensions of 4×4 cm^2 and are 45 cm long. Each block is optically isolated from the others by an aluminized mylar wrapping. The center 3×3 blocks are removed to produce a 12×12 cm^2 beam hole. The blocks surrounding this hole will be made of radiation hard lead-glass due to the high radiation intensity near the photon beam. Radiation damage to the lead glass reduces the transmission efficiency of the glass over the shorter (blue) wavelengths. The current plan is to instrument the inner 11×11 array with radiation-hard F108 glass. Type F108 lead glass is a factor of 100 more radiation-hard than type F8-00.

Each block will be read out using an FEU 84-3 photomultiplier tube (PMT), also manufactured in Russia. These twelve-stage PMTs have a maximum gain of 2×10^5 and connected to a custom-designed Cockcroft-Walton base [89] with relatively low power dissipation – about 0.2 W per base. This is important for heat disapation due to the close packing of many phototubes [90].

Phototubes at the FCAL position will see a magnetic field from the solenoid on the order of 200 *Gauss*. For this reason, the phototube will be recessed from the lead-glass by using a cylindrical light guide and shielded with soft iron and μ-metal reducing the magnetic field to $10 - 20$ *Gauss*.

The number of photoelectrons seen in the phototube is a large contributor to the energy resolution of the FCAL and any improvements to the detector to increase the number Čerenkov photons seen and, therefore, the number of photoelectrons produced, improves the resolution. Based on Monte Carlo simulations, improved optics and the resolutions of the E852 and RadPhi lead-glass calorimeters, the FCAL is expected to have an energy resolution of $5.6\%/\sqrt{E(GeV)}$.

LGD (LEAD GLASS DETECTOR)

4 X 4 X 45CM LEAD
GLASS BLOCK

EIGHT POINT HANGING CONNECTION

PMT CELL WALL

SOFT IRON CELL WALL TUBE

FCAL PMT

REAR PLATFORM

15 FEET

View of GlueX FCAL
Assembly from Downstream
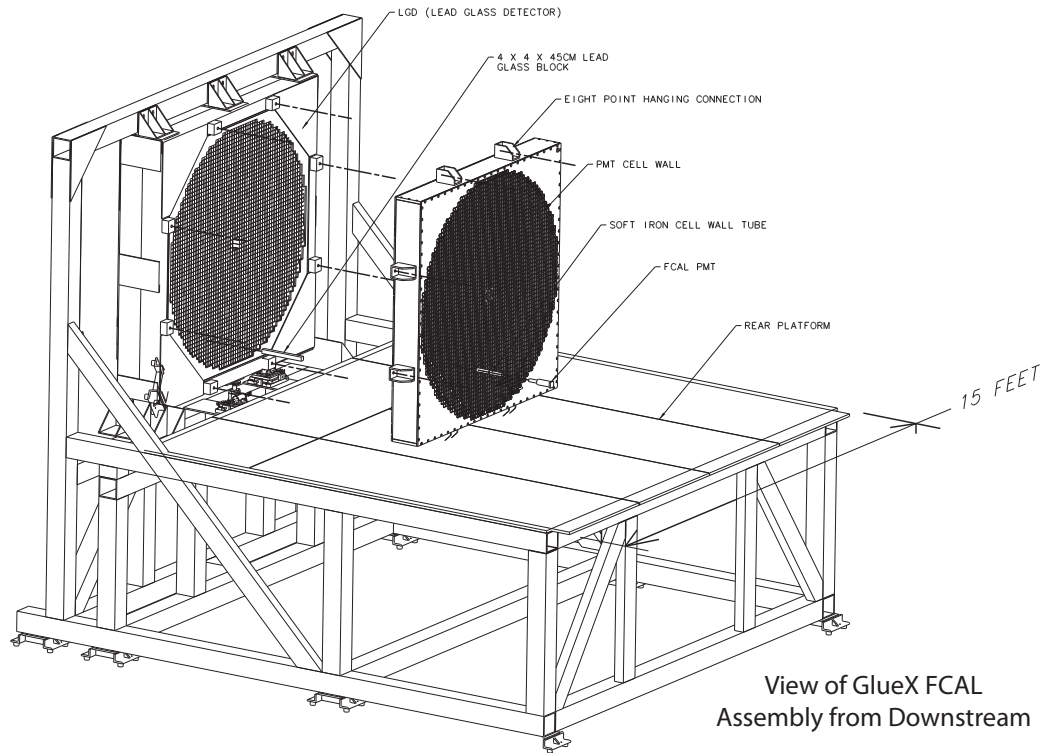
Figure 3.2: The Forward Calorimeter (FCAL) consisting of 2800 lead glass blocks arranged in a circular stack. The front of the array is located 560 cm downstream of the target center. The diameter of the circular stack is 240 cm. Figure taken from Ref. [86]

3.6.2 Barrel Calorimeter

The Barrel Calorimeter (BCAL) is shown schematically in Fig. 3.3 and, relative to the other detectors, in Fig. 3.1 . The BCAL is 390 cm long with an internal radius of 65 cm and an external radius of 90 cm, evenly divided into 48 individual modules. The dimensions of this calorimeter are driven by the volume required for charged particle tracking and the bore dimensions of the solenoidal magnet. The BCAL design is based on that of the electromagnetic calorimeter used in the KLOE experiment at DAΦNE-Frascati, which also operated in a solenoidal magnetic field [91–93]. The BCAL and KLOE calorimeters both employ a lead/scintillating-fibre (Pb/SciFi) matrix of similar length with photosensors at either end to provide energy (ADC) and time (TDC) measurements. The diameter of the KLOE calorimeter is about three times that of the BCAL.

As in the FCAL, the relevant parameters for the BCAL that determine the π^0 and η mass resolutions are the photon energy (E) and the polar and azimuthal position resolutions (σ_θ and σ_ϕ). The energy resolution (σ_E) depends on the number of photoelectrons (N_{pe}) yielded by the photosensors, based on the collected light. The photoelectron statistics are strongly dependent on the stochastic fluctuations of the energy deposited by the electromagnetic shower in the scintillating fibres of the calorimeter modules. In addition, the number of photoelectrons collected depends on the fraction of photon shower energy deposited in the fibres, the efficiency with which the resulting scintillation light is captured in and transmitted down the fibre to the photosensor, and the photon detection efficiency of the photosensor.

The photon position resolution is determined by the readout segmentation in the azimuthal direction and the difference in arrival time (ΔT) of the scintillation light between the two ends of the barrel. The resolution in the time difference ($\sigma_{\Delta T}$), and
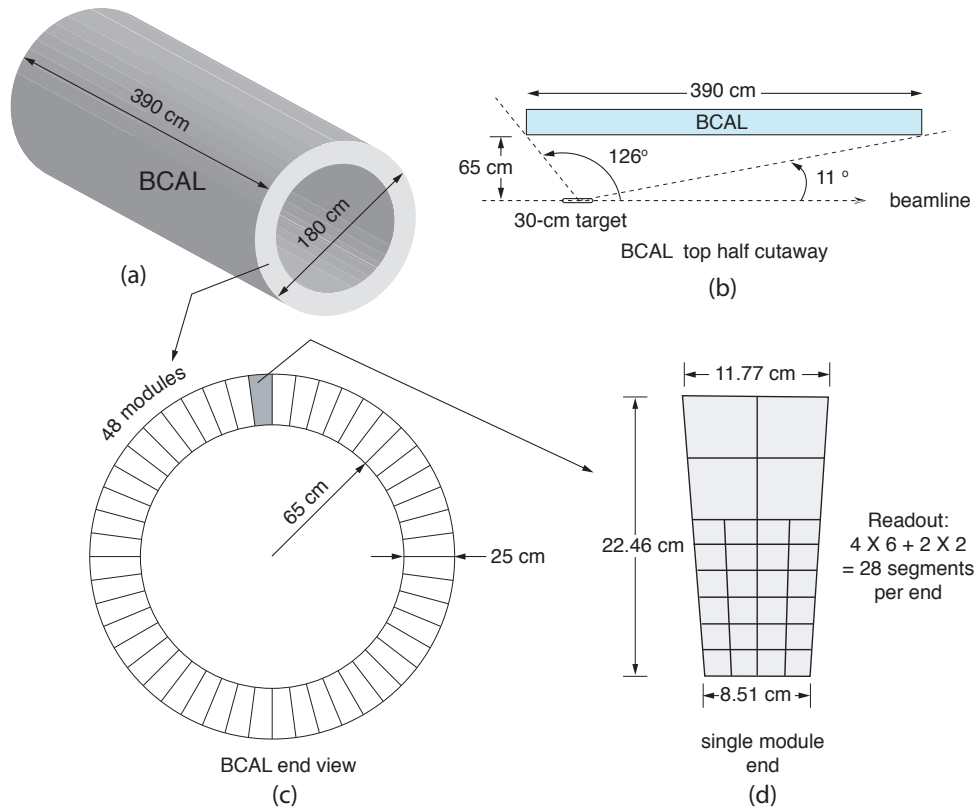
Figure 3.3: The GLUEX BCAL. (a) BCAL schematic; (b) a BCAL module side view; (c) end view of the BCAL showing all 48 modules and (d) an end view of a module showing readout segmentation. Details are given in the text.

therefore the polar angle resolution, also depend on the number of photoelectrons. The time resolution is a critical input into the momentum resolution for photons and for the particle identification for charged particles, in conjunction with trajectories from the drift chambers. As such, the time difference analysis reported below is more representative of the intrinsic BCAL resolution and independent of any external timing reference. Other parameters of relevance for extracting the four-momenta with good resolution and accuracy are adequate segmentation to avoid multiple occupancy, good linearity and a sufficiently low-energy threshold for photon detection.

The performance metrics for these quantities were set by simulating hadronic photoproduction at GLUEX energies using PYTHIA[2] [94] and also by simulating several of the signature reactions expected to yield exotic mesons. These studies included a GEANT3-based simulation [95] of the entire GLUEX detector response, including detector material and cabling, photon reconstruction and kinematic fitting. The PYTHIA simulations indicate that 70% of the produced photons with energies up to about 2 GeV will be incident on the BCAL. The photon population in the BCAL for one of the signature reactions, $\gamma p \to \eta \pi^0 p \to 4 \gamma p$, where the distribution in $\eta \pi^0$ mass was uniform from 1.0 to 2.0 GeV/c^2 and uniform in decay angles, is shown in Fig. 3.4. The distribution of photons is plotted as a function of position from the upstream end of the BCAL; the photons predominantly populate the downstream end of the BCAL. The target occupies the region $z = 33 - 63$ cm. Also shown is the average energy as a function of z with higher energy photons being more forward. The integrated thickness of the BCAL matrix, in number of radiation lengths, traversed

---

[2]PYTHIA was designed and tuned by the authors for much higher energies. Special efforts were taken by the HERMES collaboration to adapt it to the HERA electron energy of ∼30 GeV. GLUEX slightly adapted the version from HERMES to energies as low as 3 GeV, and compared the PYTHIA results with some experimental data. At 9 GeV PYTHIA underestimates the total photoproduction cross section, providing ∼80 μb instead of ∼120 μb. However, the partial cross sections from PYTHIA, scaled up by a factor 120/80=1.5 are in a reasonable agreement with the experimental data [56].

by photons incident at various positions along the length of the BCAL is also shown. Note that there is a narrow ($\sim 1°$) angular range near $11°$ where the photon trajectory intercepts a small number of radiation lengths of the Pb/SciFi matrix. Photons with polar angles less than $10°$, with respect to the beam direction, are detected in the FCAL.

Moreover, the segmentation shown in Fig. 3.3d leads to double-occupancy in less than one-percent of events with two or more photons incident on the BCAL. This segmentation is also required for adequate determination of the azimuthal angle of tracks as well as for providing information on the energy deposition profile in depth, for good cluster identification. Finally, studies of the lowest energy photons in high-multiplicity reactions that are expected to yield exotic hybrids, such as $\gamma p \rightarrow b_1(1235)\pi n \rightarrow 2\pi^+\pi^-2\pi^0 n$, indicate that an energy threshold of 40 MeV suffices [?].

It is important to point out differences in the GLUEX and KLOE applications of barrel calorimetry. KLOE is a symmetric colliding beam experiment with the intersection region at the centre of its barrel calorimeter. As a result, that calorimeter is illuminated symmetrically and nearly uniformly by photons having energies, on average, between 100 and 200 MeV and with very few photons greater than 400 MeV. On the other hand, GLUEX, is a fixed target experiment, resulting in a highly asymmetric photon distribution: 30% of the photons in the BCAL will have energies considerably higher than 500 MeV. Despite these differences, the KLOE experience provides valuable guidance in the design and construction of the BCAL . The achieved KLOE resolutions [93] of $\sigma_E/E = 5.4\%/\sqrt{E(\text{GeV})}$ and $\sigma_{\Delta T/2} = 56/\sqrt{E(\text{GeV})}$ ps are also adequate to achieve the GLUEX physics requirements, as indicated by simulation studies [?]. The extracted resolutions are a direct result of the internal Pb/SciFi matrix geometry such that similar or better resolutions should be expected for the
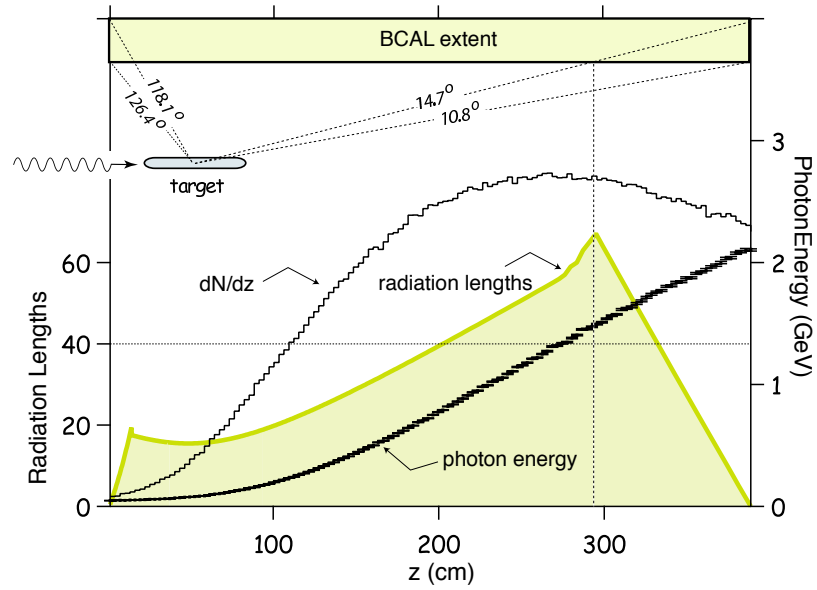
Figure 3.4: The distribution of photons, their energy and integrated path length through the Pb/SciFi matrix as a function of position along the length of the BCAL for one of the GLUEX signature reactions, $\gamma p \rightarrow \eta \pi^0 p \rightarrow 4\gamma p$, is shown. The target position and angular range subtended by the BCAL are also presented.

BCAL [96], which will be explained more thoroughly in later chapters. One of the improvements will be from double-clad fibres being used in the Pb/SciFi matrix of the BCAL, which will increase the total number of photoelectrons seen and, as a result, will provide a better timing and energy resolution.

A photograph of a production module to be used in the full barrel calorimeter is shown in Fig. 3.5. A straight-edge ruler is placed on the far end of the module and is illuminated with a lamp. The uniformity of the matrix can be seen with only a couple rows shifted. This is a result of errors in producing the module.
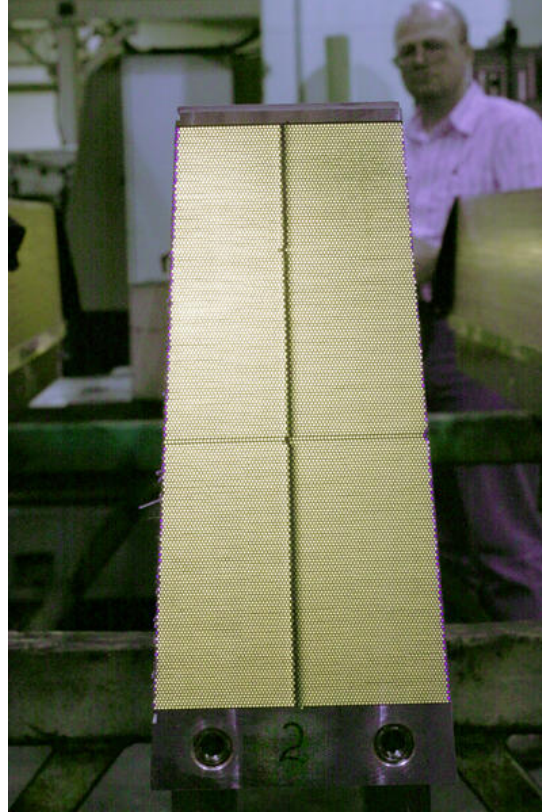
Figure 3.5: A photograph of a final production module for the BCAL. A ruler is placed on the far end and illuminated to illustrate the uniformity of the matrix. The thin, inner and thicker, outer aluminum plates can be seen mounted to the finished module.*(original in colour)*

3.6.2.1 Module Details

Table 3.2 on page 57 summarizes the salient features of the BCAL. These parameters are based on the KLOE experience, detailed GEANT-based simulations and tests of a full-scale prototype with charged particles, photon beam, lab-testing and cosmic rays. Aside from the attenuation length, the SciFi parameters are not brand specific but rather represent the generic parameters of double-clad fibres. The latter have a higher capture ratio compared to single clad fibres, such as used in KLOE. The nominal increase in capture ratio is over 50%, thus resulting in a similar increase in the number of photoelectrons, which can be important for low energy photons incident on the BCAL and the corresponding thresholds of the detector.
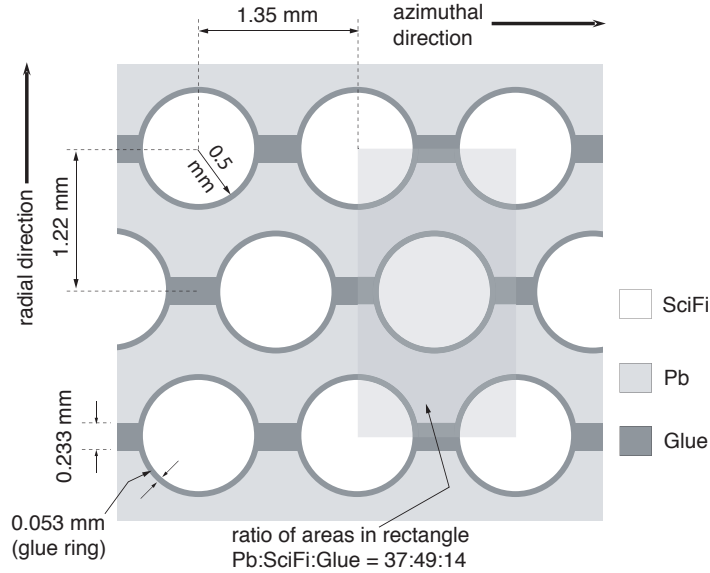
Figure 3.6: The BCAL fibre matrix showing the placement of 1 mm diameter fibres in the azimuthal and radial directions. The dimensions of the azimuthal and radial pitch, the glue box between the lead sheets and the glue ring around the fibres were determined from the prototype module using a measuring microscope. Particle tracks would appear to enter the matrix from the bottom. More details are given in Ref. [97].

The setup and running of the JLab beam test and the subsequent analysis con-

stitutes an important part of this thesis. The analysis of the beam test data showed an energy resolution for the BCAL of $\sigma_E/E = 5.4\%/\sqrt{E(\text{GeV})} \oplus 2.3\%$ and a time difference resolution of $\sigma_{\Delta T/2} = 70 \text{ ps}/\sqrt{E(\text{GeV})}$ ps. The number of photoelectrons per GeV of deposited energy was found to be about 660. The beam test is described in Chapter 5.

Table 3.2: BCAL properties. Superscript: a - design parameters of the BCAL specified for the final detector; b - quantities that have been measured; c - specifications from the manufacturer; d - from literature; e - parameter calculated from known quantities; f = parameter estimated from simulations. The number of radiation lengths as well as the resolutions in the table are all at $\theta = 90°$ incidence.

Property	Value	Ref.
Module Geometry		
Number of modules^a	48	
Module length^a	390 cm	
Module inner cord^a	8.51 cm	
Module outer cord^a	11.77 cm	
Module thickness^a	22.5 cm	
Module azimuthal bite^a	7.5°	
Lead sheet thickness^c	0.5 mm	
Fibre Properties		
Fibre diameter^c	1.0 mm	[98]
First cladding thickness^c	0.03 mm	[98]
Second cladding thickness^c	0.01 mm	[98]
Core fibre refractive index^c	1.60	[98]
First cladding refractive index^c	1.49	[98]
Second cladding refractive index^c	1.42	[98]
Trapping efficiency^{c,d,e}	5.3% (min) 10.6% (max)	[98–100]
Attenuation length^b	(351±17) cm	GlueX-doc-1317
Effective speed of light^b, c_{eff}	(16.2±0.4) cm/ns	[101]

Table 3.2, continued.

Matrix Parameters		
Radial fibre pitch[b]	1.22 mm	
Azimuthal fibre pitch[b]	1.35 mm	
Volume ratios[b]	37:49:14 (Pb:SF:Glue)	[97]
Effective mass number[e]	179.9	[97]
Effective atomic number[e]	71.4	[97]
Effective density[e]	4.88 g/cm^3	[97]
Sampling fraction[f]	0.125	[102]
Radiation length[e]	7.06 g/cm^2 or 1.45 cm	[97]
Number of radiation lengths[e]	$15.5X_0$ (total thickness)	[97]
EM Shower Properties		
Critical energy[e]	11.02 MeV (8.36 MeV)	[103, 104]
Location of shower maximum[e]	$5.0X_0$ ($5.3X_0$) at 1 GeV	[103, 104]
Thickness for 95% containment[e]	$20.3X_0$ ($20.6X_0$) at 1 GeV	[103, 104]
Molière radius[e]	17.7 g/cm^2 or 3.63 cm	[104]
BCAL Resolutions		
Energy resolution[b], σ_E/E	$5.4\%/\sqrt{E} \oplus 2.3\%$	[?]
Time difference res.[b], $\sigma_{\Delta T/2}$	70 ps/$\sqrt{E}$	[?]
z-position resolution[b], σ_z	1.1 cm/$\sqrt{E}$ (weighted)	
Azimuthal angle resolution[f]	~ 8.5 mrad	
Polar angle resolution[f]	~ 8 mrad	

3.7 Time-of-Flight

The current design of the GlueX Time of Flight (TOF) detector consists of two $252 \times 252\ cm^2$ planes of plastic scintillator bars placed approximately 5 m downstream of the GlueX target [80]. Each plane contains 42 bars of dimensions $252 \times 6 \times 1.25\ cm^3$ with a $12 \times 12\ cm^2$ central hole for the photon beam to pass. Each bar (except possibly the central bars) will be read out on both ends by photomultiplier tubes. The thickness of the scintillation bars, the dimension along the beam direction, is set by the requirement that sufficient light be produced to meet the time resolution requirements, while at the same time minimizing the amount of material in front of the FCAL. One plane has vertical bars, the other has horizontal bars. To separate pions and kaons of momenta up to 2.5 GeV/c, a combined time resolution (using four time measurements, one measurement per bar end) of less than 80 ps across the surface of the detector is desired. The TOF detector will cover the polar angles between 1° and about 11°. This provides a good overlap with the start counter in the forward region.

The TOF will provide (1) fast signals to the trigger logic regarding forward track multiplicity, (2) timing information with sufficient resolution to add complementary information to the photon tagger and the start counter to identify the event- beam-bucket in offline data analysis, and (3) TOF information for PID. While the first two requirements are moderate in terms of timing resolution requirements, PID by using TOF information, however, requires very fast detectors with very good timing resolution over moderate flight distances.

3.7.1 Particle Identification

The knowledge of a particle's momentum and velocity allows for the determination of the mass and hence the identity of the particle. To determine the velocity of a particle, two pieces of information are necessary: (1) the time it took for the particle to reach the TOF wall provided by the TOF and Start Counter and (2) the path length from the production vertex to the detection point on the wall. Since the particles are charged and in a solenoidal magnetic field, the path length is helical and will be measured by the charged particle tracking system. The tracking system will also provide the momentum of the particle.

PYTHIA simulations have shown [105] that the TOF system will be able to identify kaons with high efficiency and low contamination up to momenta of 1.9 GeV/c. Proton identification with very good efficiency and low contamination will be possible up to 3 GeV/c. While no other PID systems, such as a Čerenkov based RICH, are currently proposed for the GLUEX detector system, there is space in front of the TOF and FCAL wall to place one. This would provide good PID for momenta over 2 GeV/c.

3.8 Electronics

The balance between cost and effectiveness of the GLUEX detector is governed largely by the number of electronics channels to be read-out and the cost to instrument them. A more finely segmented calorimeter system could provide better position and angular resolution, but at the cost of a hundreds of dollars per channel it is more prudent to chose a segmentation that will achieve the physics goals of the experiment while maintaining a reasonable budget. As with any experiment, this has driven the

design for the readout and associated electronics for systems such as the BCAL and FCAL. A summary of the electronics can be found in [106].

3.9   Trigger

The trigger in GLUEX allows for simple rejection of background events in the detector that are of no interest, and will also control the data rate at which events are recorded by the data acquisition system. The algorithm for rejecting or accepting an event is determined by the criteria for differentiating the events of interest from uninteresting background events. In the case of hybrid meson decays, the final states do not look overly different from normal (background) photoproduction decays. As such, the first rejection algorithm, the Level-1 trigger, must accept anything in the useful energy range of the photon beam, 8.4–9 GeV. Events with energies outside of this range are considered background at this trigger level. A thorough review of the trigger is found in the GLUEX Trigger Review document [107].

Purely electromagnetic interactions of the beam in the target, such as pair production, although strongly suppressed in the GLUEX detector by the solenoidal magnetic field and the detector arrangement, can give signals in the individual detectors. They can either fire the trigger, or pile up in low energy hadronic events, thus producing events that appear to have larger energies. This increases the background rate of events to be rejected.

The GLUEX detector will start taking data at a luminosity corresponding to about 10^7 photons per second in the photon-beam energy range of $8.4 \leq E \leq 9.0$ GeV. In later phases of the experiment, the beam flux will be increased by an order of magnitude to 10^8 photons per second. When running at a low beam rate, the Level-1 trigger has to reduce the rate from electromagnetic and hadronic interactions seen

by the GLUEX detector to a level acceptable by the data acquisition system for writing events directly to disc (about 20 kHz.) For runs with a photon beam rate of 10^8/s, events accepted by the Level-1 trigger will be sent to the third level trigger at a rate which should not exceed 200 kHz. The Level-3 trigger will perform an event reconstruction on a computer farm which allows for a further reduction of the low-energy photon interactions and provides an additional rate reduction by about a factor of 10. After the Level-3 trigger, events will be recorded to disc for further analysis later. GLUEX is expected to produce data on the order of Petabytes per year.

From a study of PYTHIA Monte Carlo simulations of the GLUEX detector, the Level-1 trigger algorithm performs a simple background rejection based on hit multiplicity in the Start Counter and energy thresholds in the FCAL and BCAL. The algorithm provides sufficient background rejection and still has a trigger efficiency for decays of interest near 100%.

Chapter 4

BCAL Module Composition

The BCAL derives its energy resolution not only from its sampling fraction, determined by the geometry of the scintillating fibres in the matrix, but also from the properties of the fibres and the amount of light produced or, more accurately, the number of photoelectrons seen in the photo-detectors. The timing resolution is almost entirely dependent on photoelectron statistics since the path length in the fibre does not vary significantly. As such, it was very important to understand the light production and transmission characteristics of the fibres and the light-guides that connect the fibres to the sensors.

4.1   Scintillating Fibres

In this section of the thesis, the investigation focused on the measurement of wavelength spectra from 1-mm-diameter PHT-0044 and BCF-20 scintillating fibres (SciFi) and the subsequent analysis to extract the short- and long-attenuation lengths, as well as the dependence of the attenuation length on wavelength[1].   Both SciFi types

---

[1]Since this study, Kuraray SCSF-78MJ, double-clad, blue-green fibres were selected for the production BCAL, owing to their superior performance.

are composed of a core of polystyrene and two layers of polymethylmethacrylate cladding: the first from acrylic and the second from fluor-acrylic material, having thicknesses of 3% and 1% of the fibre's diameter [98]. The scintillating core has an index of refraction $n_c = 1.6$, with the first and second layers of cladding having $n_1 = 1.49$ and $n_2 = 1.42$. A simple schematic of the fibre is shown in Fig. 4.1.
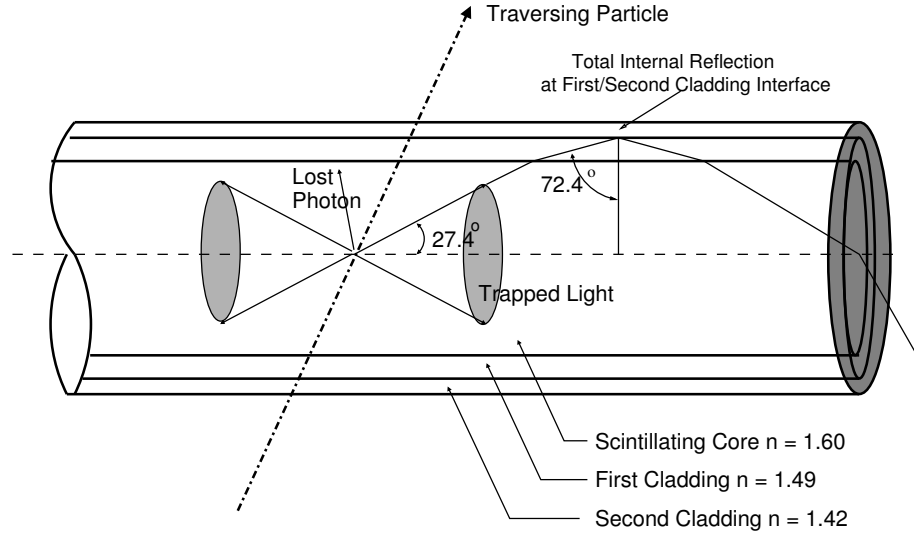
Figure 4.1: A simple schematic of a standard double-clad fibre showing the trapping of optical light for meridional rays. Adapted from Ref. [98].

4.1.1 Trapping Efficiency

The trapping efficiency for forward propagating photons is defined as the fraction of the photons produced in scintillation that are trapped by total internal reflection within the fibre. Fig. 4.1 is a simple representation of light propagating in the fibre when produced on the axis of the fibre. These light rays are referred to as *meridional* rays. However, since the path of the charged particle passing through the fibre will produce light that does not propagate on a plane which includes the fibre axis, the description becomes much more complicated. Ref. [108] discusses the trapping of

light in fibres in great detail and includes these off-axis rays. It is necessary to define an angle γ as the angle of the projection of the light ray in a plane perpendicular to the axis of the fibre with respect to the normal at the point of reflection. One may describe γ as a measure of the *skewness* of a particular ray, since meridional rays have this angle equal to zero. The polar angle, θ, is defined as the angle of the light ray in a plane containing the fibre axis and the point of reflection with respect to the normal at the point of reflection.

Using the expression given by Potter *et al* [109] and setting the transmission function, which parameterises the light attenuation, to unity, the light flux can be written as follows:

$$
\begin{aligned}
F &= F_m + F_s \\
&= 4\rho^2 \int_{\theta=0}^{\theta_{crit}} \int_{\gamma=0}^{\pi/2} \int_{\phi=0}^{\pi/2} I(\theta, \phi) \cos^2 \gamma \, d\gamma \, d\Omega \; + \\
&\quad 4\rho^2 \int_{\theta=\theta_{crit}}^{\pi/2} \int_{\gamma=\overline{\gamma}(\theta)}^{\pi/2} \int_{\phi=0}^{\pi/2} I(\theta, \phi) \cos^2 \gamma \, d\gamma \, d\Omega \; ,
\end{aligned}
\tag{4.1}
$$

where $d\Omega$ is the element of solid angle, $\overline{\gamma}(\theta)$ refers to the maximum axial angle allowed by the critical angle condition, ρ is the radius of a cylindrical fibre and $I(\theta, \phi)$ is the angular distribution of the emitted light in the fibre core. F_m and F_s, refer to either the meridional or skew cases, respectively where meridional rays pass through the central axis of the core and skew rays do not.

Assuming $I(\theta, \phi)$ is an isotropic distribution of the light in the core, the first term of Eq. 4.1 gives the trapping efficiency in the meridional approximation,

$$
\eta_m = \frac{F_m}{F_0} = \frac{1}{2}(1 - \cos\theta_{crit}) \approx \frac{\theta_{crit}^2}{4} \; ,
\tag{4.2}
$$

where all photons are considered to be trapped if $\theta \leq \theta_{crit}$, independent of their actual skew angles. F_0 is the total flux through the cross-section of the fibre core.

The integration of the second term of Eq. 4.1 gives the contributions of all skew rays to the trapping efficiency.

Complex integration leads to the result:

$$\eta_s = \frac{F_s}{F_0} = \frac{1}{2}(1 - \cos \theta_{crit}) \cos \theta_{crit} \; . \tag{4.3}$$

The total initial trapping efficiency is then:

$$\eta = \eta_m + \eta_s = \frac{1}{2}(1 - \cos^2 \theta_{crit}) \approx \frac{\theta_{crit}^2}{2} \; . \tag{4.4}$$

This is about twice the meridional approximation, $\sim 11\%$. However, skew rays have much longer optical path lengths, suffer from more reflections and therefore are attenuated more quickly. As well, the trapping efficiency of a ray is very much dependent on the circular symmetry of the core-cladding interface. Any variation in the eccentricity of the fibre diameter will lead to the refraction of some skew rays and loss of light. For this reason, far from the source, a long fibre will typically have a trapping efficiency closer to η_m. Literature typically quotes the trapping efficiency for a circular fibre as having a *minimum* trapping efficiency for the reasons stated above. A double clad fibre used in GLUEX can then be expected to have a minimum trapping efficiency of 5.3% after a long distance from the source and a maximum of 10.6% near the source. This effect will contribute to the bulk attenuation length of the fibre but will be difficult to separate from other attenuation effects.

4.1.2 Chemical Composition and Optical Spectra

The chemical and optical properties of scintillating materials have been presented elsewhere [110–112] and are recounted briefly herein. Such materials are composed of a chemical base, usually polystyrene or polyvinyltoluene, and one or more dyes that are added to improve the quantum yield of the scintillator and to waveshift the scintillation light to longer wavelengths with higher attenuation lengths [113]. The waveshifting properties are desired in order to reduce the impact of the degradation of the optical properties of the polymer due to ionizing radiation. Ionizing radiation has been seen to increase the absorption of light in the base polymers for wavelengths up to 500 nm.

The fluorescence mechanism responsible for scintillation light occurs in the base polymers and the additive dyes. The mechanism involves three main processes [114]. In the first step, ionizing particles passing through the scintillating fibre excite the polymer molecules. Shifting of the π-electrons[2] into excited singlet states is the major excitation process. In the second step, the energy is transfered from the excited state of the polymer to the primary dopant through the Förster mechanism [115]. This process is described by a dipole-dipole interaction in which a non-radiative energy transfer occurs between the excited polymer state and the primary dopant. In the third step, the primary dopant transfers its excitation energy to the secondary dopant through the emission of a photon which subsequently de-excites by emission of a photon. The net result of the process is a photon transmitted from the scintillating fibre with a wavelength that has a long attenuation length, and that photosensors are generally sensitive to.

It is the latter step that produces fluorescence, or scintillation light [110]. The

---

[2]Electrons which are in a p-orbital and form a weakly bound state by overlapping with a nearby electron, also in a p-orbital, are sometimes refered to as π-electrons.

scintillation material itself suffers from light absorption and has a quantum yield of a few percent only. Primary dyes have quantum yields typically over 80% and their optimum concentration in the mixture is about 1% by weight [110, 111] but are also subject to self-absorption. A secondary dye, in a much lower concentration (around 0.01%), resolves this issue of self-absoption by quickly absorbing the primary emission and waveshifting it to a longer wavelength. The concentrations of the primary and secondary dopants are sufficiently small to neglect their direct excitation. This process "extends" the primary attenuation length from a few cm up to several meters, and indeed SciFi's emit in the blue or green regions with attenuation lengths over 3.5 m. Moreover, the concentrations of the dyes can be tuned to achieve either higher light yield at the expense of attenuation length, or the reverse.

The attenuation length depends on the self-absorption of the materials and reflection losses as the photons travel down the fibre [116]. This is illustrated in manufacturer's absorption and emission spectra for the second dye in BCF-12 and BCF-20 fibres as shown in Fig. 4.2 (also shown are the stimulated wavelengths from the two light sources used in our experiment.) The overlap between the absorption and emission spectra in Fig. 4.2 is minimal, thus resulting in long attenuation length for these fibres. The integral of the transmitted light intensity decreases linearly as a function of the distance that the light travels in the fibre, i.e. there is an exponential loss of photons. The various wavelength regions exhibit differing slopes in these curves, with the shorter wavelengths following steeper slopes [110].

An important issue in the data analysis is the normalization of the light produced at the source, corresponding to near-zero fibre length. To this end, manufacturers' source spectra were examined and compared to our nearest measurements (1 mm fibre length). The properties of PHT-0044 and BCF-12 are quite similar, in terms
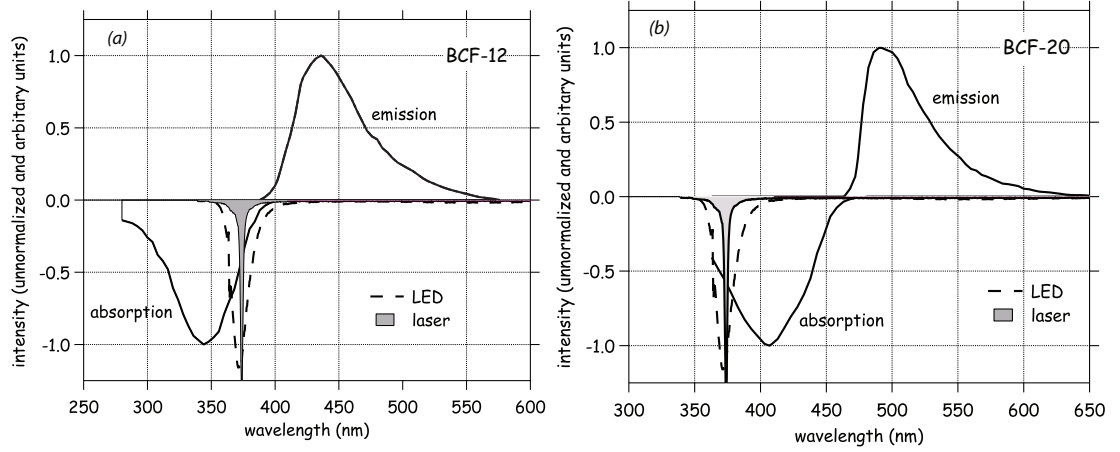
Figure 4.2: Emission and absorption spectra from the secondary dye of (a) BCF-12 and (b) BCF-20 fibres. Although BCF-12 fibres were not used in this study, their spectrum is similar to other blue-emitting fibres such as the PHT-0044 used herein, and is shown here for qualitative purposes. Also displayed are the stimulated wavelength ranges from the 373 nm LED and 375 nm laser used in our measurements, as discussed below. All curves have been arbitrarily normalized to facilitate the comparison of their spectral shapes. Figure taken from Ref. [117]

of peak emission and attenuation length. Source spectra are not available for the former, and this is why the BCF-12 spectra were used instead.

4.1.3 Measurements

For the measurements reported herein, an LED light source, a spectro-photometer and the tested SciFi were coupled together in a robust and reproducible manner (discussed later in this section). The SD2000 dual-channel fibre optic spectro-photometer[3] is based on a blazed diffraction grating with a 50 μm wide slit and features a high-sensitivity 2048-element linear CCD array that provides high response and excellent optical resolution from 200-1100 nm. This device had been calibrated by the manufacturer, and the provided specifications indicated a wavelength difference, $|\delta\lambda|$, between expected and measured values, never exceeding 0.3 nm for any given pixel

---

[3]Ocean Optics Inc., Dunedin, FL, USA (www.oceanoptics.com)

on the CCD. The SD2000 employs an external ADC1000-USB A/D converter to communicate with a PC running commercial software. The spectro-photometer had an integration window of 150 μs and measured the wavelength region of 340-1020 nm in over 2000 bins, resulting in a resolution of $\sim$3.3 bins/nm (or 0.3 nm). As a result, although the spectral shapes appear jagged at each wavelength, upon close inspection the overall behaviour of the data was stable, as evidenced by their long-wavelength tails that overlapped above 500 nm as expected, since at those wavelengths there is little absorption of light. This feature will be demonstrated below. Sample dark spectra were obtained and these had negligible effect on the measured spectra with UV light.

The LED light source used in the measurements was an RLU370-1.7-30 ultra violet LED[4], with a peak emission wavelength of 373 nm, a spectrum bandwidth of 13 nm, and typical radiant flux of 1.7 mW. Selected measurements were also performed using a 375 nm PicoQuant PDL 800-B picosecond pulsed diode laser with LDH-P-C-375B laser head[5]. A comparison of the spectra from the LED and the laser, as measured directly with the spectro-photometer, are shown in Fig. 4.3. These demonstrate that: a) the spectro-photometer had been correctly calibrated versus wavelength by its manufacturer, since the peak emission of the LED and the laser indeed were measured to be at 373 nm and 375 nm, respectively, and the peak widths were 13 nm and 1 nm, in agreement with manufacturers' specifications; b) There is no significant contribution from these light sources to the intensity of the measured fibre spectra in the wavelength range of interest, since the broad LED peak at $\sim$560 nm is only at the few percent level and does not fall in the excitation region of the fibres. In any case, this peak does not appear in the fibre spectra when the

---

[4]Roithner Lasertechnik,Vienna, Austria (www.roithner-laser.com)

[5]PicoQuant GmbH, Berlin, Germany (www.picoquant.com)

LED is positioned perpendicularly to the tested SciFi. The spectro-photometer was also used to measure the spectra of other LEDs at 470 nm and 590 nm and was found equally accurate.
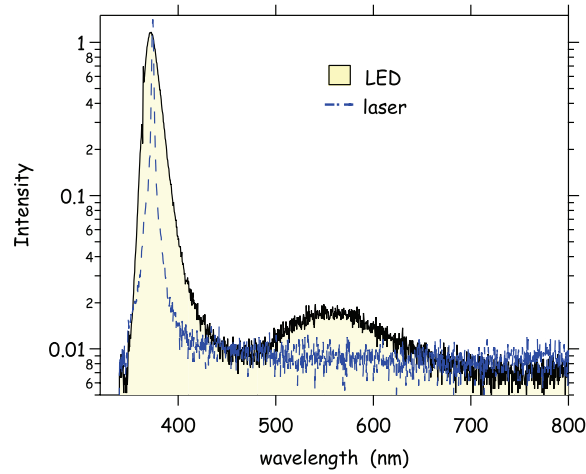
Figure 4.3: Comparison of the emission spectra of the LED and the laser as measured directly, using the spectro-photometer, and plotted on a logarithmic scale. Details are provided in the text. *(original in colour)*

The fibre under test was clamped in place horizontally until it was taut, with one end held via a clamp on a lab stand while the other was glued through a SMA connector using BC-600 epoxy. Once the glue had cured, the fibre end at the tip of the SMA connector was polished using three progressive grades of polishing paper (coarse, 12 μm and 3 μm grit) and a polishing puck, from a Clauss[6] fibre Optic Polishing kit (PK-2000), and was cleaned using ethyl alcohol and KimWipes to remove metallic dust originating from the tip of the SMA connector. Finally, the SMA end was coupled to the spectro-photometer's slave channel. This method allowed for easy and reproducible coupling of fibre to spectro-photometer. The setup was made robust to protect against displacing the test fibre and was levelled to avoid any curvature in the test fibres.

---

[6]The PK-2000 can be obtained from a large number of fibre accessories vendors.
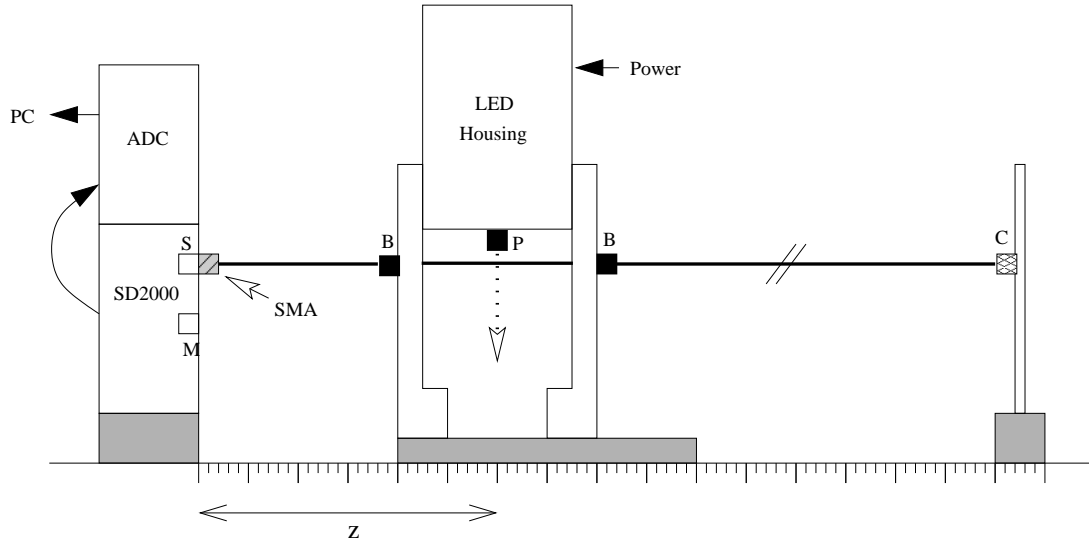
Figure 4.4:   Schematic drawing of the fibre experiment. The test fibre is shown as the bold horizontal line: on the right it is clamped to a lab stand (C), in the middle it threads through the legs of the LED support stand via barrels (B) having 1 mm inner diameter holes and external threads that mount on the support frame and on the left it is connected to the slave channel (S) of the SD2000 spectro-photometer by an SMA connector. The SD2000 connects to the ADC via a flat-ribbon bus and the ADC, in turn, connects to a PC via a USB cable. The vertical arrow pointing downwards from the LED housing indicates the direction of the incident light through its port (P) onto the test fibre. The horizontal displacement of the light direction to the entrance of the SD2000 master channel is our distance parameter, z. This figure is not to scale: for example, the LED's port is a lot closer to the fibre than implied in this schematic.

The LED was installed in a commercial housing and was mounted on a specially designed stand that could slide on the lab bench and translated across the length of the fibre (from 8 cm to 380 cm) in a parallel fashion, guided by a set of aligned, steel ruled guides. A schematic drawing of the setup is shown in Fig. 4.4. It should be noted that in that figure the distance of the LED housing port (P) to each fibre tested was 3 mm and held constant to maintain a consistent beam profile. With this setup, relative comparisons of the measured light intensity along the length of a given fibre were possible. However, due to the different level of polish of each fibre, absolute comparisons from one fibre to another were not possible for the measured intensity, although the spectral shapes were unaffected and could still be compared.

All measurements were carried out in near darkness in our lab. However, since the core of blue-emitting scintillating fibres can be damaged by prolonged exposure to UV light, yellow, UV-absorbing film (TA-81-XSR[7]) was used to cover all fluorescent overhead and incandescent desk lights in our detector test laboratory during the preparation and setup stages.

4.1.4 Results

4.1.4.1 Fitting the Emission Spectra

The measured spectra for the BCF-20 are well described by a Moyal function plus a flat background:

$$f(x, a, \mu, \sigma, b) = a \cdot \exp\left(-\frac{1}{2}\left(\frac{(\lambda - \mu)}{\sigma} + e^{-(\lambda - \mu)/\sigma}\right)\right) + b. \qquad (4.5)$$

---

[7]Window Film Systems, London, ON, Canada (www.windowfilmsystems.com)

On the other hand, the PHT-0044 fibre spectra require a sum of two Moyal functions plus a flat background. The Moyal distribution is often used as a good approximation to the Landau distribution [118], and was chosen here as the description with the fewest fit parameters; in any case, it was employed simply as a tool to integrate the spectra and proceed further in the analysis. The results of fits to Moyal functions for spectral measurements at LED distances ranging from 8 to 380 cm for both fibre types are shown in Fig. 4.5.
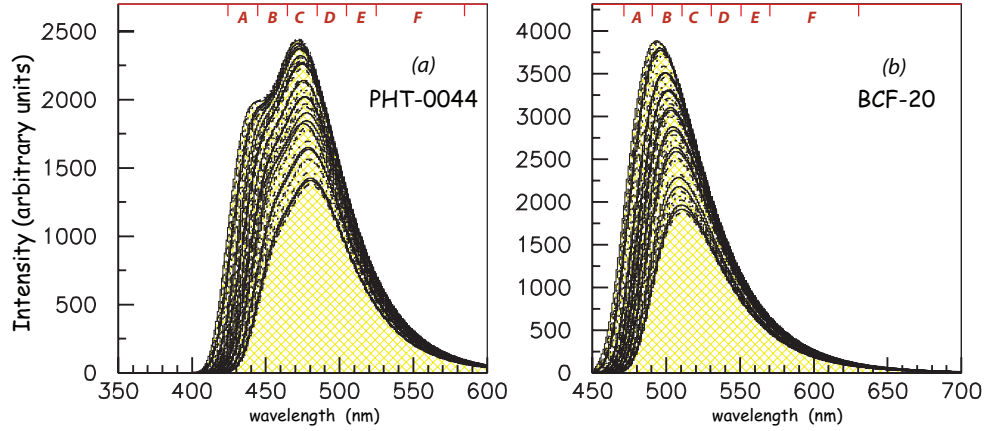
Figure 4.5: The results of fits to Moyal functions for spectral measurements at source distances ranging from 8 to 380 cm for (a) PHT-0044 and (b) BCF-20 fibres. The wavelength ranges labelled A through F in the plots will be referenced later in this paper.

The single Moyal function fits have four parameters including an amplitude (a), a characteristic wavelength and width (given by μ and σ) and the background term (b). The fits involving a sum of two Moyal functions introduce three additional parameters. The BCF-20 fibre spectral fits are characterized by a single wavelength (μ) and width (σ) and the PHT-0044 fits are characterized by two wavelengths (μ_1 and μ_2) and corresponding widths (σ_1 and σ_2). The dependence of these fit parameters on LED distance is shown in Fig. 4.6. The integral of the background term over wavelength from 400 to 700 nm is about 5% of the integral of the spectra over this

same wavelength range.
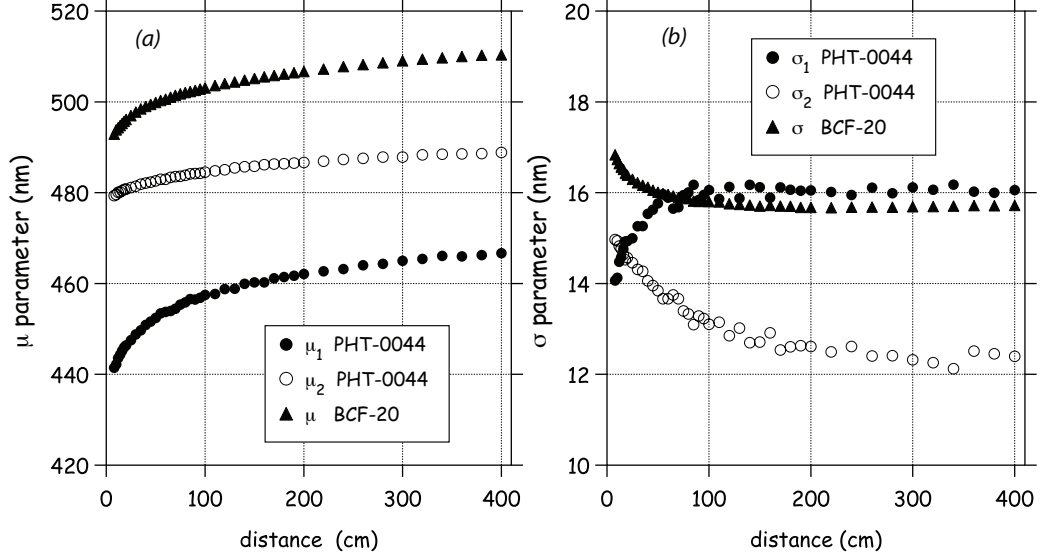
Figure 4.6: Dependence of the Moyal fit parameters (a) μ and (b) σ as a function of source distance for the PHT-0044 and BCF-20 fibres.

4.1.4.2 Attenuation Length versus Wavelength

The Moyal fits described above were integrated over wavelength for the two fibres for various source distances. Six ranges of wavelength (labelled A through F) over which the integrals were performed are indicated in Fig. 4.5 for the two fibres. The central (middle of each bin) wavelengths are indicated in the legend of the plots in Fig. 4.7. These data were fit to an exponential of the form:

$$I(d) = I_0 + \alpha \cdot e^{-(d-d_0)/\lambda} \tag{4.6}$$

For the fits shown, the floor term, I_0, was set at about 10% of the maximum value for the data in a particular wavelength range. Without the inclusion of a floor term, consistent single-exponential fits could not be obtained; this term does not originate
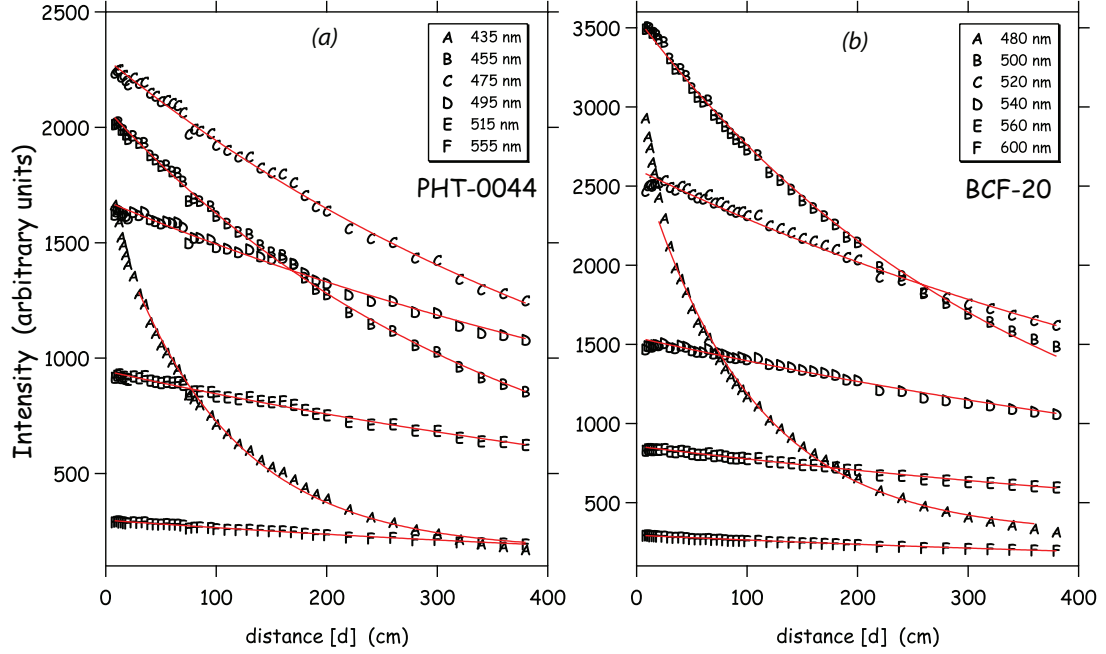
Figure 4.7: Integrals of the Moyal fits to the fitted data are shown as a function of source distance for (a) the PHT-0044 and (b) the BCF-20 fibres. The points labelled A through F are the integrals for the wavelength ranges defined in Fig. 4.5. The curves are results of fits to a single exponential. More details are given in the text.

from a spectrophotometer calibration but is most likely due to spectrum fluctuations as a result of the method of illuminating the fibres. The d_0 was not a fit parameter, but rather was determined by the starting point of the fit, which was $d_0 = 8$ cm for all the wavelength ranges except for the wavelength range labelled A, which required a $d \geq 8$ cm in order to obtain a good quality fit due to the rapid absorption at small wavelengths. The fit parameter λ is the attenuation length and its dependence on wavelength for the two fibres is shown in the left panel of Fig. 4.8. Such behaviour was first reported in reference [110].

The attenuation lengths in the right panel of Fig. 4.8 were obtained by plotting the value of the Moyal fit function as a function of distance at discrete wavelengths and fitting to an exponential. Note the structure in this dependence around 460 nm
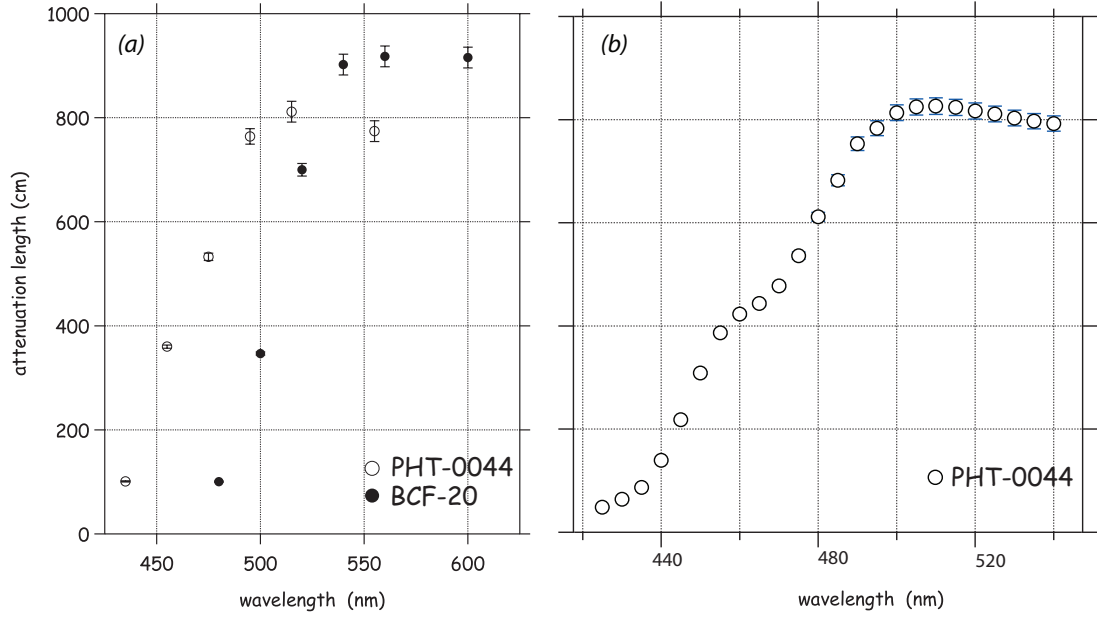
Figure 4.8: (a) The attenuation length as a function of wavelength for the PHT-0044 and BCF-20 fibres. The attenuation length is the parameter λ as defined in Eq. 4.6 and is obtained by fitting the data shown in Fig. 4.7. (b) The attenuation length as a function of wavelength as extracted by plotting the value of the Moyal fit function as a function of distance at discrete wavelengths and fitting to an exponential. Note the structure in this dependence around 460 nm.

to 470 nm that corresponds to the region of the second peak in Fig. 4.5. This is a persistent feature and not an artifact of our measurements or the spectro-photometer response, and shows faintly in the left panel of Fig. 4.8 due to the lower resolution in that method.

4.1.4.3 Fibre Spectral Shape Details

The spectral shapes of the PHT-0044 and BCF-20 fibres differ significantly, as can be seen in Fig. 4.5. The striking difference between the PHT-0044 and BCF-20 fibres in terms of the loss of light from the source to 8 cm distance is illustrated in a graphical manner in Fig. 4.9. In that figure, the d=0 cm and 8 cm spectra are shown as a function of wavelength, normalized at 490 nm and 590 nm for the

PHT-0044 and BCF-20 fibres, respectively. The emission spectrum at the source $(d = 0$ cm) for the PHT-0044 fibre was assumed to follow the emission spectrum for BCF-12 as mentioned previously; that and the source spectrum for BCF-20 were provided by the manufacturer. This normalization was based on a combination of long attenuation length and sufficient intensity at each wavelength. With attenuation lengths of ~800 cm and ~900 cm at 490 nm and 590 nm, respectively, as extracted from Fig. 4.8, the effect of 8 cm in loss of strength is negligible. In addition, variations in the regions around these values resulted in stable ratios of areas under the spectral shapes, further emphasizing the lack of sensitivity to the exact normalization choice.
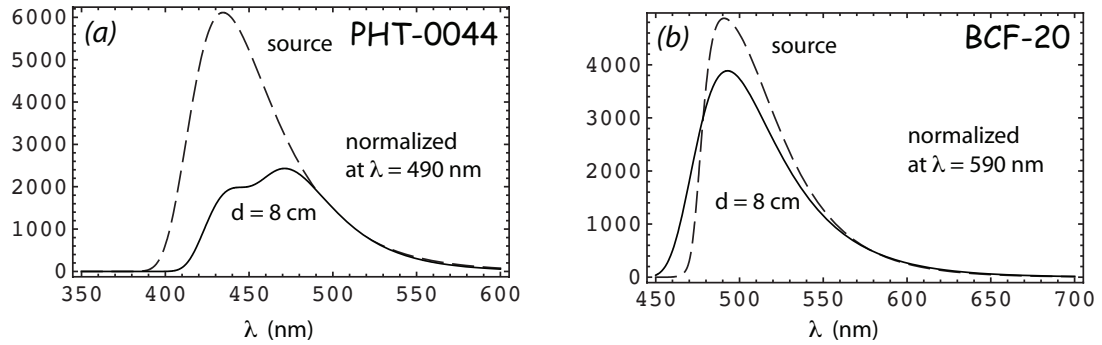
Figure 4.9: The manufacturer's $d{=}0$ cm source (dashed line) and 8 cm spectra (solid line) are shown, as a function of wavelength for (a) the PHT-0044 and (b) BCF-20 fibres, respectively. Details are presented in the text. Figure taken from Ref. [117]

The main features of Fig. 4.9 are: a) large loss of light from source to 8 cm for PHT-0044 as compared to the BCF-20 fibre and quantified in Section 4.1.4.4, and b) a curious discrepancy between the source and 8 cm curves for the BCF-20 is apparent, where the latter extends to lower wavelengths. No firm explanation of this was found. However, a close inspection of the leading edge of the source shows a rather rapid (and unnatural in appearance) rise from its 470 nm base to its 490 nm peak. A possible explanation is that the manufacturer may have used a bandpass or some other type of filter to block the blue wavelengths of a UV light source.

Our experimental setup used for the measurements, as presented in Section 4.1.3, did not allow measurements closer than 8 cm from the source. Therefore, in order to further investigate the double-peaked behaviour of the PHT-0044 spectra and to facilitate comparisons to the manufacturer's source spectra, we employed an alternate setup using the laser. In that, the laser light was transported via a clear optical fibre held by a clamp and a lab stand so as to be perpendicular to the tested PHT-0044 fibre, in a manner similar to the LED measurements. In this manner, a short sample (15 cm) of PHT-0044 fibre was tested by coupling it to a clear (BCF-90) 5 cm-long fibre using Q2-3067 optical grease[8], with both fibres positioned in a channel of a plate so as to remain in contact and axially aligned. The clear fibre was threaded and epoxied through a SMA connector and facilitated proximity measurements of the PHT-0044 by bridging the gap from the spectro-photometer's SMA connector to the CCD surface. In this manner, PHT-0044 spectra were collected at distances from 1 to 20 mm in 1 mm steps, from 20 to 60 mm in 5 mm steps and at 100 mm. The latter point provided an "anchor point" to the LED data, since the two measurements had different setups. Indeed, it was reassuring to observe that the LED- and laser-stimulated PHT-0044 spectra at 10 cm were consistent.

Having assured the reliability of the laser measurements, the resultant spectra are shown in Fig. 4.10, normalized at 500 nm. Normalization at other wavelengths was carried out, but the 500 nm normalization was the most consistent one, since the high-wavelength tails of all distance measurements overlapped perfectly, and no large discrepancies appeared at the two peaks.

The spectra at distances of a few mm's from the excitation source should closely match the "source spectrum" provided by the SciFi manufacturers. For PHT-0044 (and BCF-12), however, the peak emission is listed by them at 435 nm with no evi-

---

[8]Dow Corning Corporation, Midland, MI, USA (www.dowcorning.com)
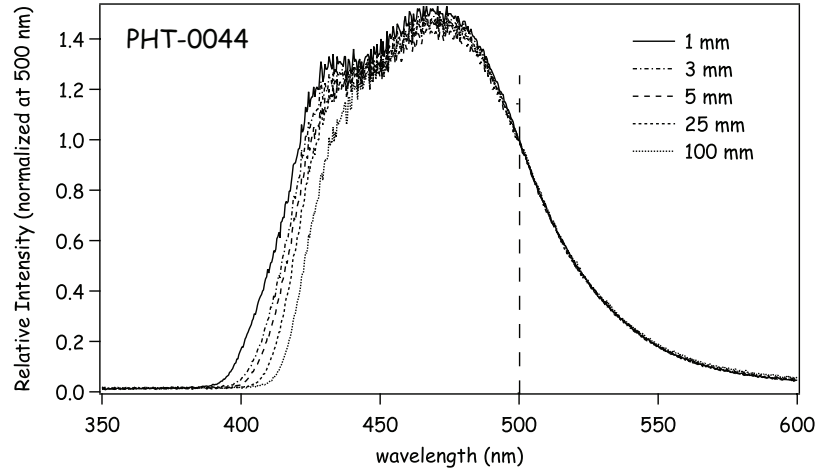
Figure 4.10:   Measurements from a short sample of PHT-0044 fibre using the UV laser. Spectra were collected at distances from 1 to 20 mm in 1 mm steps, from 20 to 60 mm in 5 mm steps and at 100 mm, but only five of them are shown for reasons of clarity. The spectra were normalized relative to each other at the wavelength value of 500 nm.

dence of secondary strength at 460-470 nm. Our measurements are in disagreement to those reference spectra: while some strength is evident at 435 nm, the peak emission is at 460-470 nm, instead. One explanation may lie in the attenuation length measurements, shown in Figs. 4.7 and 4.8. The attenuation length at 460 nm is ~400 cm, compared to ~80 cm at 435 nm. Thus, if the source spectrum has secondary emission strength around 460-470 nm, the reduced attenuation of the latter compared to the former can result in the double-peak structure observed in our measurements. It is worth noting here that the blue emitting fibres in reference [110], the equivalent fibre types from Kuraray (SCSF-81 and SCSF-81M)[9], and several blue-emitting plastic scintillator data (BC-400, BC-404 and BC-408 from St. Gobain as well as EJ-200 from Eljen[10]), all show a "shoulder" in the source emission spectra in the region of 460-470 nm.

---

[9]Kuraray America Inc., Houston, TX, USA (www.kuraray-am.com)

[10]Eljen Technology, Sweetwater, TX, USA (www.eljentechnology.com)

The significantly different attenuation lengths at 435 nm and 460-470 nm can easily provide the explanation of the structure observed in Fig. 4.5. However, the attenuation length for 435 nm cannot account for the weak strength observed at a few mm distance from the source location. Another mechanism must be responsible for the suppressed emission at the nominal peak wavelength of 435 nm. Taking into consideration that the reference spectra are generated within scintillation material thickness of 1 cm or more, it is possible that within the 1 mm diameter (maximum effective thickness) of the fibre the UV source does not fully excite the dyes, thus resulting in a reduced strength at the lower wavelengths. The 10 cm distance spectra for BCF-12 in reference [119] appear very similar to that shown in Figs. 4.5 of this work. The agreement between the reference spectra and our measurements for BCF-20 further indicates that this effect is indeed confined to lower wavelengths.

A quick calculation from our work shows that the resolving power, $R = \lambda/\Delta\lambda$, of our LED and laser is 28.6 and 375, respectively. Coupled to the aforementioned spectro-photometer resolution of 0.3 nm, these values result in a very fine resolution in wavelength, that does not appear to be the case for the results in reference [120], which is perhaps why the second peak appears to be washed out in their work and other published data.

4.1.4.4   Scintillating Fibre/Photosensor Matching

The fibre spectra of intensity versus wavelength in Fig. 4.11a were convoluted with the spectral response of a typical bi-alkali PMT (the XP2020[11]) and a silicon-based photomultiplier (SiPM) – (the A35H SiPM[12]) in Fig. 4.11b, respectively, resulting in the curves shown in Fig. 4.11c and Fig. 4.11d. The objective was to model a realistic

---

[11]PHOTONIS SAS, Brive, France (www.photonis.com).
[12]A prototype SiPM from SensL with a 35μm pixel pitch.

situation in an experiment.

Specifically, the PHT-0044 and BCF-20 spectra were convoluted over wavelength with the XP2020 quantum efficiency (QE) and SiPM photon detection efficiency (PDE), respectively, and were plotted as a function of distance from the source. Double-exponential fits were employed with two attenuation lengths (short and long). Note that when the PHT-0044 spectrum is folded with the XP2020 QE, the fraction of the integrated source intensity (see Fig. 4.9a) seen at 200 cm from the source is 24%, while the corresponding fraction for the BCF-20 with the A35H is 61%. Since the QE and PDE are relatively flat in the region of interest, these fractions reasonably describe the actual loss of light in the fibres. One can conclude that, whereas the integrated intensity of the PHT-0044 fibre coupled to the XP2020 is superior to that of the BCF-20 fibre, the results are indistinguishable when the fibres are coupled to the SiPM, only if one considers the data in the $d = 8\text{-}380$ cm region, and not from the source.

The wavelength-averaged QE of the XP2020 and PDE of the A35H SiPM were computed using the emission spectra of PHT-0044 and BCF-20. The integrals of these spectra over wavelength were computed as a function of distance, with and without convolution with the QE (or PDE), by dividing the integral with convolution by the integral without convolution. The results are shown in Fig. 4.12. For PHT-0044, at 200 cm from the source, the average QE of the XP2020 is 15% and that of the A35H is 14%. For BCF20, at 200 cm from the source, the average QE of the XP2020 is 9% and that of the A35H is 14%.
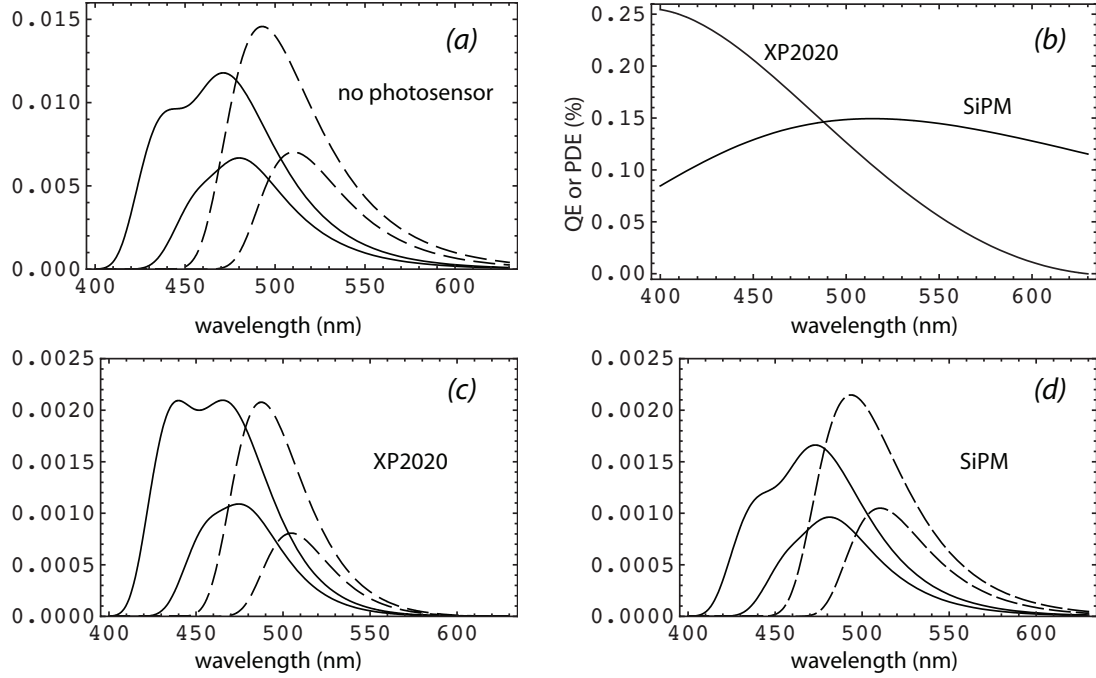
Figure 4.11: (a) Emission spectrum for the PHT-0044 (solid lines) and BCF-20 fibres (dashed lines) at 8 cm and 390 cm. The 8 cm spectra for both the blue and green fibres were normalized to give unity for the respective total integrals. (b) The QE and PDE for the XP2020 and SiPM respectively. (c) The PHT-0044 and BCF-20 spectra now convoluted with the QE of the XP2020. Note that the areas under the curves for the 8 cm distance are set to 1.0 in plot (a), which results in areas under the PHT-0044 spectra of 0.164 and 0.068 while those under the BCF-20 curves are 0.110 and 0.040, both in plot (c). (d) Similar curves, but now convoluting with the PDE of the SiPM. The areas under the PHT-0044 curves are 0.136 and 0.067 while for the BCF-20 curves we have 0.145 and 0.065.
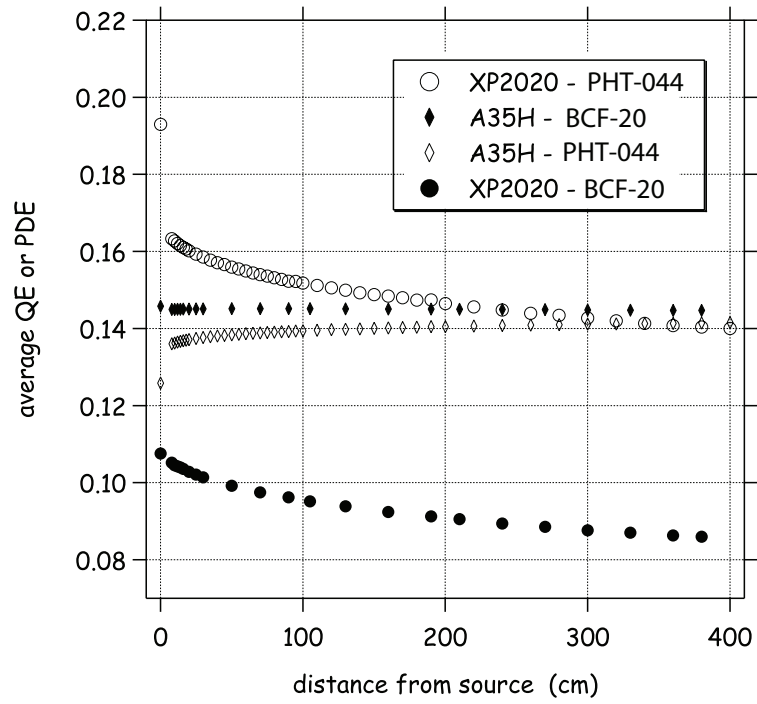
Figure 4.12: The average QE of the XP2020 and the average PDE of the A35H, as a function of distance from source for PHT-0044 and BCF-20 scintillating fibres, are shown. Details are given in the text.

4.1.4.5   Attenuation Length with and without Photosensor

As can be seen in Fig. 4.7. the light output of a fibre is strongly dependent on λ and d, with shorter wavelengths that dominate at small distances being replaced by longer wavelengths at larger distances. However, the bulk attenuation is the result of the integrated light yield and, being the convolution of two different response regions, cannot be effectively represented by a single exponential function. Therefore, each fibre was characterized by [121]:

$$I(d) = I_0 + \alpha_1 \cdot e^{-(d-d_0)/\lambda_1} + \alpha_2 \cdot e^{-(d-d_0)/\lambda_2} \qquad (4.7)$$

The values from this fit are shown in Table 4.1. Using this information, the attenuation length for PHT-0044 and BCF-20 was plotted with and without the photosensor coupling in Fig. 4.13. The weighted attenuation length in that table is based on the relative amplitudes of the two exponentials.

	Without Photosensor		With Photosensor	
Component	PHT-0044	BCF-20	PHT-0044	BCF-20
short (cm)	50±14	48±8	43±8	50±9
long (cm)	478±21	481±21	414±14	491±21
weighted (cm)	428±23	400±23	353±18	408±25

Table 4.1:   Short and long attenuation length components for the PHT-0044 and BCF-20 fibres, as extracted from a double-exponential fit. The weighted attenuation length is based on the relative amplitudes of the two exponentials. The photosensor in the case of PHT-0044 is the XP2020 and in the case of BCF-20 is the SiPM.

The long bulk attenuation length of 414 cm for the PHT-0044 fibre combined with the XP2020 agrees well with the specification supplied by the manufacturer, which was extracted using a ^{90}Sr electron source and a bi-alkali vacuum PMT. Those measurements were made between 64 cm and 200 cm and are dominated by the

long component[13]. For the BCF-20 fibre, on the other hand, the manufacturer's specification was derived using bi-alkali PMT's and our results cannot be compared directly to those. However, the smoothly varying and relatively flat QE response of a PMT over the emission spectrum of BCF-20 (approximately 460 nm to 560 nm; see Figs. 4.11b and 4.12) will not alter the weighted attenuation length of 408 cm, and St. Gobain quotes a value larger than 350 cm. In conclusion, our measurements using UV light sources and a spectral deconvolution agree very well with the manufacturer's ones using an electron source, once the range of distance measurements are taken into consideration.

4.1.5   Fibre and Photosensor Match

The relevant quantities in matching SciFi's to photosensors are the emission spectra of the former and the spectral response of the latter because this combination affects the number of photoelectrons generated independent from attenuation length. Changes in the spectral emission of the fibre with length affect the number of photoelectrons detected and introduces a non-linearity in the energy response of the detector system. The combination of SiPM's and fast green emitting SciFi's, such as BCF-20, in applications where the technology of the latter is relevant, is an optimal one due to the flat PDE response of the SiPM in the emission wavelength spectrum of the former and the stability of the peak emission wavelength of the SciFi, as seen in Fig. 4.11. Such combinations have already been reported in the literature [122].

Fast blue SciFi's are by far the most widely used fibres, in combination with bi-alkali type of vacuum PMT's. Most such fibres with peak emission at nominal 435 nm – examples of which are PHT-0044 (no longer produced), BCF-12 and SCSF-

---

[13]Information provided by PolHiTech (www.polhitech.it).
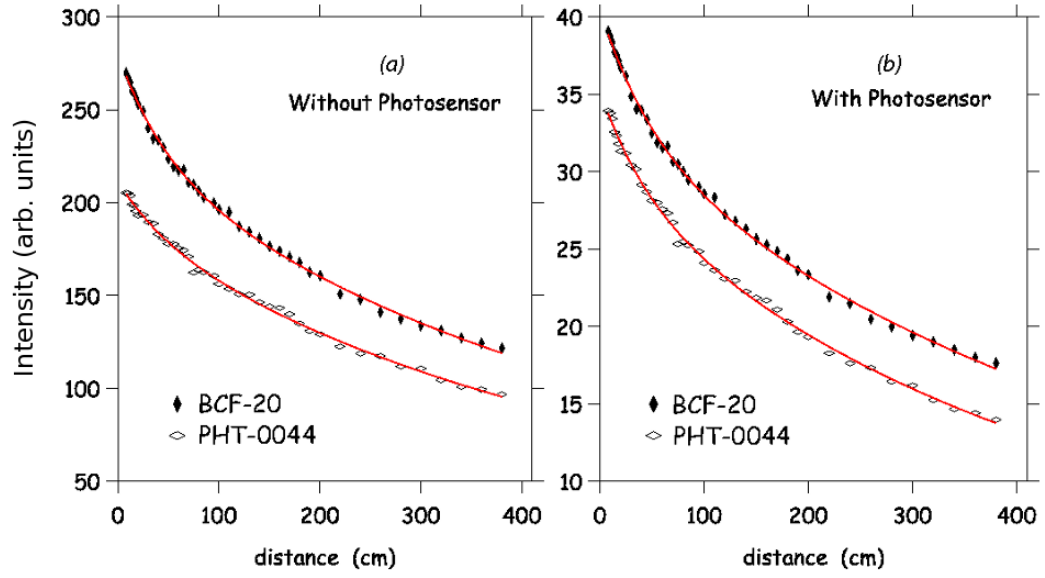
Figure 4.13: Double-exponential fits to the PHT-0044 and BCF-20 data without and with the convolution of the photosensor. The photosensor in the case of PHT-0044 is the XP2020 and in the case of BCF20 is the SiPM. The results of the fits are shown in Table 4.1.

81, all sharing very similar attenuation lengths and spectral functions. However, the testing of several different samples produced consistent emission spectra that are quite different than the manufacturers' specifications. In this work, the results are shown for only PHT-0044 fibres due to the large detailed amount of experimentation that we have done with that particular fibre type. The peak emission is not at 435 nm, which appears only as a secondary "bump", but at approximately 470 nm, instead. One possible explanation is that the thickness of the fibre presented to the exciting UV light (maximum 1 mm) is not adequate to absorb the UV light and to allow its full conversion to the emission spectrum representative of the material in sufficient thickness (as discussed in the preceding section). As such, the emission spectra in this thesis near the illumination centre, shown in Fig. 4.10, are the effective spectra we have measured for such types of fibres.

This observation leads to question the effective photon yield listed by most manufacturers of approximately 8,000 photons/MeV of deposited energy by minimum ionizing particles (MIP). If such a yield is the integral of the full emission spectrum, as listed in the product literature, then a significant fraction, approaching 50%, is not available for excitation by UV light, as shown in Fig. 4.9. Experimental results are consistent with such reduced photon yields. BCAL data with cosmic rays and photon beams verify that the nominal photon yield of 8,000/MeV has to be reduced by a significant fraction, over and above that justified by attenuation length and spectral distortion with distance, to account for the measured yield of 660 photoelectrons at 1 GeV incident photons [123]. The same treatment was applied to the KLOE results of 700 photoelectrons also at 1 GeV [124], taking into consideration the single-clad fibres used and the very efficient light guide-Winston Cone collectors used.

The conclusion derived here is that that our work explains the physics cause for

the commonly known fact that the measured number of photoelectrons from SciFi's do not reflect the manufacturers' number for scintillating material of 8,000/MeV. The actual number is closer to around 4,000 photons/MeV at the scintillation location for 1 mm diameter blue emitting fibre.

Using the methodology described in this thesis, it is concluded that the conversion of UV light in 1 mm of green (BCF-20) material is much more efficient than for blue fibres. The overlap of the reference and measured spectra in Fig. 4.9 is significant, indicating a small loss of photon yield due to conversion to the final emission spectrum. If this also represents the case of charged particle tracks in BCF-20 fibres, as the results for PHT-0044 indicate, then one expects a factor of approximately 2.5 times the photoelectron yield of the BCF-20/SiPM combination than obtained with the PHT-0044/PMT combinations.

It would be advisable for the manufacturers of scintillating fibres to show actual spectra obtained in such thin materials, rather than reference emission spectra than can only be realized in thicknesses beyond the realm of fibre use and availability, and to quote the effective number of photons per MeV of energy deposit (MIP) produced in fibres.

Finally, the attenuation lengths of both PHT-0044 and BCF-20 are in good agreement with specifications if the measurements duplicate the manufacturers' methodology. As such, both blue and green SciFi's exhibit comparable bulk attenuation lengths with or without the influence of the two corresponding types of photosensors used in our work.

4.1.6   Future Outlook on Fibres and Sensors

Improvements to spectrum measurements could be achieved by re-calibrating the sensitivity of the photospectrometer. A calibration has not yet been performed since the purchase of the photospectrometer, due the the inavailability of the required equipment. It has been suggested that the sensitivity of the detector to specific wavelengths of light may account for the difference in spectral shapes from the manufacturers spectra. However, the sensitivity of the detector will not change any conclusions about the attenuation lengths of the fibres as a function of wavelength as the *relative* change in intensity is used to determine this value. As well, only a large discrepancy (more than a few percent) in the relative sensitivity of the detector from unity will affect the bulk attenuation length measurements significantly. A lower sensitivity to the UV part of the spectrum will make the bulk attenuation length appear larger than it actually is.

Since this work was completed, the GLUEX collaboration has chosen SiPMs as the readout for the entire BCAL. Hammamatsu MPPC[14] (SiPMs) are likely to be chosen as they have better characteristics then SensL's[15]. Also, Kuraray SCSF-78MJ fibres are being used for production of the final BCAL modules with 400,000 fibres having already arrived at Regina, 1/2 of the total shipment of fibres, with the rest being produced or ready to be shipped. These fibres exhibit a peak emmision in the blue-green part of the optical spectrum with similar attenuation lengths to the BCF-20 and PHT-0044.

---

[14]http://sales.hamamatsu.com/en/products/solid-state-division/si-photodiode-series/mppc.php
[15]http://sensl.com/

4.2   Light-guides

The wavelength sensitivity matching of the light sensors to the fibres was described in the previous section. In this section, the light transport from the fibres to the light sensors will be presented.

Constructing an array of light-guides to read out the BCAL poses a geometrical and logistical challenge in trying to match the geometry and segmentation of the BCAL, described in Fig. 3.3 to devices for collecting the light. The work in this section focuses on a light guide design for the inner 12 cm of the BCAL, although it can easily be scaled for the outer segments. In all cases, the exit of the light-guide will be circular to match the geometry of the readout device, as well as provide better efficiency. To a first approximation, the inner segmentation was assumed to be square such that the entrance of the light-guides for readout can be square. This was done for simplicity in simulating, designing and constructing protype light-guides and will not affect the conclusions. The square design is approximate to the trapezoidal shape needed for stacking a 6×4 array of light-guides together to match the shape of the BCAL. The edges will require some slight degree of tapering in a final design to match the inner 12 cm of the 7.5° wedge shape of a BCAL module.

4.2.1   Non-Imaging Concentrators

The design of nearly all non-imaging concentrators are based on the edge-ray principle, namely that all rays with an entrance angle less than or equal to the maximum angle θ_{max} should leave the concentrator after one total internal reflection or "bounce". In general, light rays that suffer more than one bounce tend to be reflected back and exit out the entrance. With this principle in mind, the light-guide discussed here is designed so that all light rays exit after a single reflection. A simple cone

shape offers an uncomplicated design for a light concentrator, but it is not ideal, and has a lower efficiency than is desired as light rays that experience more than one bounce return as illustrated in Figure 4.14. However, the design discussed below will use a conic shape for slightly tapering one section as only single reflections are expected.
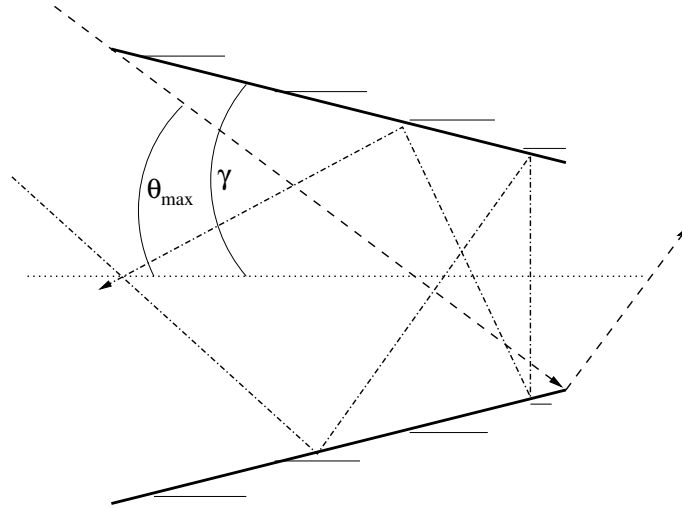
Figure 4.14: Non-imaging concentrator: A cone shape will turn back some rays if they reflect more than once.

An ideal or nearly ideal non-imaging light concentrator is a compound parabolic concentrators (CPC), otherwise known as a Winston Cone [125]. A Winston cone is an off-axis parabola of revolution designed to maximize collection of incoming rays within some field of view and has circular entrance and exit apertures by symmetry of their design. A schematic of the Winston cone is shown in Fig. 4.15. It maximizes the collection of incoming rays by allowing most off-axis rays to make multiple bounces before passing out the exit aperture. However, because of its circular entrance aperture, it is not a suitable match for the BCAL's geometry. Instead, by using a combination of geometries, a highly efficient light guide has been designed which has a square entrance and a circular exit.
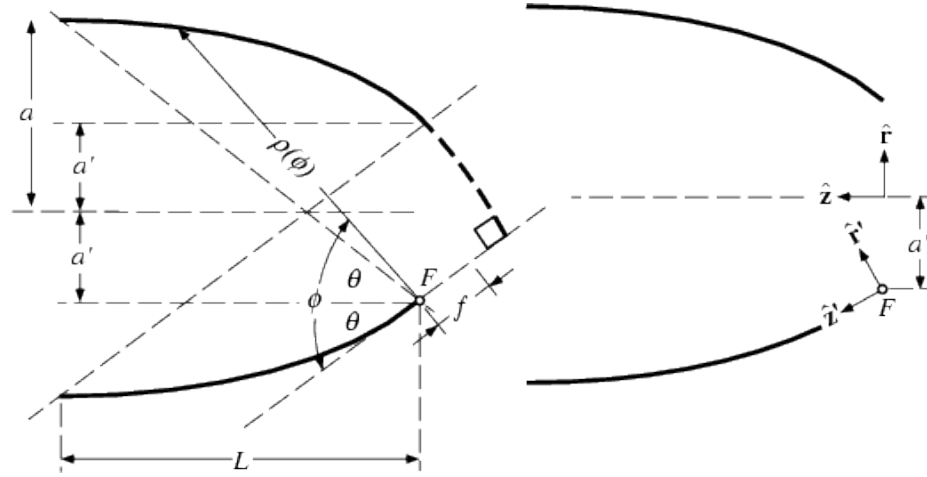
Figure 4.15: A schematic of a Winston cone (CPC). The entrance and exit apertures are of radius a and a' respectively. F is the focus of the upper parabola segments, and f is its focal length. The length of the cone is L. Image from [126].

4.2.2 Design

Assuming that the light-guide will be machined from an acrylic polymer, an index of refraction of 1.49 was assumed in the design that follows. The overall shape of the light-guide can be separated into two distinct segments: a conically tapered rectangular block (Segment A) and a Compound Parabolic Concentrator (CPC) (Segment B). As Liouville's Theorem places a limit on the maximum concentration of light of about 3:1 [125], the ratio of exit to entrance area is limited. A readout choice of a large area silicon photomultiplier with a circular area of 1.26 cm^2 falls near this limit, if the entrance window is 2×2 cm^2.

The light-guide's surface shape is the principle factor in reflecting light from the entrance aperture to the exit aperture. What follows will describe the surfaces needed to transport the light with a high efficiency. A sketch of the design is shown in Fig. 4.16. A 3D image rendering of a similar light-guide created with the open-source software package Blender[16] is shown in Figure 4.17.

4.2.2.1 Segment A

The surface of Segment A is derived from having a square entrance and a circular exit, described previously, so that a Winston cone can be attached to the circular face and the light can be concentrated with higher efficiency. The surface of Segment A is essentially a block with material removed from one set of corners where the surface of a cone would intersect the volume of the block such that the corners of the block are tapered down to a circular aperture. Some light concentration is done in this segment but its principle function is to guide the light to the circular exit aperture. The length of this segment is determined by the angle of the conical tapering. Any

---

[16]www.blender.org
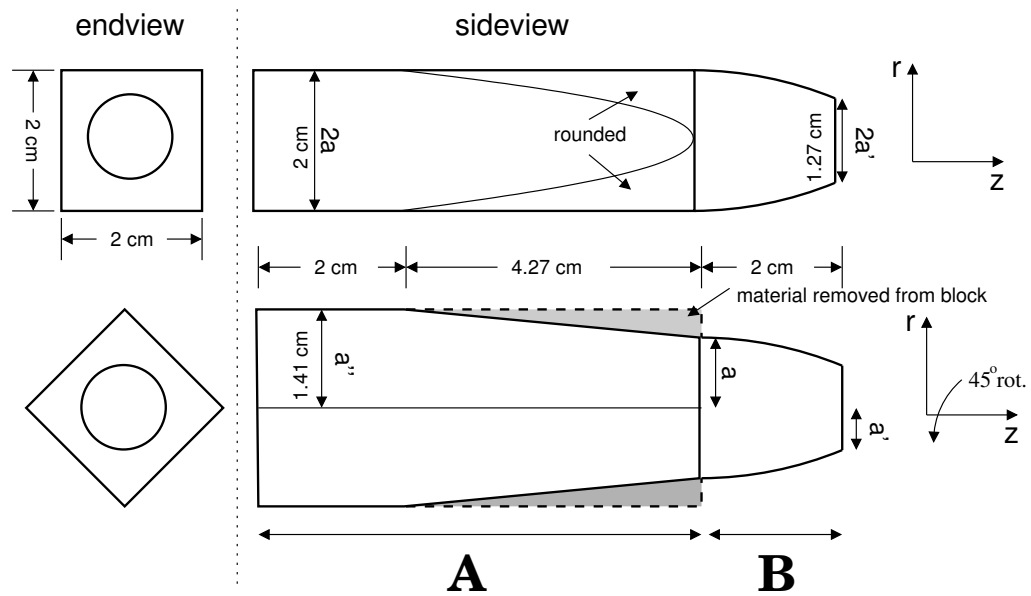
Figure 4.16: A sketch of the light guide. Top: side view. Bottom: side view but rotated 45° about z.
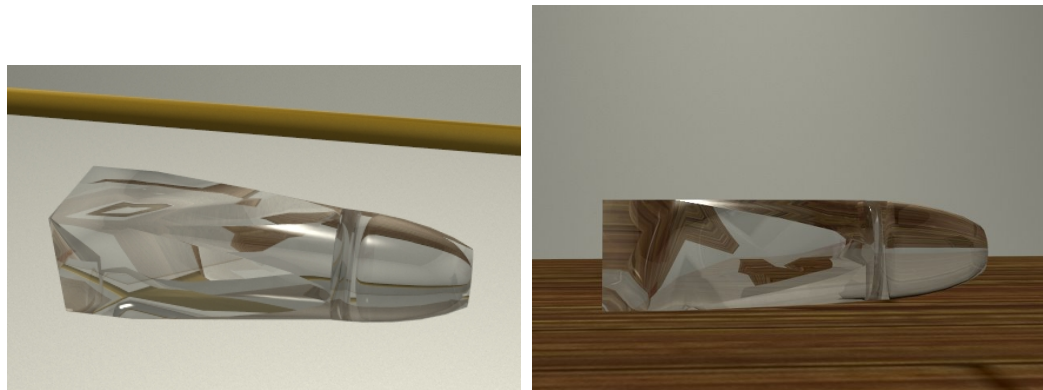
Figure 4.17: A 3D rendering of a light-guide. The dimensions used to create the drawing are not the final dimensions of the prototype but the image shows the overall shape more clearly than a simple sketch. *(original in colour)*

untapered portion near the entrance is arbitrary in length but is also useful for light source mixing and ease of mounting. This extra length (a few centimetres) does not significantly affect the performance, as the attenuation length of acrylic is on the order of a few metres.

The most important parameter of Segment A is the optimal tapering angle of the cone. The edge-ray principle dictates that this should be large enough that only one reflection occurs. The taper angle is therefore dependent upon the maximum angle at which the light enters the light guide from the BCAL. The blue-green light traveling in the core of the fibre has a maximum angle from the axis of the fibre of $27.5°$ as dictated by total internal reflection between the first and second layers of cladding. Any light at larger angles is lost before it exits the fibre. The core of the scintillating fibre has an index of refraction of $n = 1.6$, therefore when the light is transmitted into the light-guide, which has an index of refraction of $n = 1.49$, any rays exiting the fibre at $27.5°$ are refracted to a higher angle in the acrylic of the light-guide. Because of this, the light-guide is designed for $\theta_{max} = 29.5°$.

From the edge-ray principle [125] the length of the cone can be calculated as

$$L = \frac{(a'' + a)}{tan\theta_{max}} \tag{4.8}$$

where $a'' = \sqrt{2}$ cm is the entrance radius of the cone and $a = 1$ cm is the exit radius.

Simulations of light transport through Section A of the light-guide with the geometry described above are possible within GEANT3 [95]. Calculations of the efficiency of a light-guide using Čerenkov light in the green wavelength with different angles of conical tapering were performed with the results shown in Fig. 4.18. The length of the light guide in the simulation was kept constant at 10 cm such that the portion that was not tapered was still square and attenuation effects due to path length

were minimized. The length of the portion that is tapered changes with the angle of tapering as seen in Eq. 4.8. The GEANT3 simulations were in agreement with the edge-ray principle. Fig. 4.18 shows that for longer tapered sections with shallower tapering, the efficiency is fairly flat, $\eta \simeq 0.96$ and but the efficiency drops off sharply at angles greater than 29.5°. In order to achieve maximum efficiency with minimal cone length and material, $\theta_{max} = 29.5°$ was chosen for the tapered section of the light guide. The surface of Segment A is described by Eq. 4.10 below.

Transmission vs theta(max)
(theta=0-29.5deg) (n=1.49) 2x2cm^2 to r=1cm with L(guide)=10cm
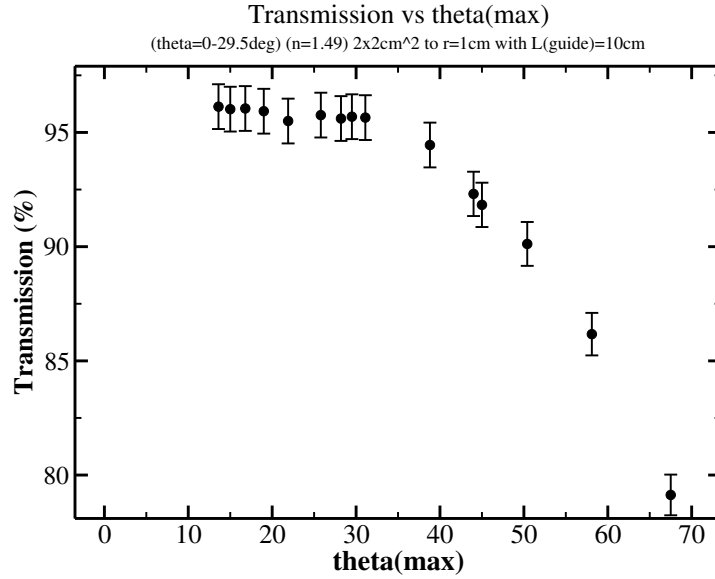
Figure 4.18: Efficiency results of the light-guide from a GEANT3 simulation with 2×2 cm^2 entrance and 1cm radius exit with a flat polar angle distribution of the photons between 0° and 29.5° with random azimuthal angle. The horizontal axis describes the tapering of the cone.

$$r(z) = a'' - z\frac{(a'' - a)}{(a'' + a)}tan(\theta_{max}) \tag{4.9}$$

where $0 \leq z \leq L_{cone}$. The length of the conically tapered section is $L_{cone} = 4.27$ cm

(from Eq. 4.8). Substituting the physical values into Eq. 4.9 we obtain (in cm):

$$r(z) = \sqrt{2} \text{ cm} - (0.097071) \cdot z \tag{4.10}$$

The origin for Eq. 4.9, $z = 0$, lies at the border between the tapered and untaperd portions.

The transmission efficiency as a function of discrete entrance θ is shown in Fig. 4.19. Some fraction of light is transmitted all the way up to $\theta = 42.5°$. Fig. 4.20 shows the intensity of light over the exit area of Segment A. Notice the increased intensity in the corners due to reflections from the tapered portions of the segment.

Light guide transmission curve
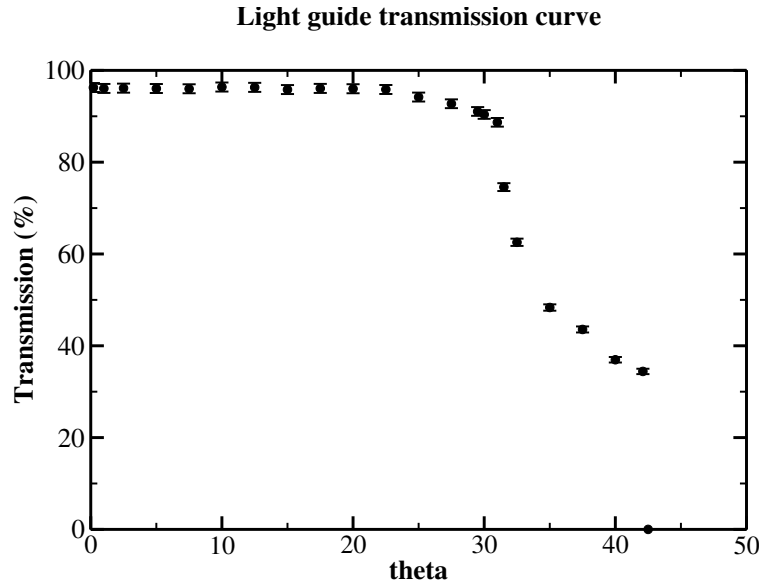
Figure 4.19: The transmission curve from Monte Carlo simulation for Segment A for discrete entrance θ (random azimuthal angle), distributed randomly in x and y over the entrance aperture.
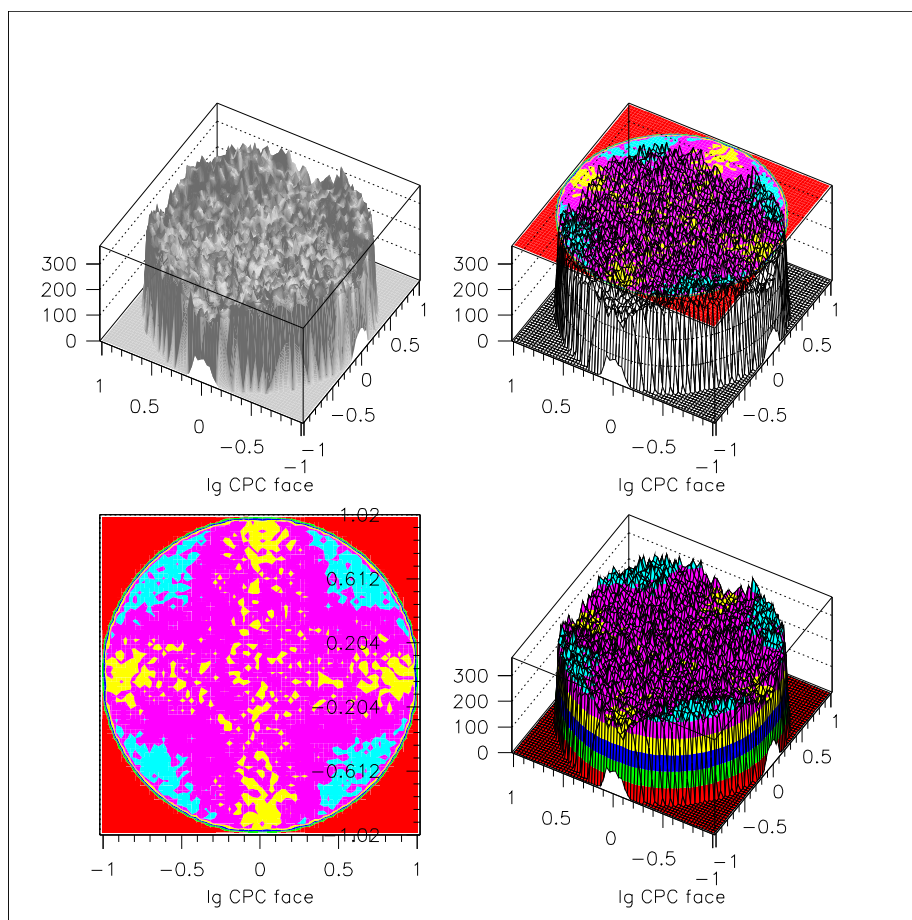
Figure 4.20: Surface plot of the 2-d histogram (x,y) of the intensity of light at the exit aperture from Monte Carlo data for the cone tapered section A. The four panels present different views/projections and constrasts for clarity. *(original in colour)*
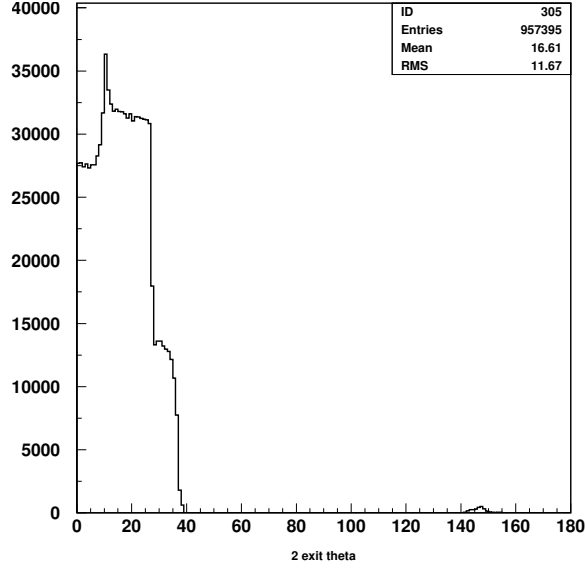
Figure 4.21: A histogram of the polar angle, θ, in degrees, at the exit aperture of the cone tapered section A. The vertical axis indicates the intensity of the light rays.

4.2.2.2 Segment B

This is the Winston Cone segment of the light guide. The properties of CPCs, or Winston Cones, are well known and have been shown to be nearly ideal due to their symmetrical properties [125]. Matching the entrance aperture of the CPC to the exit aperture of the tapered section, and choosing the exit aperture of the CPC, defines its other parameters.

WICO [95], a simple ray tracing program, was used to calculate the efficiency of the CPC for various exit areas. Data from the GEANT simulation that produced Figs. 4.20 and 4.21 were used as inputs to the WICO calculation. The transmission efficiency for CPCs with different exit apertures are shown in Fig. 4.22. The efficiency is quite good even at smaller areas but is largest when it reaches 1.2 cm^2 and plateaus for larger exit areas.

The exit aperture area, A, for the prototype light-guide has been chosen to match

Transmission curve for a=1.0 cm Winston Cone (CPC)

Entrance position and momenta from tapered light guide simulation
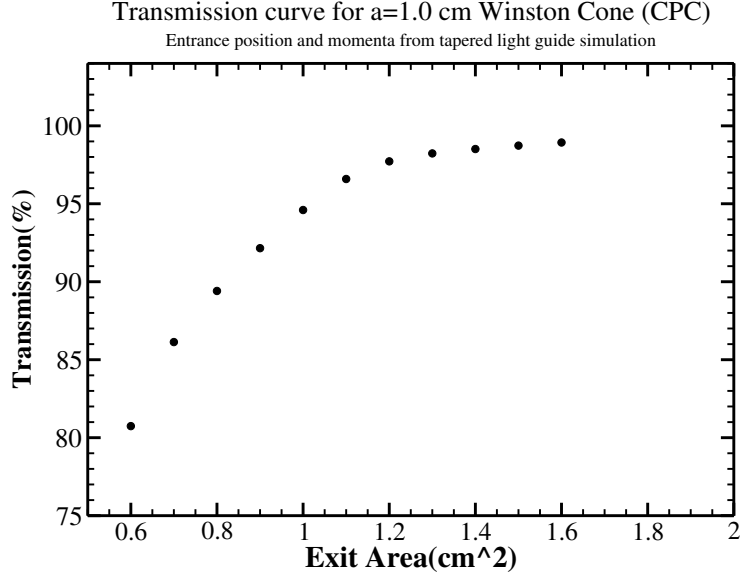
Figure 4.22: Transmission curve for CPC efficiency vs. exit area.

the active area of the SiPM ($A = 1.26$ cm^2). The entrance and exit apertures of the Winston cone dictate the other parameters of the CPC:

$$a' = \sqrt{\frac{A}{\pi}} = 0.633301 \text{ cm}$$

which gives

$$\theta_{max_B} = sin^{-1}(\frac{a'}{a}) = 39.3°.$$

From [125] we obtain the equations describing the surface of the CPC. (The origin for the following, $z_B = 0$, lies at the exit of Segment A):

$$r_B(\theta) = \frac{2a'(1 + sin\theta_{max_B})sin\theta}{1 - cos(\theta + \theta_{max_B})} - a' \tag{4.11}$$

$$z_B(\theta) = \frac{a'(1 + \frac{1}{sin\theta_{max_B}})}{tan\theta_{max_B}} - \frac{2a'(1 + sin\theta_{max_B})cos\theta}{1 - cos(\theta + \theta_{max_B})} \tag{4.12}$$

where $\theta_{max_B} \leq \theta \leq 90°$.

Eq. 4.12 yields a length for the Winston Cone of $L_{CPC} \simeq 2.00$ cm for the desired entrance and exit apertures stated above. A histogram of the polar angle for light leaving the CPC is shown in Fig. 4.23. The exit angle now extends to higher angles such that, if there is an air gap at the exit window, any light at angles higher than $42°$ (about $\sim 30\%$ of the total) will be total internally reflected back into the light-guide. Fig. 4.24 shows the light intensity over the surface of the exit aperture. The higher intensities near the edges of the exit aperture are due to the paraboloid focusing the light there. The pair of valleys are likely a feature of the tapering in Segment A.
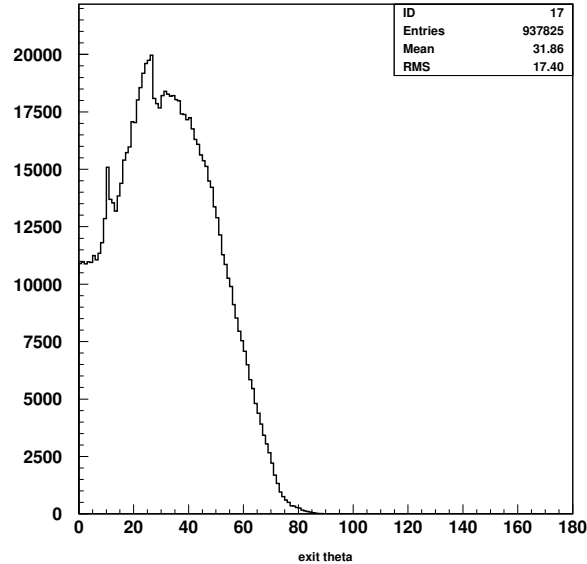
Figure 4.23: A histogram of the polar angle, θ, in degrees, at the exit aperture of the CPC (area = 1.26 cm^2). Notice the smearing to much higher theta compared to the exit of SegmentA (Fig. 4.21). The verticle axis is the intensity of light rays. An air gap will internally reflect light above $42.5°$.

4.3 Results and Final Design

By choosing optimal parameters for maximum efficiency for Segment A (based on Fig. 4.18) and Segment B (based on Fig. 4.22), a light-guide with an overall efficiency
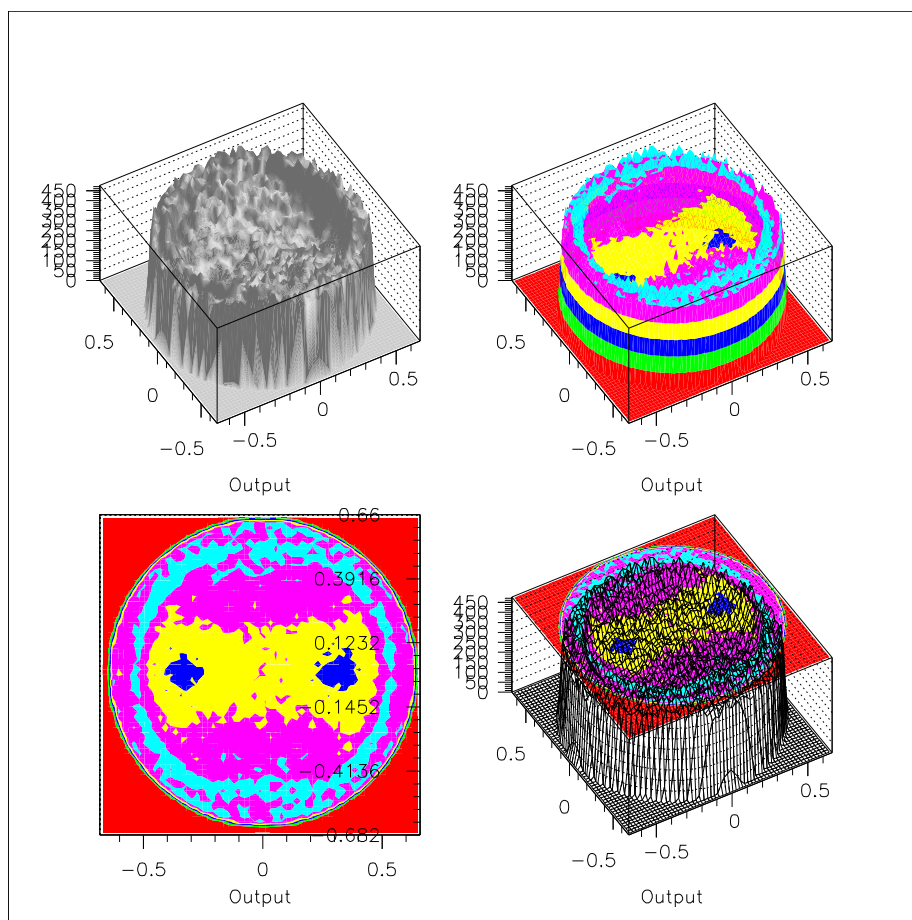
Figure 4.24: Surface plot of the 2-d histogram (x,y) of the intensity of light rays at the exit aperture of the CPC of area $= 1.26$ cm^2. The four panels present different views/projections and constrasts for clarity. *(original in colour)*

of approximately $\eta = 0.90$ (assuming no internal reflections at the exit) can be achieved. This is an optimistic value for the efficiency, however, since it does not include variations or losses due to coupling with the BCAL or photo-detector, or imperfections in the material's volume or surface. Equations [4.8–4.12] describe the surfaces and dimensions of a lightguide with this design and have been employed to manufacture 10 cm prototypes (3.5 cm untapered, 4.5 cm conically tapered and 2 cm CPC), which have been already used in cosmic-ray tests on the BCAL. One is shown in Fig. 4.25.
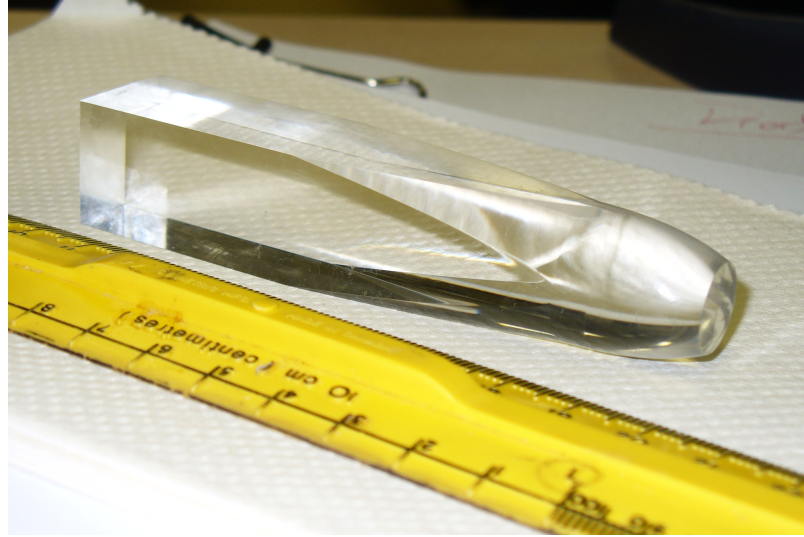
Figure 4.25: A photograph of a manufactured acrylic prototype of the lightguide. *(original in colour)*

Currently, other collabotors (Jefferson Lab, Univ. of Santa Maria (Chile)) have begun simulations of trapazoidal shapes, and will continue work on light guide development for the readout of the BCAL.

Chapter 5

The BCAL Jefferson Lab Hall B

Beam Test

The goals of the beam test were to measure the energy, timing and position resolutions of the prototype BCAL module, Prototype-1, as well as the response of the module at different positions along its length and at various angles of the incident beam. Results of this beam test will anchor further Monte Carlo simulations of the GlueX detector and will aid in the development of the 48 modules for the full BCAL detector. The detailed analysis and results reported in this thesis are for the Prototype-1 module perpendicular to the beam ($\theta = 90°$) with the beam incident at its centre ($z = 0$ cm).

5.1   Experimental Facility

The beam test took place in the downstream alcove of Hall B at the Thomas Jefferson National Accelerator Facility (Jefferson Lab). In order to accommodate the module with its support frame, readout system and cables, an additional platform

was installed in front of the beam-dump alcove. This expanded space allowed for the measurements with the photon beam perpendicular to the module, as well as providing a greater range of lateral and rotational degrees of freedom for the module when positioned inside the alcove. However, as illustrated in Fig. 5.1, the relative dimensions of the alcove and platform, with respect to the length of the module, still allowed for only a limited range of positions and incident angles that could be illuminated by the beam. Measurements, when the module was on the platform and oriented perpendicularly to the beam, were possible for relative positions of the beam spot between -100 cm to $+25$ cm with respect to the centre of the module. Within the alcove, the angular range was limited to angles $40°$ and less, and a length scan was carried out between -190 cm to -15 cm. The module was mounted on a cart that could be remotely rotated with good precision to the required angle. Lateral movements of the module with respect to the beam required a hall access for manual positioning.
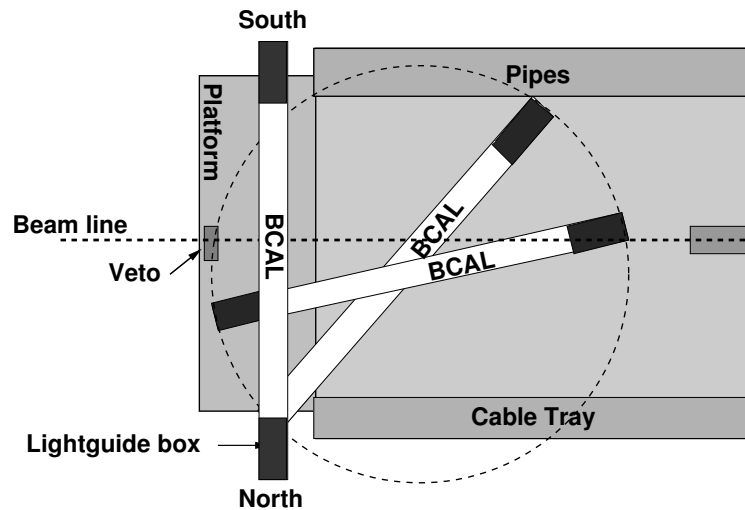
Figure 5.1: Diagram of the Hall-B downstream alcove with schematic placements of the BCAL module. The drawing is not to scale.

The primary electron beam energy from the CEBAF accelerator at Jefferson Lab

was $E_0 = 675$ MeV and the current was 1 nA for most of the measurements. The electron beam was incident on a thin target (the "radiator") located just upstream of the magnetic spectrometer (the "tagger"). The energies of the electrons scattered from the radiator were measured, thus providing timing and momentum information for the associated bremsstrahlung photons with a spectrum of energies from 150 MeV to 650 MeV, as described below. The photon beam was collimated with a 2.6 mm collimator, reducing the flux after collimation to 6.5% of its original value, resulting in a beam spot of virtually uniform density with a diameter of 1.9 cm on the BCAL module. The distance from the radiator to the collimator, and the collimator to the BCAL, were 5.8 m and $\sim$39 m, respectively. See Ref. [127] for more details on the Hall B tagger.

The Hall B tagger system determines the electron momentum information from 384 individual scintillator paddles, called E-counters, with a phototube on one end. Each of these counters is arranged to cover constant photon energy intervals of $0.003E_0$ and to physically overlap with its adjacent neighbour by 1/3 of its width, thus creating 767 individual photon energy bins and providing an energy resolution of $0.001E_0$. The timing information, on the other hand, is provided by 61 individual scintillator counters, called T-counters, with phototubes attached to both ends. The T-counters are classified in two groups. The first 19 (narrower) counters cover 75% to 90% of the incident electron energy range, and the remaining 42 counters cover the 20% to 75% range.

5.2 Prototype BCAL Module

The first prototype module (Prototype 1), was constructed of alternating layers of 99.98% pure lead of 0.5 mm thickness that were grooved ("swaged"), creating chan-

nels to accommodate the fibres. This was accomplished by passing the lead sheets between the two grooved rollers of a custom-designed machine thereby creating the channels by plastic deformation of the lead. The fibres were obtained from Pol-HiTech[1] and are of type PHT-0044 double-clad scintillating fibres of 1 mm diameter. The fibres were bonded in the lead channels with Bicron-600[2] optical epoxy. The thickness of the module is 23 cm, its length is 400 cm and the width is 12 cm, with the internal matrix geometry as indicated in Fig. 3.6. The matrix was built upon an aluminum base plate of 2.54 cm thickness that was further supported by a steel I-beam for added stiffness and ease of handling. Prototype 1 was not machined along its long sides at the 7.5° indicated in Fig. 3.3 and retained its rectangular profile from production. This is not expected to have an impact on the results of the beam test. However, the two ends of the module, where the read-out system was attached, were machined and polished. Visual inspection revealed that only eight of the approximately 17,000 fibres had been damaged in handling and construction. No optical defects affecting light transmission were observed in the other fibres.

5.3   Readout and Electronics

The module was divided into 18 readout segments, each with dimensions 3.81 × 3.81 cm^2. This segmentation comprised six rows in depth and three columns vertically with respect to the beam, as shown in Fig. 5.2. Acrylic light guides having a square profile and with a 45° mirrored surface channelled the light from the fibres to the PMTs that were placed perpendicularly to the fibre direction on both the North and South ends of the module, as shown in Fig. 5.3. The staggered, vertical placement

---

[1]PolHiTech SRL, 67061 Carsoli (AQ), Italy (www.polhitech.it).
[2]Saint-Gobain Crystals & Detectors, USA (www.bicron.com).

of the PMTs was due to their diameter of 5 cm being larger than the 3.81 cm width of the readout segment size. Large, rectangular silicone sheets, 2.5 mm thick, were used to interface the light guides with the module and smaller, circular, 2.5 mm thick, silicone cookies coupled the PMTs to the light guides. The readout ends and all their components were enclosed in an aluminum box painted black with the top covered by Tedlar®[3] PVF to maintain light-tightness. The shower profile was such that most of the energy, nearly 90%, was deposited in the first 12 cm of the BCAL and the largest number of photoelectrons originated in that part of the module. For this reason, the three upstream columns of Fig. 5.2 were read out using Philips[4] XP2020 photomultiplier tubes. These tubes were selected for their good timing characteristics. The last three rows were read out using Burle[4] 8575 PMTs.

The bases for the PMTs were designed with dual BNC outputs on the anode. The signals were sent to a CAEN[5] C207 equivalent leading edge discriminator and from there they were sent directly to a JLab F1 TDC [128] that was used to record the timing of the signals. The sum of the discriminator outputs was sent to a second discriminator, the threshold of which was set to require signals from at least four PMTs from each end of the module. The threshold logic pulse from either end (North OR South) of the module and the Master OR (MOR) signal from the T-counters of the tagger defined the trigger for the experiment. On average, the event rate was between 1 to 4 kHz for the duration of the beam test. A special electronics module was used to allow cosmic event triggers from scintillator paddles placed above and below the module as well as triggers from a pulser that were used to establish ADC pedestals, and were recorded concurrently with beam data. Signal amplitudes from the second BNC output of the PMTs were digitized using CAEN V792 ADCs.

---

[3]Tedlar® is a registered trademark of E. I. du Pont de Nemours and Company or its affiliates.
[4]PHOTONIS SAS, Brive, France (www.photonis.com)
[5]CAEN Technologies, Inc. Staten Island, NY, USA www.caen.it/nuclear/
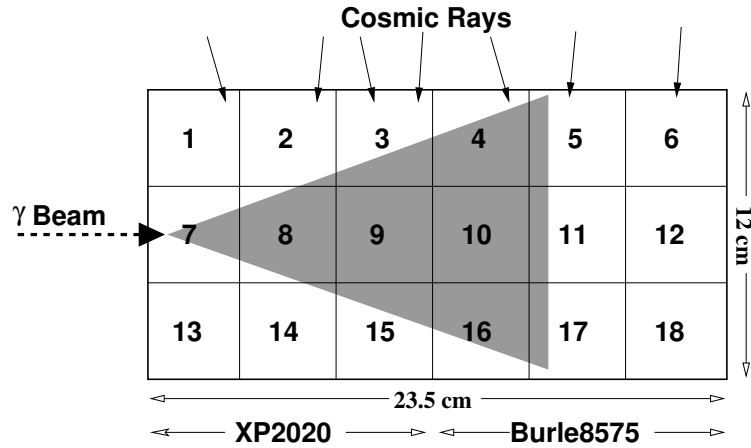
Figure 5.2: The segmentation and readout for the BCAL module as viewed from its North end. The lead/scintillating fibre matrix would appear to be rotated by 90° with respect to Fig. 3.6. The electromagnetic shower that develops in the module approximately forms a cone shape and is illustrated with the shaded triangle in the figure. A very small percentage of the energy is deposited in the outer segments or leaks out the sides.
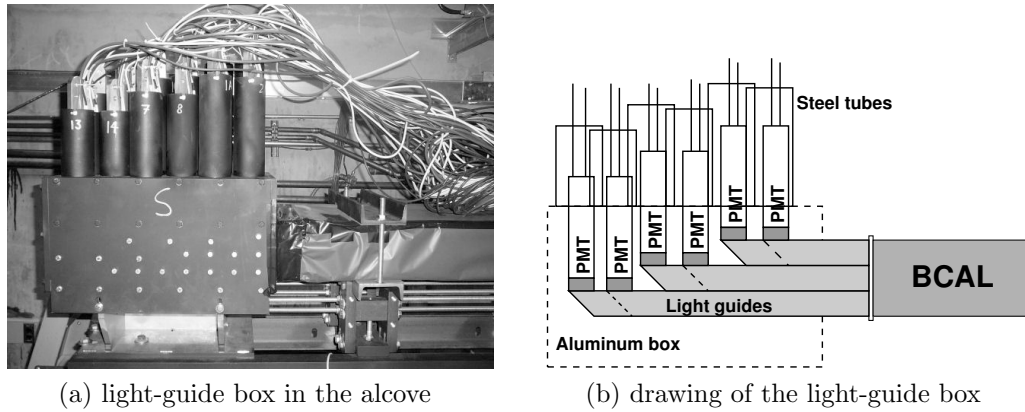
(a) light-guide box in the alcove   (b) drawing of the light-guide box

Figure 5.3: (a) The box that enclosed the 18 light guides and PMTs with cables attached for the South end of the BCAL module is shown. (b) The module was entirely wrapped in Tedlar® on the right and pressed against the light guides using a silicone sheet as an optical coupling, as described in the text.

The complete logic diagram is shown in Fig. 5.4.

5.4 Energy Resolution

5.4.1 Gain Balancing and Energy Calibration

With the module divided into 18 segments on each of the North and South sides, 36 PMTs were utilized in total. By adjusting the PMT supply voltage, an initial, relative balancing of the PMT gains was performed using cosmic data during the setup stage such that the means of the cosmic ADC spectra were nominally within ten percent of a certain value; only a couple of channels deviated from this value by up to a factor of two. Further adjustments to the gains were done in software during the analysis, using the spectra collected during four dedicated cosmic runs.

By assuming that the energy deposited by cosmic rays is uniform in each segment of the BCAL, a gain balancing constant was found for each North and South segment by taking the ratio of each segment's spectra to that of one particular segment,

$$C_{N,i} = \frac{N_{\text{ADC},i}}{N_{\text{ADC},7}}, \tag{5.1}$$

where $C_{N,i}$ was the balancing constant for the ith segment on the North side, each balanced with respect to $N_{\text{ADC},7}$. The procedure was identical for the South end, anchoring with respect to $S_{\text{ADC},7}$. Keeping in mind the attenuation length of the BCAL, $N_{\text{ADC},7}$ and $S_{\text{ADC},7}$ were then balanced with respect to one another. An overall energy calibration constant for the BCAL was then found by plotting the balanced ADC values versus the tagged photon energy.

Once the BCAL was calibrated, the distribution of the difference between the reconstructed BCAL energy and the tagged photon beam energy was found. This
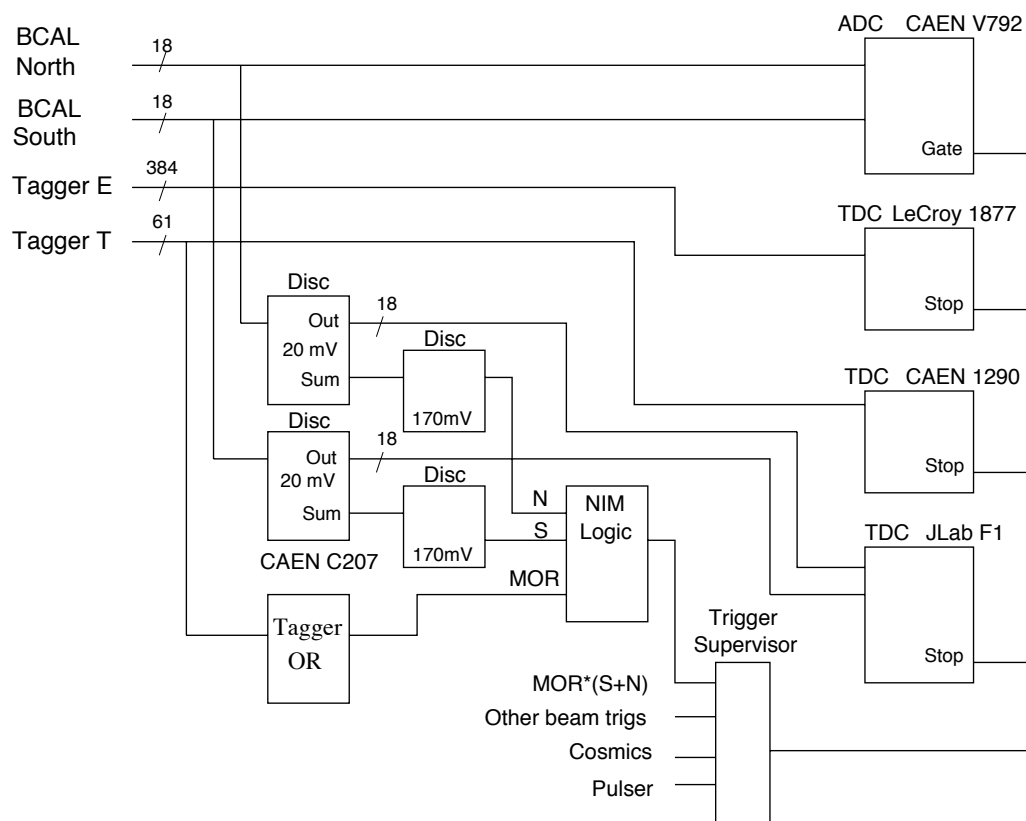
Figure 5.4: The logic diagram for the BCAL Hall-B beam test electronics. It should be noted that segments 1 and 13 did not contribute to the trigger, and this explains the apparent discrepancy between the 18 outputs of the discriminator and the sum output (that is just 16).

ratio, D, is defined as

$$D = \frac{E_{\text{BCAL}} - E_{\text{BEAM}}}{E_{\text{BEAM}}},$$ (5.2)

where E_{BCAL}, the reconstructed energy in the BCAL module, is defined as

$$E_{\text{BCAL}} = K \cdot \sqrt{\left(\sum_{i=1}^{18} \frac{N_{\text{ADC},i}}{C_{\text{N},i}}\right)\left(\sum_{i=1}^{18} \frac{S_{\text{ADC},i}}{C_{\text{S},i}}\right)}.$$ (5.3)

E_{BEAM} is the photon energy measured in the tagger and K is the overall calibration constant. The reconstructed energy in the BCAL module is then the geometric mean of the balanced ADC values multiplied by K. The geometric mean removes the effect of the attenuation in the fibres. The width of the distribution, σ_D, is the energy resolution, σ_E/E, for the module.
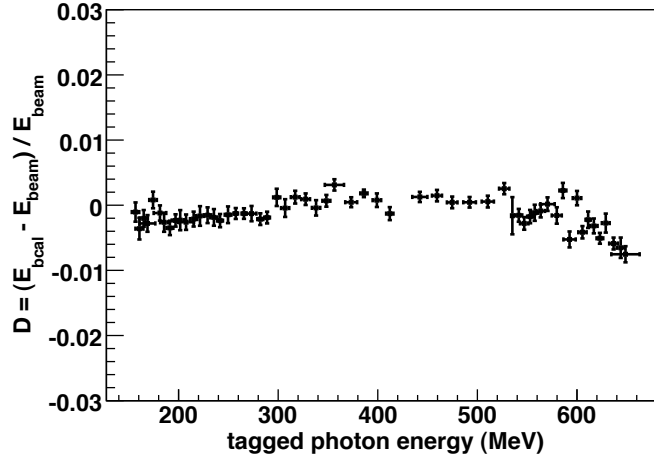
Figure 5.5: $D = (E_{\text{BCAL}} - E_{\text{BEAM}})/E_{\text{BEAM}}$ is shown after gain balancing and calibration. Notice that the deviations from zero are typically less than 0.5%.

A plot of D vs. E_{BEAM} can be seen in Fig. 5.5. This shows how well the PMT gains are balanced and how well the energy in the BCAL is reconstructed. Although the deviations from zero are so small as to be inconsequential, typically less than 0.5%, there may be a number of physical reasons for these deviations such

as non-linearities in the sampling fraction of the shower for each segment, albedo, background contributions to the ADC spectra which could not be removed at lower energies and leakage outside the module.

The deviation from zero below 300 MeV is most likely due to background that could not be removed from the ADC spectra. The deviation from zero above 575 MeV is probably due to electromagnetic shower leakage from the module and/or inherent nonlinearities in the detector due to the reduced sampling of the soft photons and electrons in the electromagnetic shower in the outer cells. All deviations from linearity, however, are small and typically less than 0.5%. Future beam tests will be carried out in more detail under production (physics running) conditions and are expected to yield a more accurate energy calibration and tighter distribution in D.

5.4.2 Energy Resolution Results

The calibrated spectra for D were fitted by a Gaussian function. A typical spectrum and its fit are shown in Fig. 5.6, this one for timing counter 40, corresponding to a beam energy of 273 MeV.

Subsequently, the energy resolution was extracted for all timing counters and is shown in Fig. 5.7, plotted as a function of the tagged photon beam energy, for the data at $\theta = 90°$ and $z=0$ cm. The fit to the data is also shown in Fig. 5.7, resulting in

$$\frac{\sigma_E}{E} = \frac{5.4\%}{\sqrt{E(\text{GeV})}} \oplus 2.3\%,\tag{5.4}$$

where the $\oplus$ indicates addition in quadrature. Small variations in the fits produced relatively large variations in the floor term $(2.3 \pm 1\%)$ but little variation in the stochastic term $(5.4 \pm 0.1\%)$.

The energy resolution of an electromagnetic calorimeter is typically expressed in
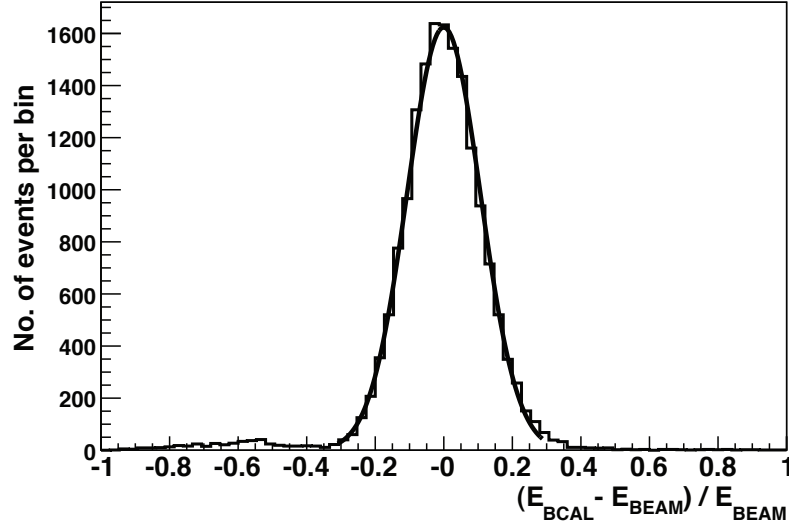
Figure 5.6: The calibrated spectrum for D is shown for timing counter 40, corresponding to a beam energy of 273 MeV. The solid line is a Gaussian fit to the data.

the form:

$$\frac{\sigma_E}{E} = \frac{a}{\sqrt{E(\text{GeV})}} \oplus b \oplus \frac{c}{E(\text{GeV})}. \tag{5.5}$$

The $a/\sqrt{E}$ term contains the combined effect of sampling fluctuations and photoelectron statistics. It is commonly referred to as the stochastic term. The $1/\sqrt{E}$ dependence is expected from the fact that the fluctuations are proportional to the number of particle tracks, n, that cross the active material; n has a Poisson distribution with a variance $\sqrt{n}$. Since the energy of a shower is proportional to n, the contributions to the resolution σ_E/E due to the stochastic fluctuations is proportional to $1/\sqrt{E}$. The KLOE collaboration concluded that the photon statistics from the light yield of their calorimeter ranges from $1.6\%/\sqrt{E(\text{GeV})}$ [129] up to $2.7\%/\sqrt{E(\text{GeV})}$ [130] and, therefore, contributes very little to the resolution since it is added in quadrature to the sampling contribution. Indeed, the stochastic fluctuations in sampling dominate the resolution.

The constant term, b, in Eq. 5.5, originates from all other energy-independent
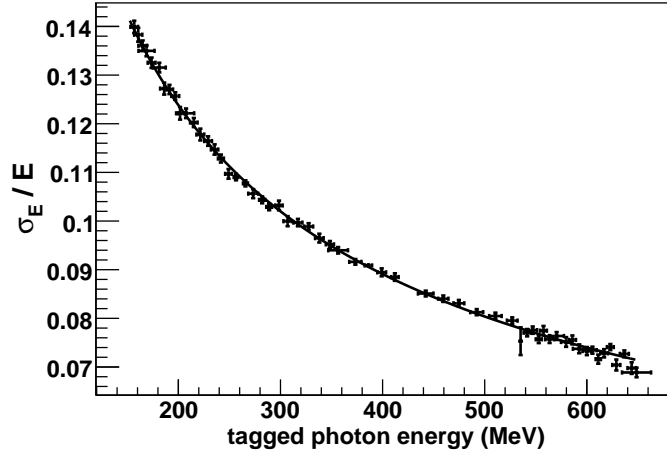
Figure 5.7: Energy resolution vs. E_{BEAM} for photons for $\theta = 90°$ and $z = 0$ cm. The fit gives $\sigma_E/E = 5.4\%/\sqrt{E(\text{GeV})} \oplus 2.3\%$. The fit of Fig. 5.6 corresponds to the 40th datum from the right (19th from the left) in this figure.

sources that contribute to uncertainties in the energy reconstruction. These sources can be mechanical imperfections, material defects, segment-to-segment calibration variations, non-uniformity of response, instability with time and shower leakage. Much work has gone into removing any of these effects during the construction of the BCAL module, throughout the beam test, and in any subsequent analysis.

If contributions from the noise term, c/E, existed, they would be from electronics noise and pileup in high-rate environments. This term increases at lower energies but has not been observed to contribute in the beam test analysis as both the rates and noise were low. Fits to the beam test data including this term produce almost identical stochastic and constant terms with values for c consistent with zero.

The stochastic coefficient, $a = 5.4\%$ in Eq. 5.4, compares well with the corresponding one from KLOE determined from $e^+e^- \rightarrow e^+e^-\gamma$ reconstruction, reported as $a = 5.4\%$ [93]. The KLOE beam tests [130] reported a value for $a = 5\%$. No value for b was reported in either case, as it did not contribute within KLOE's energy range

due to its addition in quadrature to the resolution. Uncertainties in these values have also not been published. The KLOE calorimeter and BCAL Prototype 1, as read out in the beam test, have similar sampling fractions and photostatistics. Although the production readout for the BCAL will be different, the beam test setup resulted in benchmark metrics for any future upgrades to the BCAL matrix structure, such as increasing the sampling fraction in the inner layers to improve low energy photon detection for critical regions of exotic hybrid production phase space and producing a better energy resolution.

As mentioned above, the stochastic fluctuations in sampling dominate the resolution. This being the case, there should be little effect on the energy resolution due to the shower position along the module (z). Attenuation of the light in the fibres will only affect the number of photoelectrons seen at the read-out ends of the module and is compensated for by the double ended read-out of the module. On the other hand, increasing the photon beam energy results in more particle tracks over a greater depth of the shower profile generated within the module, therefore more fibre layers are intercepted by more particle tracks. The expectation, then, is that the resolution will improve with increasing photon energy but remain nearly independent of the position of the beam spot. This was verified by examining the energy resolution for photon energies from 225 MeV to 575 MeV for three z-positions at normal incidence.

Finally, the value for the constant term in Eq. 5.4 was found to be, $b = 2.3\%$. This is the intrinsic constant value for the energy resolution of the BCAL. This value is march larger than the value found in KLOE, which reported a value near zero. However, the maximum energy of the BCAL photon beam test was too low to determine it precisely, as the uncertainty was estimated to be relatively quite large,

$\pm 1\%$. This uncertainty was estimated based on experience from attempts to fit the data. For low energies, the constant term contributes negligibly to the resolution at a few hundred MeV when added in quadrature to the stochastic term. Nevertheless, since approximately 30% of the photons in GLUEX will have energies above 500 MeV, efforts to minimize the constant term and extract it more accurately in future beam tests will be fruitful.

5.4.3   Sampling Fraction and Energy

The sampling fraction – the fraction of energy deposited in the SciFi's – can be expressed as a ratio with respect to either the total energy deposited in the BCAL module (f) or the incident photon energy (f_γ). These quantities, however, are difficult to measure in an experiment but fairly simple to simulate. A GEANT 3.21 simulation was developed to that end, based on modelling the BCAL as a standalone package and independent from the previously mentioned simulations. Individual fibre and epoxy volumes were programmed into the Monte Carlo with the appropriate Pb:SciFi:Glue ratios and material properties resulting in the geometry shown in Fig. 3.6.

These simulations indicate that f_γ decreases as a function of photon energy due to leakage. This is shown in Fig. 5.8a, with the decrease being linear above 200 MeV. It should be noted that the size of the module will primarily affect only f_γ in the sense that a smaller module will result in a smaller f_γ due to energy from the electromagnetic shower leaking outside the module. On the other hand, f depends only on the energy deposited in the matrix itself and is independent of the incident photon energy or overall geometry of the module. The deviation from linearity at low energy is probably due to the fact that more of the low energy electrons and positrons from
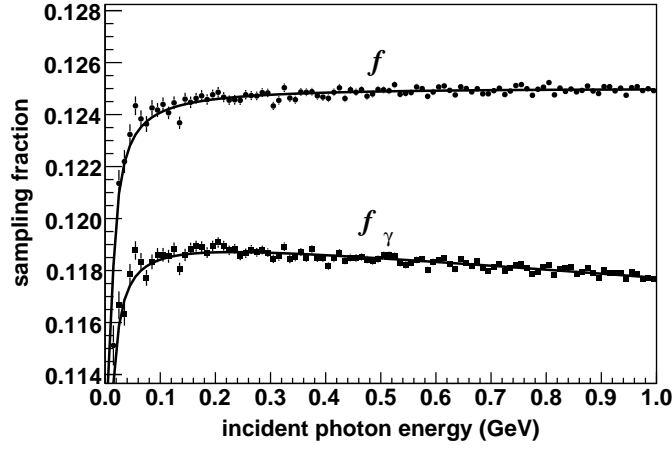
(a)
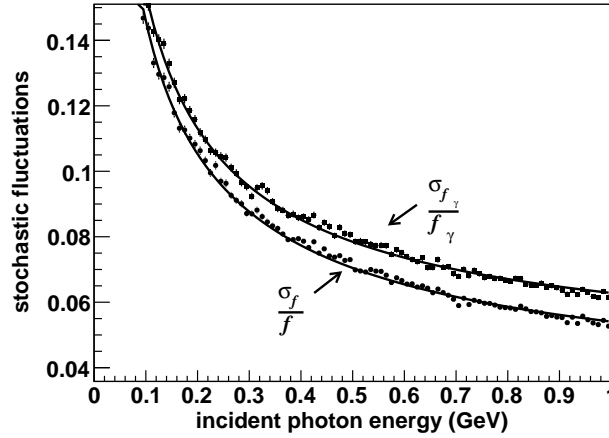
(b)

Figure 5.8: (a) The photon energy sampling fraction, f_γ, and deposited energy sampling fraction, f, are shown from simulation for $\theta = 90°$. The data are fit to $a_0/E + a_1 E + a_2$ functions, which were chosen among the simplest functions that described the data well. (b) The sampling fluctuations of the module, $\sigma_{f_\gamma}/f_\gamma$ and σ_f/f are plotted from simulation. The data are fit to $a/\sqrt{E} \oplus b$ functions with $a_{f_\gamma} = 4.6\%$, $b_{f_\gamma} = 1.6\%$, $a_f = 4.5\%$ and $b_f = 0.9\%$.

the electromagnetic shower stop in the lead before being sampled by the scintillating fibres. One would expect this reduction in both sampling fractions and this is what was observed.

The sampling fluctuations, σ_f/f, can be seen in Fig. 5.8b. These are the dominant contributor to the energy resolution, at about $4.5\%/\sqrt{E(\text{GeV})}$. Subtracting the simulated sampling fluctuation contributions from the measured energy resolution yields photoelectron statistics contribution to the energy resolution of about $3.1\%/\sqrt{E(\text{GeV})}$. This is similar to the estimated value of $\sim 2.7\%/\sqrt{E(\text{GeV})}$ from a KLOE beam test [130].

5.5 Timing and Position Resolution

The time difference of the signal from the BCAL ends will provide position information for neutral particles, which is needed to reconstruct their four-momenta. The position resolution is related to the time difference resolution by the effective speed of light within the calorimeter. Thus, by using measurements of the effective speed of light from a previous beam test at TRIUMF [101] ($c_{\text{eff}} = (16.2 \pm 0.4)$ cm/ns from Table 3.2), the position resolution of the calorimeter can be easily extracted.

The time difference resolution will be of the form:

$$\sigma_{\Delta T/2} = \frac{c}{\sqrt{E(\text{GeV})}} \oplus d. \tag{5.6}$$

In general, the constant term, d, in Eq. 5.6 is a result of residual calorimeter miscalibrations, but some fraction is also due to the finite width in z of the beam, which will contribute to the time difference resolution. With the beam width being $l \sim$ 1.9 cm, the flat and square distribution of the beam contributes $(l/c_{\text{eff}})/\sqrt{12} = 30$ ps

to the resolution.
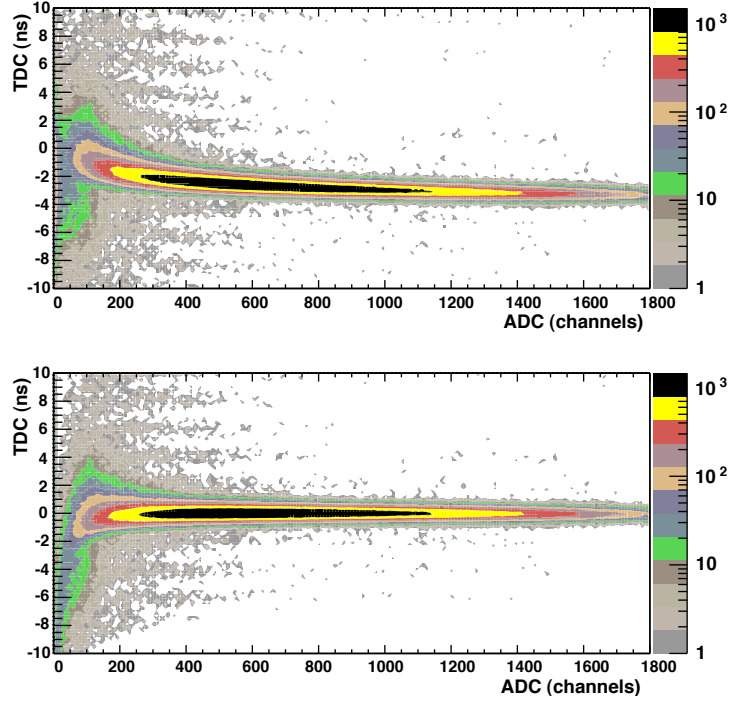
Figure 5.9: ADC vs. TDC for segment South 8. The uncorrected time affected by the time walk due to the dependence on amplitude is seen in the top plot. The bottom plot shows the corrected time. The BCAL time was referenced with the tagger time. *(original in colour)*

The double-ended readout of the BCAL allowed for time difference measurements to be made, but because leading edge discriminators were used, the timing of the discriminator signal output had a dependence on pulse height which required a time-walk correction. A plot of ADC versus TDC for segment 8 can be seen in Fig. 5.9. Fits with a function of the form $p_0/\sqrt{\text{ADC}} + p_1$ were performed, as the time delay due to signal amplitude in leading edge discriminators follows this form. The fit parameter p_1 is a constant term indicating the timing offset of the particular readout segment from the tagger MOR timing signal. Parameter p_0 also varies depending on the particular readout segment but has a nominal value of ~ 35 ns $\cdot$ GeV$^{1/2}$. The

fit is poor for the downstream segments, specifically segments 6 and 18 where the statistics are low, as there is very little energy deposited there and the fluctuations are consequently large. For this reason, most of the outer segments were not included in the timing analysis. Analysis of the timing data focused mainly on segments 7, 8, 9 and 10 where nearly 90% of the energy was deposited. Due to the resulting asymmetry from the walk correction at low ADC values, which caused distortions in the time difference resolution, low ADC values were rejected. In the case of South 8, channels lower than 350 were rejected. This corresponds to 1 MeV of energy deposited in the segment or 0.125 MeV deposited in the fibres. Similar ADC cuts were made for the other segments depending on the distortion at the lower end of the ADC spectra. This results in a loss of efficiency, and slight bias for events which fluctuate to a higher signal, at the lower energies but in a much improved time difference resolution over the whole tagger spectrum.

The timing for an event was found by summing the TDC values of all the segments in an event cluster, weighted by their energy; cuts on the ADC and timing determined whether a segment was included in the cluster. A cluster is defined by the energy weighted sum of the times of each segment such that the time difference, ΔT, is expressed as:

$$\frac{\Delta T}{2} = \frac{1}{2} \frac{\sum_i E_i (T_{\mathrm{N},i} - T_{\mathrm{S},i})}{\sum_i E_i} \tag{5.7}$$

Subsequently, the walk-corrected spectra for each tagger timing counter were fitted by a Gaussian function. A typical spectrum and fit are shown in Fig. 5.10, this one for timing counter 40. All timing counter spectra were fitted in the same fashion, and the fit results are plotted on Fig. 5.11. From the subsequent fit in that figure, the time difference resolution including only the middle row segments 7, 8, 9
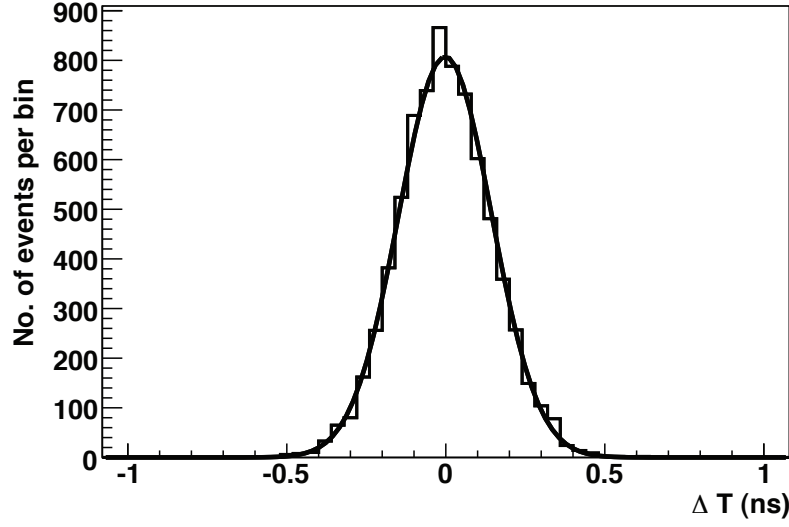
Figure 5.10: The walk-corrected spectrum and Gaussian fit for timing counter 40. The solid line is a Gaussian fit to the data.

and 10 is found to be:

$$\sigma_{\Delta T/2, 7-10} = \frac{75 \text{ ps}}{\sqrt{E(\text{GeV})}} \oplus 30 \text{ ps}. \tag{5.8}$$

The floor term is equal to the finite width of the beam, as expected. This implies that the intrinsic time resolution of the BCAL is consistent with zero for the constant term. As the time difference resolution is dependent on the number of photoelectrons, the time difference resolution, $\sigma_{\Delta T/2, 7-10}$, can be corrected to include the missing photoelectrons, after subtracting the beam width from the constant term, and is found to be

$$\sigma_{\Delta T/2} = \frac{70 \text{ ps}}{\sqrt{E(\text{GeV})}}. \tag{5.9}$$

The KLOE beam test result of 72 ps/$\sqrt{E(\text{GeV})}$ [130] represents the timing resolution extracted from the signal average of both ends of each segment. With better fibres and PMT's KLOE estimated they could achieve a resolution of $\sim$
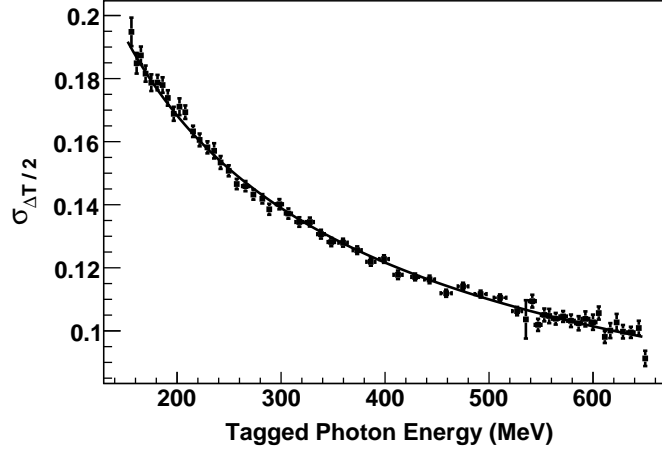
Figure 5.11: The time difference resolution, in nanoseconds, for segments 7, 8, 9 and 10 as a function of energy. The fit gives $\sigma_{\Delta T/2} = 75$ ps$/\sqrt{E(\text{GeV})} \oplus 30$ ps. The fit of Fig. 5.10 corresponds to the 40th datum from the right (19th from the left) in this figure.

58ps$/\sqrt{E(\text{GeV})}$ and this was achieved [93]. The result shown here from the BCAL beam test was extracted from the time difference of the signals. It should be noted that old/degraded PMTs were used in this beam test, especially the 18 Burle 8575's used in the three rear layers of the module, which had a timing resolution per pair averaging around 1.4 ns in contrast to the forward XP2020's that averaged around 0.6 ns per pair. As such, it is expected that the time difference resolution from Prototype 1 is actually better than reported here and the use of better fibres, light guides and light sensors will result in an improved timing resolution.

Finally, the time difference resolution defines the position (z) resolution along the length of the module, since $\sigma_z = \sigma_{\Delta T/2} \cdot c_{\text{eff}}$. Therefore, the determined position resolution is calculated to be $\sigma_z = 1.1$ cm$/\sqrt{E(\text{GeV})}$ for a 1 GeV photon. KLOE reported a similar position resolution from their beam test of $\sigma_z = 1.2$ cm$/\sqrt{E(\text{GeV})}$ [130].

5.6   Determination of the number of photoelectrons

The number of photoelectrons per end of the prototype BCAL module, N_{pe}, was estimated at $z = 0$ cm and $\theta = 90°$. The distribution in the ratio, R, of the North to the South readout sums, for each of ten bins in beam energy, E_j, from 150 MeV to 650 MeV, was expressed as

$$R(E_j) = \frac{\sum_{i=1}^{18} E_{N,i;j}}{\sum_{i=1}^{18} E_{S,i;j}} \qquad (5.10)$$

where $E_{N,i}$ and $E_{S,i}$ are the calibrated energies corresponding to the ith segment on the North and South side, respectively. Using this ratio results in the suppression of shower fluctuations that dominate the statistical variance of the individual sums for each readout end. Under the assumption that each of the amplitude spectra has a Poisson-type shape, the ratio spectra were fitted to the function:

$$f(r) \sim \int P(x, N_{pe} \cdot \sqrt{R}) \cdot \frac{1}{r} P\left(\frac{x}{r}, \frac{N_{pe}}{\sqrt{R}}\right) \left[\frac{x}{r}dx\right] \qquad (5.11)$$

where r is a North/South amplitude ratio, R is an average North/South amplitude ratio, N_{pe} is the average number of photoelectrons, and P is a Poisson-type probability:

$$P(x, N) = \frac{e^{-N}N^x}{\Gamma(x+1)}. \qquad (5.12)$$

The $(1/r)$ and (x/r) factors are needed to perform the integration over the uniform r-bins. The χ^2/ndf was nearly one for all the fits. The resulting photoelectron yield per GeV per end is plotted in Fig. 5.12 as a function of beam energy.

The one parameter fit in Fig. 5.12 yields a mean value of $\sim$660 photoelectrons
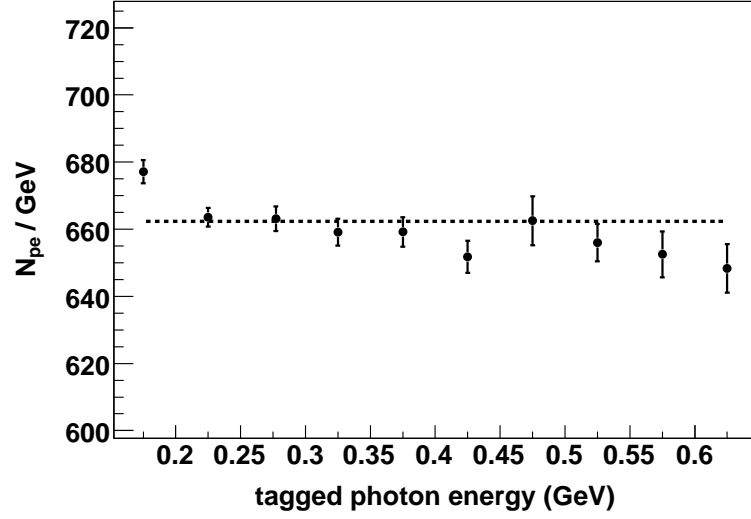
Figure 5.12: The number of photoelectrons per GeV per end of the BCAL module is shown as a function of energy. A one parameter fit is plotted (dashed line). For more details see the text.

per GeV for photons over the energy range of the beam test. A non-linearity of $\sim5\%$ is apparent, but not worriesome, due to the preliminary nature of the beam test. A similar effect can be seen in results from KLOE beam tests for photons and positrons [129]. The non-linearity in the number of photoelectrons observed may be due to the non-linearity of the detector when sampling the soft photons of an electromagnetic shower, variations in the light guides and their couplings and shower leakage. Nevertheless, this is an adequate estimation of the number of photoelectrons from this work and future beam tests over a wider range of energies with a more sophisticated readout system similar to the final experiment will solidify this value and more thoroughly reveal any non-linearities in the detector response.

In comparison, KLOE reported $N_{pe} \sim 700$ per end at 1 GeV. The BCAL module used double-clad scintillating fibres, potentially giving rise to approximately 50% more photoelectrons than KLOE. However, the KLOE calorimeter had light guides combined with Winston Cone collectors that resulted in a much higher transport

efficiency, typically ∼90%, than the light guides used in the beam tests described in this work, estimated to have a transport efficiency of ∼50%. This feature could easily compensate for the increased capture ratio of the fibres in the BCAL, but lower number of measured photoelectrons.

5.7 Prototype-1 Performance

The first full-scale prototype module for the BCAL tested the construction techniques and the performance of the matrix under beam conditions. An energy resolution of $\sigma_E/E = 5.4\%/\sqrt{E(\text{GeV})} \oplus 2.3\%$ and a time difference resolution of $\sigma_{\Delta T/2} = 70$ ps$/\sqrt{E(\text{GeV})}$ ps were found from the Jefferson Lab beam test data. The number of photoelectrons per GeV is about 660. The energy and timing resolutions meet the original design goals and the performance of the module closely matches that of KLOE, a proven sampling calorimeter. The analysis for the more demanding regions of module and beam geometries, near the end of the module and at small incident angles can now proceed having established the performance under more benign conditions and having the Monte Carlo simulations tested and anchored to the data.

Chapter 6

Hall D Monte Carlo Detector Simulation

The development of an accurate and realistic Monte Carlo simulation is key in the development of any particle physics detector. Simulation of the full detector allows for informed decisions about detector design before construction and, once experimental data have been taken, the simulation aids in the interpretation of the results. In the case of the GLUEX BCAL, which was modeled on KLOE calorimeter, the simulations allowed for confirmation of certain calorimetry properties and for the differences between the KLOE calorimeter and the GLUEX barrel calorimeter to be investigated. Additionaly, with a full simulation of the detector, reconstruction algorithms can be developed and analysis of simulation data can be performed such that the detector's acceptance and extracted mass resolutions can be calculated before any experimental data are taken.

6.1 Overview

A complete series of simulation and reconstruction software packages have been developed and implemented for neutral particle detection in GLUEX, while tracking for charged particles and full event fitting is still in development. The object-oriented software, written by the collaboration in C^{++} and designed to be general and modular, is intended for experiment-wide use. Some custom reconstruction and analysis code was written specifically for this thesis work but was not made available to the whole collaboration due to its specific nature. Similar reconstruction code of a more general nature is planned to be added to the software repository in the future.

A schematic diagram of the data flow for the full calorimeter simulation and reconstruction framework is shown in Fig. 6.1. The simulation begins with the output from a Monte-Carlo (MC) physics generator with three different generators in the Hall-D software repository: a) the modified PYTHIA package tuned to GLUEX energies, discussed previously in Chapter 3, for producing hadronic background events, b) GENR8, a simple generator that produces single particles with fixed trajectories and c) AMPTOOLS, a generator that produces multi-body decays with appropriate spin-dependant angular distributions. Generated particles are propagated through a full GEANT3-based hit-level detector simulation, HDGEANT, that includes all active (detectors) and inactive (supports and cables) material in the tagger, collimator, target and GLUEX spectrometer. The detector desciption is written in XML for standardization. The initial particle vertex is dependent upon the generator and any initial conditions provided to the simulation. Additional digitization and response effects are incorporated in reconstruction algorithms outside HDGEANT to produce equivalent raw detector hits. Clusterization algorithms reconstruct the "hits" into "photon" objects. A hit is the position and energy information for a particular seg-

ment of the detector. As charged particles with higher momenta will deposit energy in several segments, thus mimicking a neutral particle as they are clustered regardless of the incident particle charge. Charged particle tracking information is used to differentiate these charged particle induced clusters from neutral particle showers. Kinematic fitting algorithms form pairs of photons into decays from mesons such as the $\pi^0, \eta, \rho^0, \omega^0$ which can be reconstructed to form further resonances and the entire physics event.

6.2 BCAL Simulation and Reconstruction

Electromagnetic shower development in the BCAL is simulated by tracking secondary particles through its volume and accumulating the deposited energy via ionization[1]. The geometries and materials are normally entered as parameters to the MC but in the case of the BCAL it is computationally too expensive to include the true geometry in the full GEANT-based detector MC. In the case of the HDGEANT software, a BCAL module was defined with an effective mixed material based on the volume, mass and atomic number ratios of the lead, glue and scintillating fiber. However, a stand-alone GEANT3-based simulation (SAMC) was created with the full fibre, lead and glue geometry to study the response of the full lead/sci-fi matrix. Information obtained from the SAMC is used in the HDGEANT to mimic the true response of the BCAL and was used to further understand the response of the prototype modules in the JLab beam test and cosmic ray tests. Some of this SAMC work has been presented earlier in this thesis, in Section 5.7.

---

[1]The secondary particles above 1 GeV generally lose their energy via bremsstralung (electrons) and pair-production (photons). The succesively lower energy electrons (below 1 GeV) in the electromagnetic cascade will increasingly start to lose their energy through ionization and thermal excitation; below a few MeV, photons will instead lose their energy through Compton scattering and the photoelectric effect.

Monte Carlo   **Experiment**

Event Generator   Trigger

GEANT (HDDM)   Detector

MCHit:FCAL, BCAL   ADC, TDC

MCResponse:
FCAL, BCAL

Hit: FCAL, BCAL

BCAL Shower   FCAL Shower

BCAL Photon   FCAL Photon

DPhoton   Charged Tracking

Kinematic Fit

Two–photon fit

PID and Global Fit
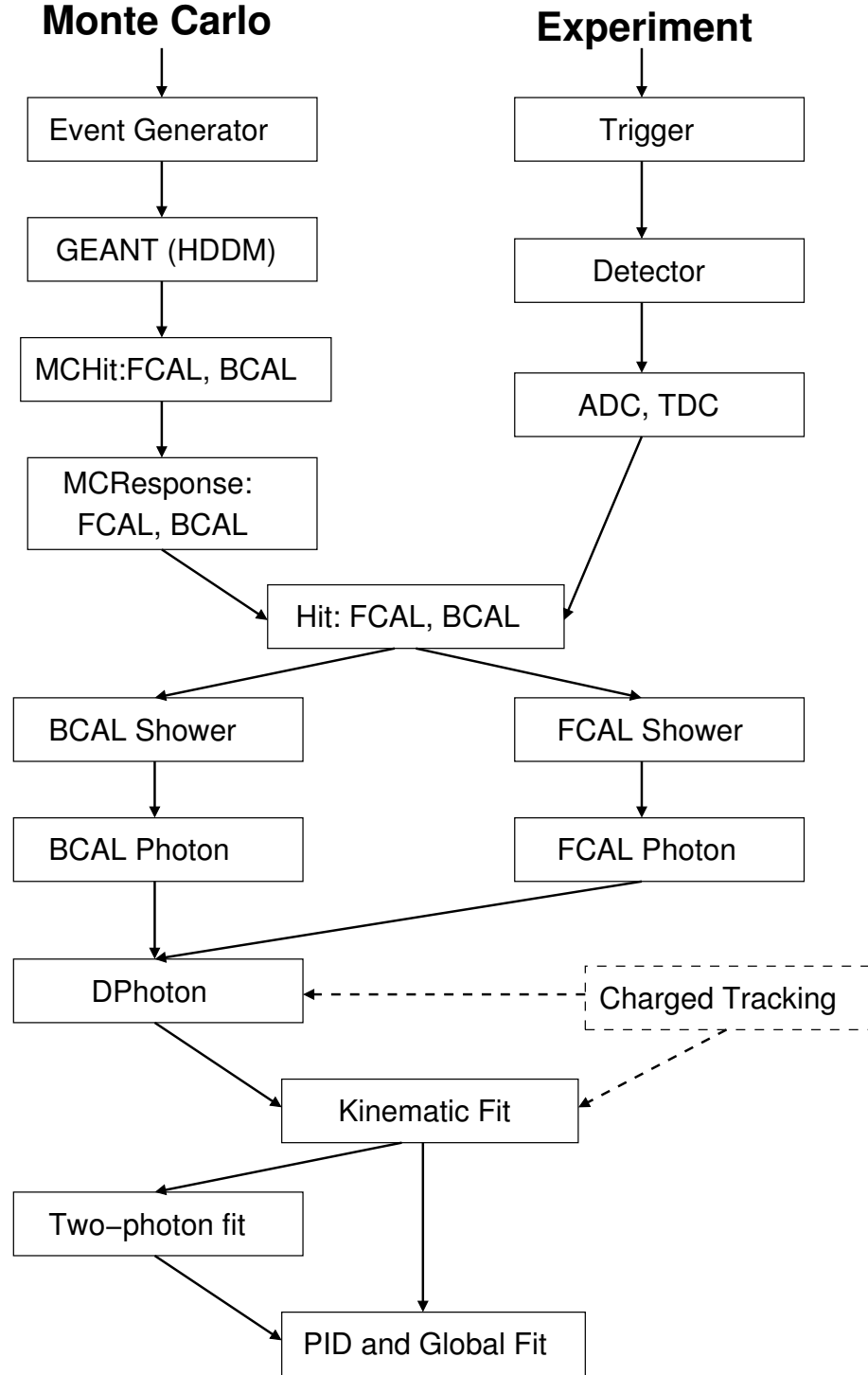
Figure 6.1: Data flow diagram for the GLUEX calorimeters from Monte Carlo and experiment. The dashed lines indicate input of data from the charged particle tracking software.

The response of each segment in the HDGEANT BCAL is simulated by multiplying the mean sampling fraction by the total energy deposited in the segment. Stochastic fluctuations are modelled by smearing the signal in each cell by a Gaussian distribution with a width that is a fraction of the mean sampling fraction, σ_f/f. The SAMC sampling fluctuation is explained further below. Light attenuation and time delay are modelled by using an effective attenuation length $\lambda = 350$ cm and speed of light in the fibre c' = 16.75 cm/ns that were measured in past cosmic ray tests of BCAL Prototype 1.

6.2.1 Sampling Fraction from the Stand-Alone Monte Carlo

The relatively low atomic number and density of the scintillator compared to the surrounding lead means that the active material in the BCAL will only sample approximately 12% of the energy deposited in a module. However, because only about half of the volume of the BCAL is filled with scintillator in a regular matrix of fibres, the number of fibres encountered by secondary shower particles fluctuates and therefore the sampled energy fluctuates. This stochastic fluctuation is the dominant contributor to the energy resolution of the BCAL and cannot be modelled in a mixed material module and therefore needed to be modelled in a stand-alone Monte Carlo where computational resources could be dedicated to simulating the response of a BCAL module with an internal matrix geometry. The sampling fractions and stochastic fluctuations from simulation were shown previously in Figs. 5.8a and 5.8b. As such, the sampling fraction fluctuations depend on energy in a cell as

$$\frac{\sigma_f}{f} = \frac{A}{\sqrt{E_{\text{dep}}}} \oplus B, \tag{6.1}$$

with A and B being 4.5% and 0.9% respectively.

6.2.2 Electronics Threshold

Electronics thresholds and dark noise in the readout SiPMs are also modelled in HDGEANT. Correctly modelling this is very important, as the threshold greatly affects the performance of the BCAL for energies less than 200 MeV. Some assumptions were made [131] in approximating the threshold: (1) zero suppression will be done on a per channel basis on the FADC so that the pedestal alone cannot cause more than 5% of all BCAL channels to exceed the zero suppression threshold. (2) The main contributor to the ADC pedestal is single photoelectron (PE) dark pulses from the SiPM, their rate being 40 MHz [132]. (3) The readout window for the flash ADC [133] is 100 ns. This means that the SiPM pulses must be fully contained in this window including any forward and backward shifts due to differences in transit time in the readout chain and transit time in the module (about 25 ns for full length). If the readout window is 100 ns, there will be an average of four single dark-rate PE pulses in each window. According to Poisson statistics, this means that 95% of events will have seven or fewer of these pulses. Therefore, the threshold for a cell to be accepted in the full HDGEANT simulation is set at eight photoelectrons.

Since the Monte Carlo simulation only calculates the energy deposited in a cell and not the number of photoelectrons, the average number of PE per MeV must be determined from experiment. This number is difficult to determine without a beam test using the final readout design and employing proper light-guides and SiPM sensors. The JLab beam test in 2006 used a coarser readout with bialkali PMTs and long, rectangular light guides with poor efficiency and thus were not well suited for the extraction of number of photoelectrons.

Cosmic ray tests [134], using the prototype light guides (designed in Section 4.2) and prototype SiPMs from SensL, measured an effective energy deposited in the fibre to photoelectron conversion of 91 keV/PE. The sampling fraction for cosmic rays is about 15%, therefore 1 PE = 91 keV / 0.15 = 0.61 MeV deposited in the module. As a result, after attenuation of the light in the module is accounted for, only hits with 8 PE × 0.61 MeV = 4.9 MeV deposited in the cell are recorded in the simulation, as these hits exceed the zero suppression threshold. Noise in the electronics has been neglected in this estimate, so the 4.9 MeV energy threshold per BCAL cell may be somewhat optimistic, but ongoing improvements in the SiPM array may reduce the dark noise rates. Some optimization in the FADC may lower the threshold too. However, the intent of the threshold estimate was to get as close as reasonably possible to the final, realistic value of the GLUEX experiment.

6.2.3 Clusterisation

In the reconstruction, the full collection of cells associated with a particle is called a "cluster". The energy and angular direction of a particle is obtained from the cluster information with no consideration for the details of the energy deposition or the shower profile. The original versions of the GLUEX BCAL reconstruction code were modelled after the KLOE reconstruction software [135]. The reconstruction code has been improved since, mostly to increase speed, but the basic data flow remains the same and functions as follows. First, the raw hits are read and arranged into arrays with the indices defined by the module, layer and sector number[2]. Since there are inner and outer sector layouts for the BCAL, columns are not a good index. Adjacent cells are then determined from the indices in the r and ϕ directions. By searching all

---

[2]The module index is defined by its position as one of the 48 modules of the barrel. The layer index increases in radius and the sector index is defined by its position in ϕ.

adjacent cells, a cluster can be constructed. If multiple clusters are found, clusters separated by less than 40 cm in space, 30 cm along z and 2.5 ns in time are merged into one cluster. Clusters are split in the z-direction if their time RMS is greater than 5.0 ns. After the clusters are merged or split the final energy and energy-weighted positions for the showers are determined as follows:

$$E_{shower} = \sum_{1 \leq i \leq n_{cell}} E_i \tag{6.2}$$

$$X_{shower} = \sum_{1 \leq i \leq n_{cell}} (X_i E_i)/E \tag{6.3}$$

$$Y_{shower} = \sum_{1 \leq i \leq n_{cell}} (Y_i E_i)/E \tag{6.4}$$

$$Z_{shower} = \sum_{1 \leq i \leq n_{cell}} (Z_i E_i)/E \tag{6.5}$$

To avoid the creation of spurious clusters due to isolated low energy cells in the calorimeter, all showers with energy less than 20 MeV are removed and not recorded. This threshold is being studied by others to determine its effect on shower reconstruction. If the threshold is too low, many clusters from back-scatter may be formed and cannot be associated with a particle trajectory. If the threshold is too high, the resolution degrades.

In addition to the energy-weighted position of the entire shower, the energy-weighted position *by layer* for each cluster is also found. These points are projected onto the x, y and z axes and fit to lines so that a parametric representation of the path of the photon can be inferred. The trajectory of the photon can be written as

$$\vec{d}(s) = \vec{a} + s\vec{c}. \tag{6.6}$$

where the vectors $\vec{a}$ and $\vec{c}$ represent a point in (x, y, z) space on the trajectory and

the direction of the photon, respectively. The vector quantities are determined from a series of linear fits. If the shower positions are determined correctly, $\vec{c}$ should be parallel to the photon momentum and, by construction of the fit, $\vec{a}$ will will be the point where the photon struck the BCAL inner surface. In the current reconstruction code, the vector pointing from the target centre to $\vec{a}$ is taken as the photon momentum. The algorithm does not *need* to assume the track originates at the target centre but the systematic uncertainties in reconstructing the photon momentum without the target as the vertex have not been explored. The errors on $\vec{a}$ are used in forming the the photon error matrix, which will be discussed later.

6.2.4 Calibration of the BCAL

The recorded photon energy in the Monte Carlo is the total energy deposited in the material of the BCAL and FCAL. This, however, will not be equal to the initial incident photon energy: some energy will leak out the back side, the inner face, and/or the ends of the BCAL; or the photon will shower in the CDC, FDC or their signal cables (which run the length of the inner face of the BCAL) before entering the calorimeter. If the mean loss of energy and response of the calorimeter is known as a function of position and incident energy, a calibration constant can be applied to the recorded MC energy to correct the reconstructed energy for these losses.

In order to calibrate the BCAL, the detector was uniformly illuminated in ϕ, z from 30 to 370 cm and energy between 0 and 4 GeV with photons thrown from the centre of the target. In the global coordinate system, the upstream edge of the BCAL begins at $z = 17$ cm and the downstream edge is at 407 cm. Only photons that produced a single shower were considered. The response of the detector is expressed as the ratio of reconstructed energy, E_{rec}, to generated energy, E_{gen}, versus position

on the front of the BCAL, Z_{gen}, and is shown in Fig. 6.2a. The response is noticeably non-linear as a function of position. Likewise, the response of the detector as a function of E_{gen} for 100 cm $<$ z $<$ 120 cm is shown in Fig. 6.2b and is also non-linear as a function of energy. The region from 370 cm to 390 cm was calibrated in a separate step, as the showers can leak out the ends of the BCAL, and the response is quite different than the region less than 370 cm, but the method was the same. The end region of the BCAL is expected to see a large portion of the photons from η and π^0 decays so it is important that photons can be reconstructed near the end, even with degraded resolution. The response of the detector as a function of Z_{gen} and E_{gen} for 390 cm $<$ z $<$ 395 cm is shown in Figs. 6.2c and 6.2d.

At a given position on the BCAL, the response of the BCAL is slightly non-linear as a function of shower energy due to leakage out the front and backside of the detector. This slight non-linearity can be corrected for with a power law function of the form

$$E_{corr} = A \cdot E_\gamma^{1+\epsilon} + B.$$ (6.7)

An invertible function is required in order to calculate E_γ from E_{corr}. The relative positioning of the shower within the BCAL, as well as the material in front of the BCAL, changes with z due to the photon's trajectory from the target. As a result, the parameters A, ϵ and B depend on the shower's z-position. The ratio of corrected energy to generated energy will also allow for the energy resolution to be calculated from MC such that Eq. 6.7 is rewritten as

$$\frac{E_{corr}}{E_\gamma} = A(z) \cdot E_\gamma^{\epsilon(z)} + \frac{B(z)}{E_\gamma}.$$ (6.8)

The functions $A(z)$, $\epsilon(z)$ and $B(z)$ can be determined by fitting Eq. 6.8 to the

(a)

(b)

(c)

(d)
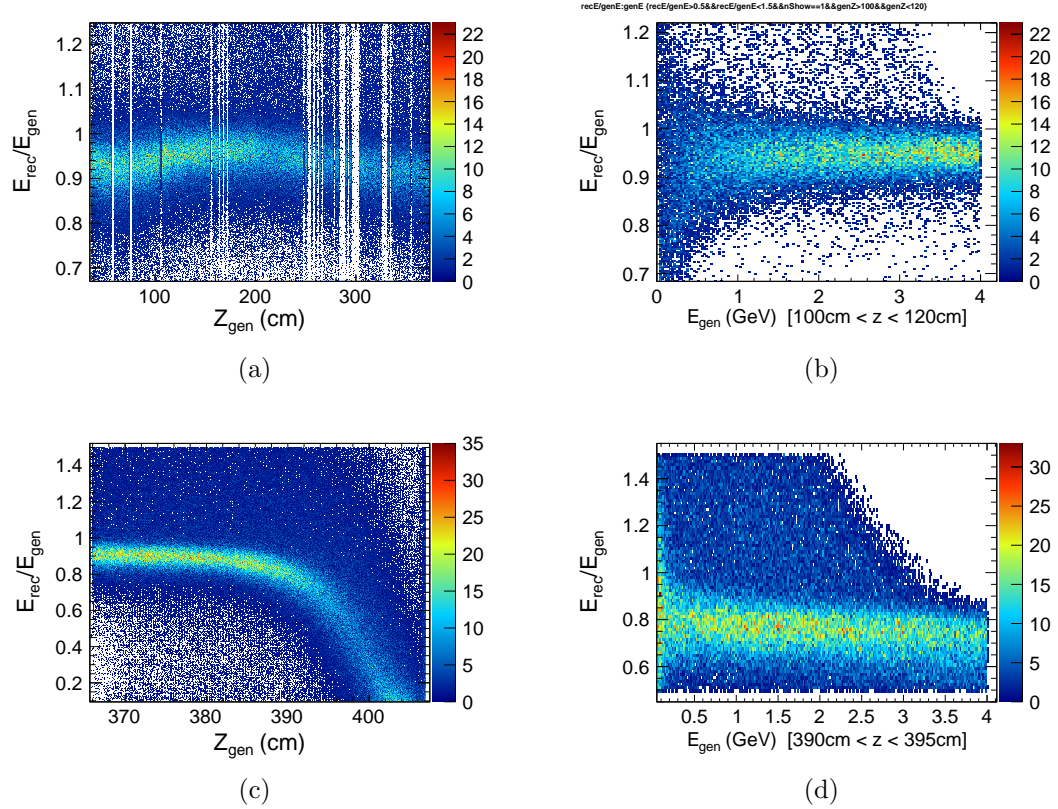
Figure 6.2: The uncalibrated response of the BCAL. The fits require an invertible, non-linear function to fit the spectra at multiple z-positions. (a) Response versus Z_{gen} in the region $30 - 370$ cm. (b) Response versus E_{gen} between 0 to 4 Gev in the region of 100 cm $< z <$ 120 cm. (c) Response from 365 to 400 cm. (d) Response over 0 to 4 Gev at 390 cm $< z <$ 395 cm. Gaps in the data are due to missing data files. *(original in colour)*

data for small discrete regions of z. The results for parameters $A(z)$, $\epsilon(z)$ and $B(z)$ can be seen in Figs. 6.3c, 6.3b and 6.3c, respectively, with polynomial fits shown.

(a) $A(z)$

(b) $\epsilon(z)$

(c) $B(z)$
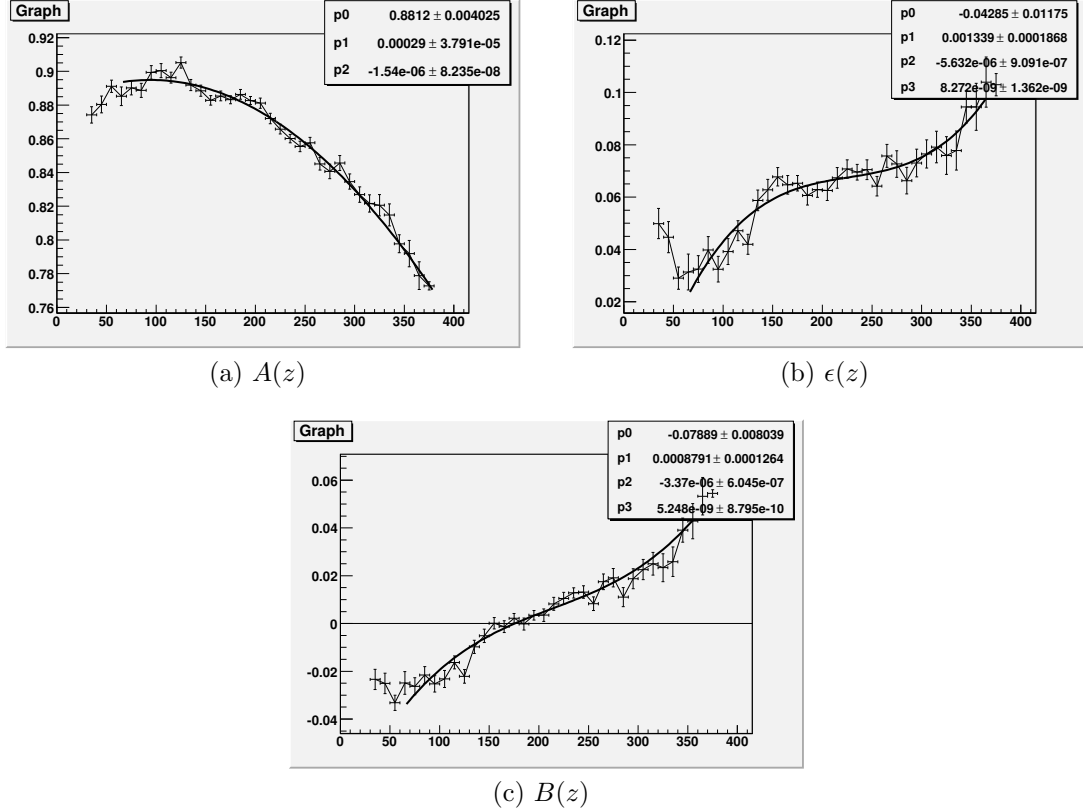
Figure 6.3: The parameters from fitting Eq. 6.8 to spectra of E_{rec}/E_{gen} versus E_{gen} for discrete z positions from 30 to 370 cm. The parameters $A(z)$, $\epsilon(z)$ and $B(z)$ are shown in (a), (b) and (c), respectively. Polynomial fits to the data are also shown. The response of the BCAL is expected to be symmetric about the target ($z = 48$ cm).

The polynomial fit for each parameter is used to calculate the calibration constants in Eq. 6.8. The reconstructed energies after calibration from the BCAL are shown in Fig. 6.4.

From Fig. 6.4, the resolution of the calibrated reconstructed energy degrades significantly in the region from 395 to 407 cm. Although this is a relatively large range in z, it subtends a small polar angle from 10.2° to 10.6°. This region extends the effective gap between the BCAL and FCAL. The calibration software coding developed

(a)   (b)

(c)   (d)
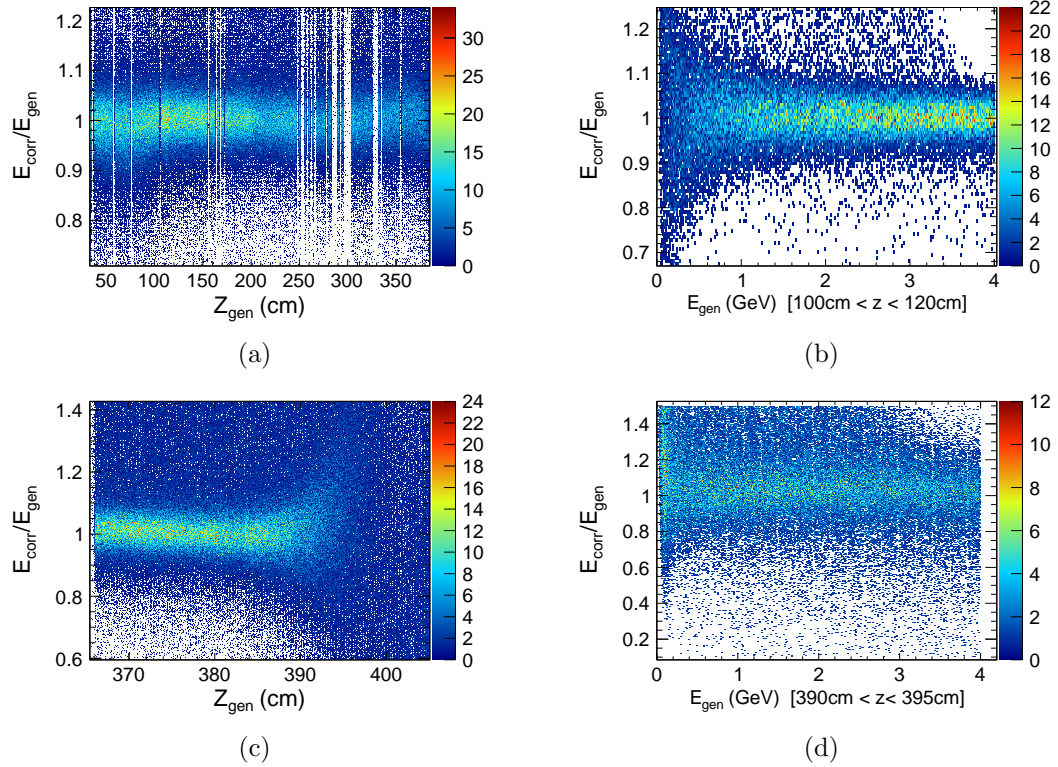
Figure 6.4: The calibrated response of the BCAL similar to Fig. 6.2 but now for corrected energies. The response along the BCAL is still not perfectly flat in these figures. This is a result of the difficulties of fitting an invertible, non-linear function to spectra at multiple z-positions. However, the calibration is within a couple percent of unity. *(original in colour)*

from the above work is implemented in the "BCAL Photon" step of Fig. 6.1.

6.2.5   Energy and Position Resolution

The energy resolution of the BCAL was examined using 0 to 4 GeV photons incident in the z-region of 30 cm $< z <$ 395 cm. Fig. 6.5 shows photon energy resolutions as a function of generated energy after the non-linear energy correction described above is applied. The energy resolution was fitted with the standard relation

$$\frac{\sigma_E}{E} = \frac{A}{\sqrt{E}} \oplus B \, , \tag{6.9}$$

where the $\oplus$ indicates addition in quadrature, B is some small ($< 1\%$) floor term and the statistical term $A \approx 5.5\%$. As a result of the shower developing at different orientations in the BCAL for different z positions, it is expected that the energy resolution will have some small dependence on position, as the stochastic term in the energy resolution is dependent upon shower fluctations and the floor term has some dependence upon shower losses. Where leakage out the end of the module is significant, near $z =$400 cm, shown in Fig. 6.5c, the energy resolution in the Monte Carlo simulation appears degraded. The results for the resolution (less than 380 cm) agree well with the JLab beam test results.

Fig. 6.6 shows the difference in generated and reconstructed z-position and polar angle at the inner face of the BCAL for 30 cm $< z <$ 380 cm. The error in the polar angle can be written in terms of the z-position error as

$$\delta\theta = \frac{r}{z^2 + r^2}\delta z \tag{6.10}$$

Due to the z^2-depedence in the denominator of Eq. 6.10, the z-resolution is seen

(a)

(b)

(c)
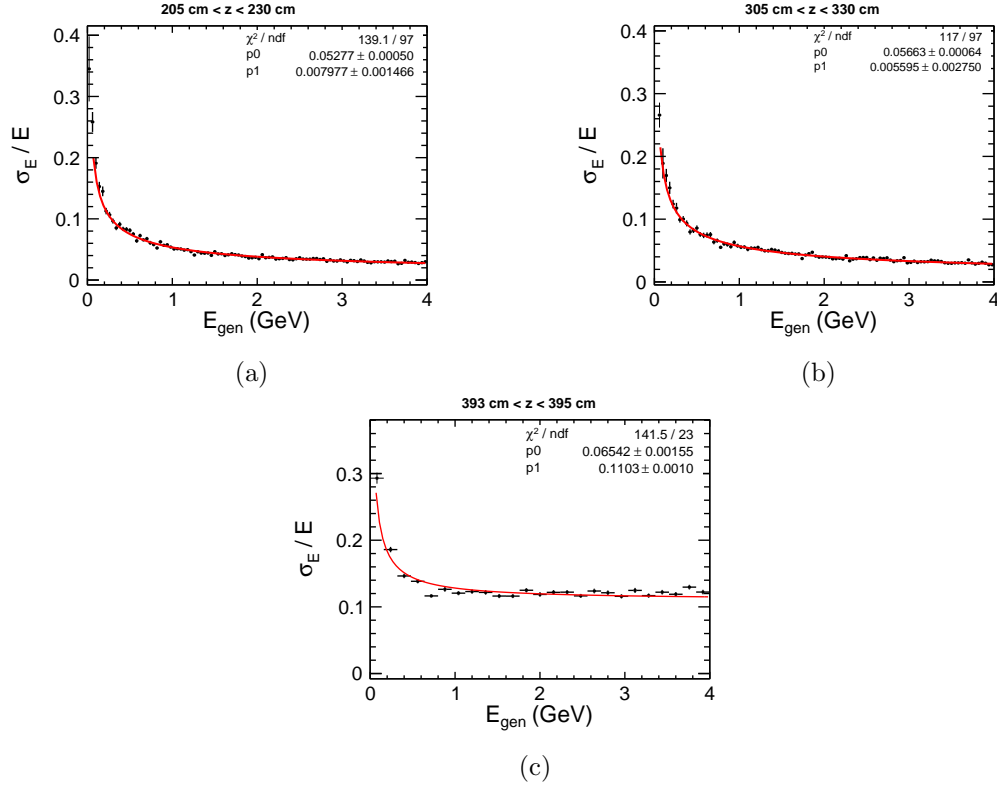
Figure 6.5: A fit to the standard deviation of the fractional energy error, σ_E/E as a function of generated photon energy for the regions (a) 205 cm $<$ z $<$ 230 cm, (b) 305 cm $<$ z $<$ 330 cm and (c) 393 cm $<$ z $<$ 395 cm. The data are fit to a function of the form in Eq. 6.9 where $p0 = A$ and $p1 = B$ in the figures. *(original in colour)*

to degrade in Fig. 6.6e with increasing z, while the θ resolution improves, as seen in Fig. 6.6f. The reconstruction of the cluster position implements time smearing determined from the time difference resolution measured in the JLab beam test. Seen in Fig. 6.6e, the z-resolution along the length of the BCAL is $\sim$ 1 cm and degrades to 1.5 cm towards the downstream end of the BCAL. The polar angle resolution, seen in Fig. 6.6f, is ~ 10 mrad near the target and improves to ~ 1 mrad after a couple hundred cm's downstream.

The downstream end of the BCAL was examined more closely, as the resolutions are expected to be much worse in this region. Fig. 6.7 shows the differences in generated and reconstructed z-positions and polar angle and their resolutions for the downstream end of the BCAL. Up to 397 cm, the differences and resolutions compare well to those upstream, but after 397 cm, the shower positions are not reconstructed well, with the difference between the reconstructed postion and generated position devating from zero by more than a few cm. The reduction in intensity after 397 cm also demonstrates a clear degradation in reconstruction efficiency.

The resolution in azimuthal angle, ϕ, is derived from the reconstructed shower position in the transverse plane, as a result of the energy-weighted position of the cells in the cluster. The azimuthal angle does not require smearing as a result of timing resolution, unlike σ_z and σ_θ and, as a result, the accuracy of the azimuthal resolution will only depend on the faithfulness with which HDGEANT produces electromagnetic shower profiles and the coarseness of the readout segmentation. Fig. 6.8 shows the difference in reconstructed and generated azimuthal position and the azimuthal resolution for the length of the BCAL and the end region. The calculated resolution of 5 to 6 mrad is better than the design goal of 8.5 mrad.

Overall, the energy resolution obtained from the MC simulations of both calorime-
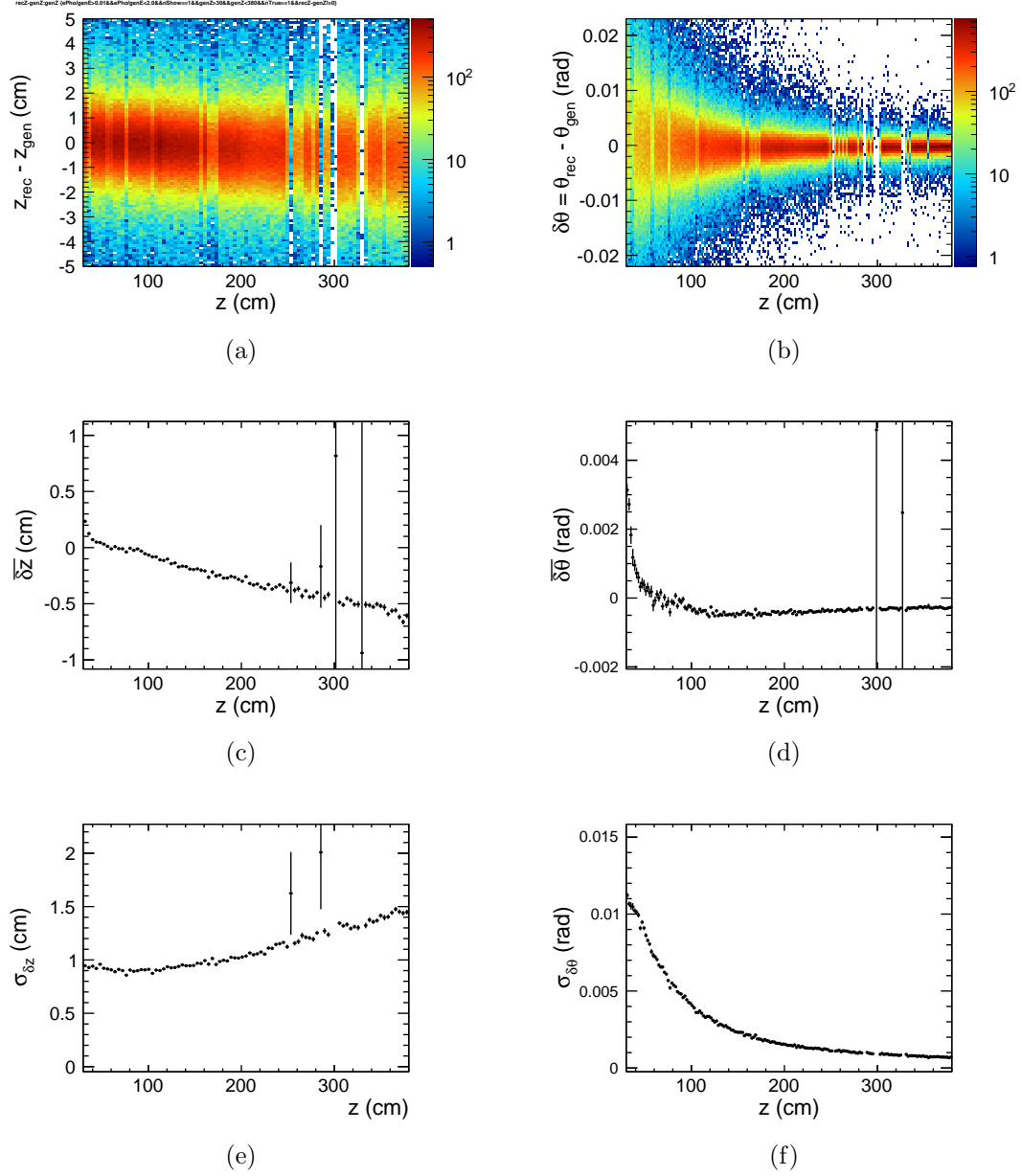
Figure 6.6: Differences in the reconstruction error for z position (left) and polar angle (right) of photon impact points on the inner face of the BCAL for 30 cm $< z <$ 380 cm. Distributions are seen in (a) and (b). The means of the distributions are shown in (c) and (d). The standard deviations of the distribution are shown in (e) and (f). Gaps in the data are a result of missing data files. *(original in colour)*
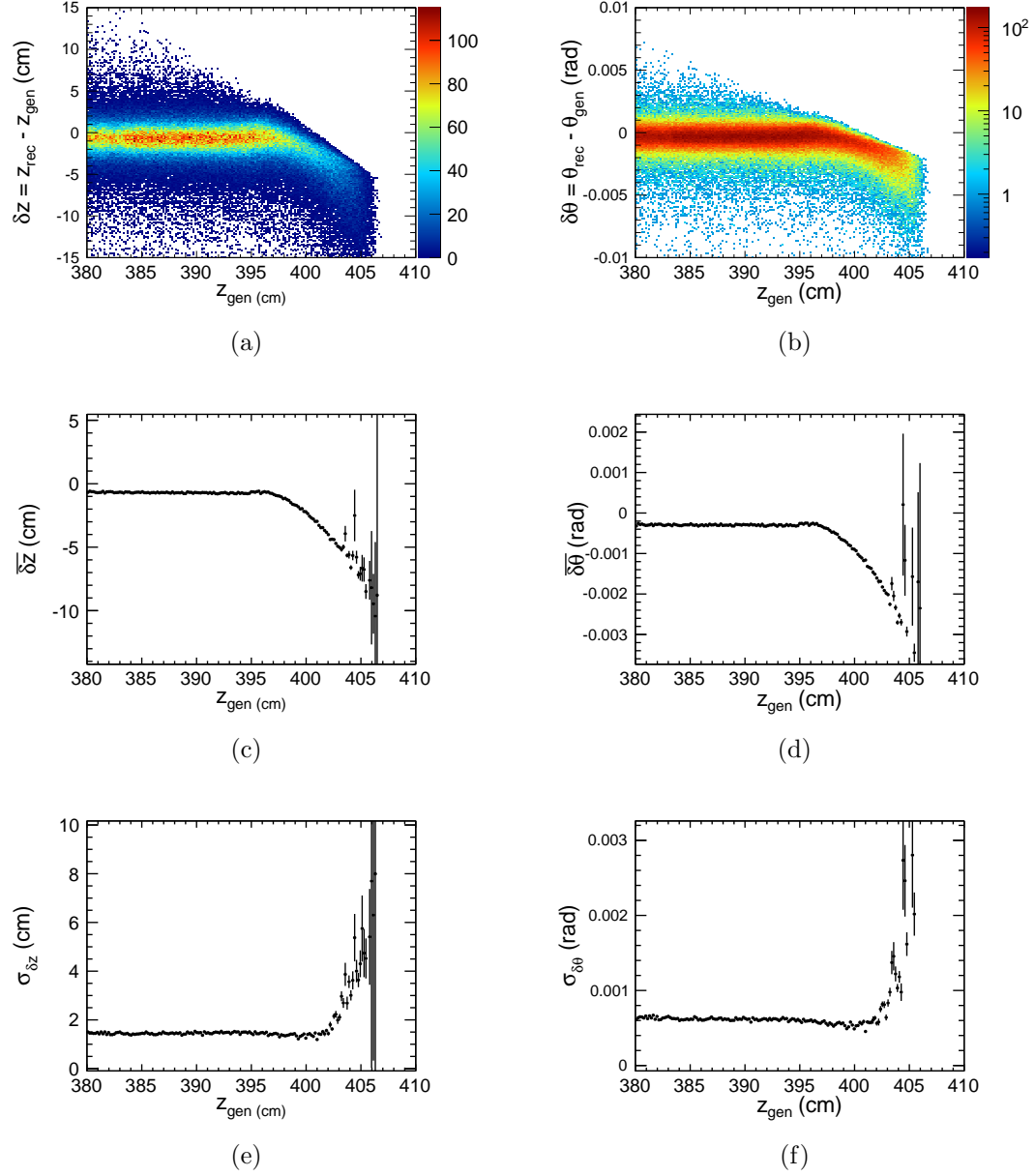
Figure 6.7: Differences in the reconstruction error for z position (left) and polar angle (right) of photon impact points on the inner face of the BCAL for 380 cm $< z < 407$ cm. Distributions are seen in (a) and (b). The means of the distributions are shown in (c) and (d). The standard deviations of the distributions are shown in (e) and (f).
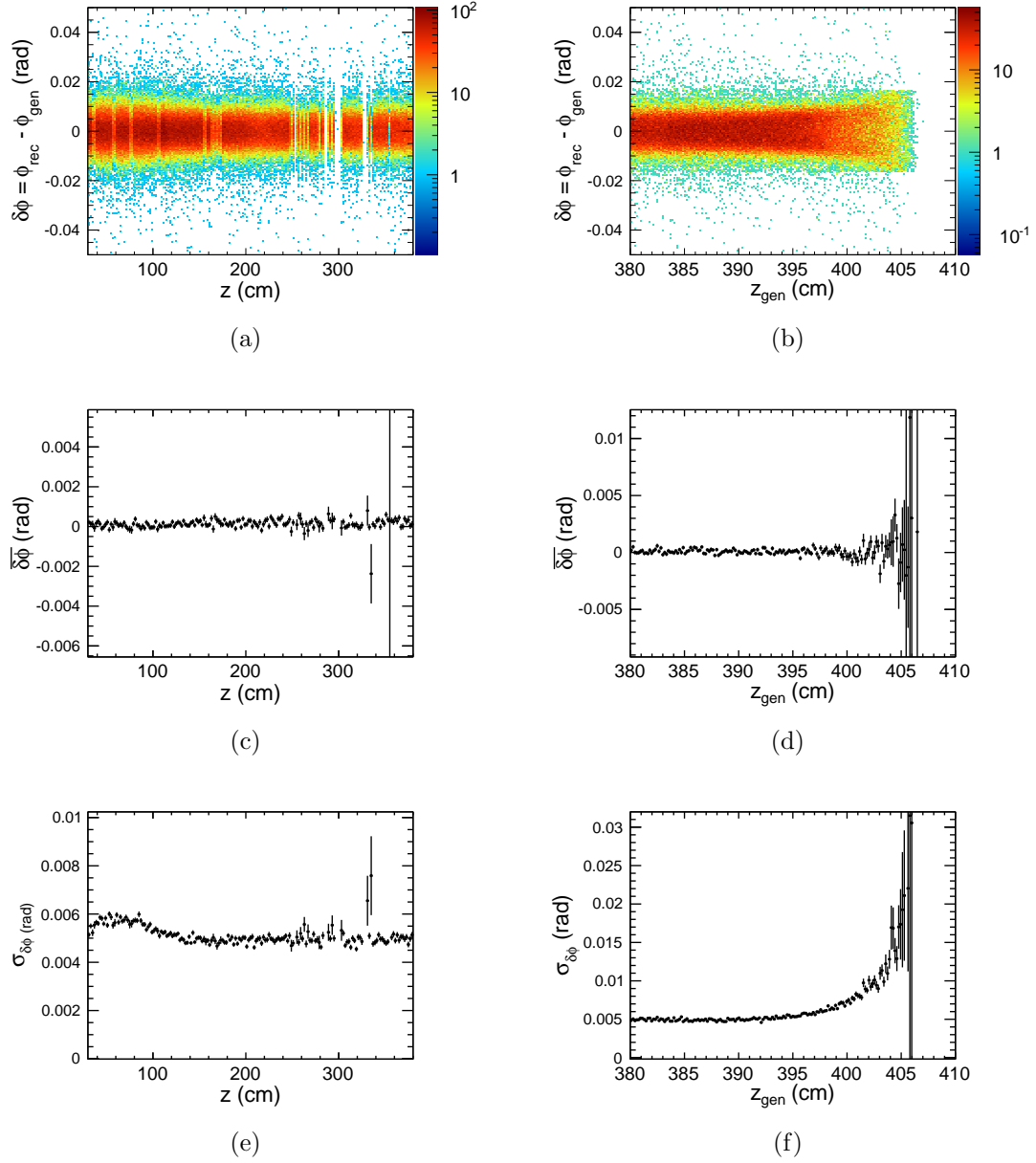
Figure 6.8: Differences in the reconstruction error for the azimuthal angle of photon impact points on the inner face of the BCAL for 30 cm< z <380 cm (left) and 380 cm< z <407 cm (right). Distributions are seen in (a) and (b). The means of the distributions are shown in (c) and (d). The standard deviations of the distributions are shown in (e) and (f). *(original in colour)*

ters are similar to the beam test measurements and past experience from the KLOE calorimeter. Better modeling of the threshold and noise of the readout electronics has also resulted in a similar floor term ($\sim 1\%$) in the energy resolution not seen before in other MC calculations. More advanced modeling of the time difference resolution demonstrated a degradation of the z-position resolution as expected. Continued studies and new beam test data may further improve the accuracy of the modeled resolution and understanding of the systematic errors in the reconstruction of data, especially at the downstream end of the BCAL.

6.3 FCAL Simulation and Reconstruction

The reconstruction software package for FCAL photons is based on that used for the RADPHI experiment [136]. Similar to the BCAL, the algorithm groups hits in the FCAL into clusters. The method is an iterative process in this case, selecting the highest energy block as a seed to begin a cluster. Other blocks within a 25 cm radius which record a hit are included in the cluster with the energy summed according to a radial profile defined by exponential and logarithmic functions. The process continues with a new seed from the remaining blocks until all blocks are assigned with a minimum of two blocks required to form a cluster. The threshold for photon detection is 100 MeV. After the clusters are formed, the cluster energy and position are then corrected for known shower depth and non-linear effects.

6.3.1 Energy and depth corrections

Much like the BCAL, the FCAL suffers from a non-linear energy response which is a result of two competing effects. First, when the photon energy increases, the core of the shower in the lead glass moves towards the downstream face of the FCAL and

reduces the attenuation of light before it reaches the phototubes. This increases the relative gain of higher energy photons with respect to low energy photons. However, shower leakage out the back of the FCAL increases for higher energy photons and begins to reduce the relative gain of the higher energy photons. The result is that the reconstructed energy has a weak dependence on shower energy. The non-linear equation used to correct the energy is the same as that for the BCAL, Eq. 6.7, although in the case of the FCAL the parameters do not have the same dependence on position as the face of the FCAL is flat. The parameters in Eq. 6.7, for the FCAL, are approximately $A = 0.65$, $\epsilon = 0.035$ and $B = 0$. A depends mainly on the attenuation length in the glass.

6.3.2 Energy and Position resolution

While a beam test of the FCAL has yet to be done, and previous experience from RADPHI should predict the correct resolution for the FCAL, the resolution of the FCAL was also calculated from MC. A resolution of the form in Eq. 6.9 was found where the statistical term of $(5.7\%\oplus0.3)\%$ was determined with a negligible floor term. Fig. 6.9 shows the photon energy resolution as a function of generated energy after non-linear energy and depth corrections were applied. Figure 6.10 shows the absolute error in polar (left) and azimuthal (right) angle versus generated polar angle. The error in polar angle does not depend on actual shower position at the face of the FCAL. In the case of ϕ, one can see the effect of the finite FCAL block size at small polar angles.
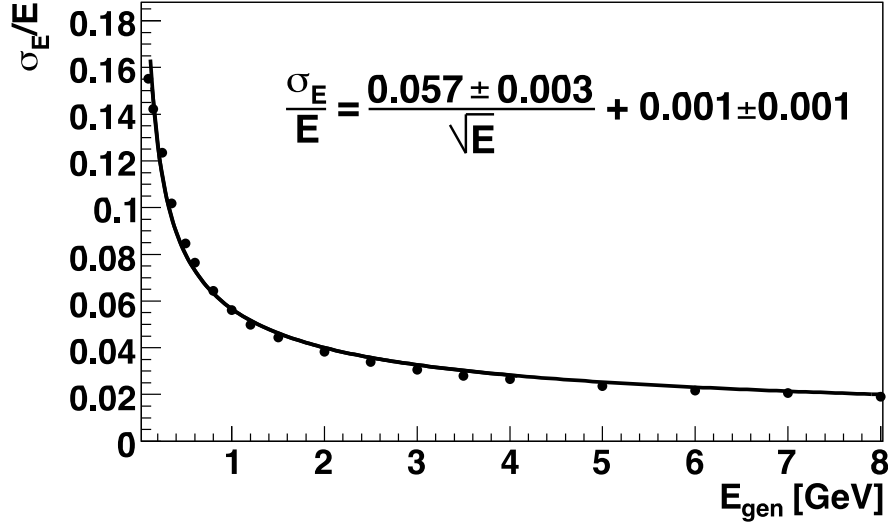
Figure 6.9: Fractional energy resolution from the FCAL as a function of generated energy after energy-corrections were applied. Figure from Ref. [137].

6.3.3   Determination of Photon Momenta

The reconstruction algorithms for both the BCAL and FCAL measure the shower position, $\overrightarrow{r}$ and the energy of the shower after corrections , E_{corr}. The 4-momentum of the photon is determined from these quantities:

$$E_\gamma = E_{corr} \tag{6.11}$$

$$\overrightarrow{p}_\gamma = \frac{(\overrightarrow{r} - \overrightarrow{v})}{|\overrightarrow{r} - \overrightarrow{v}|} E_\gamma, \tag{6.12}$$

where $\overrightarrow{v}$ is the vertex position of the photon, which is currently the centre of the target with errors given by the size of the target. In the experimental data analysis, the vertex postion will be measured by finding the origin of the charged particle tracks or from the missing momentum in the case of a missing proton track and
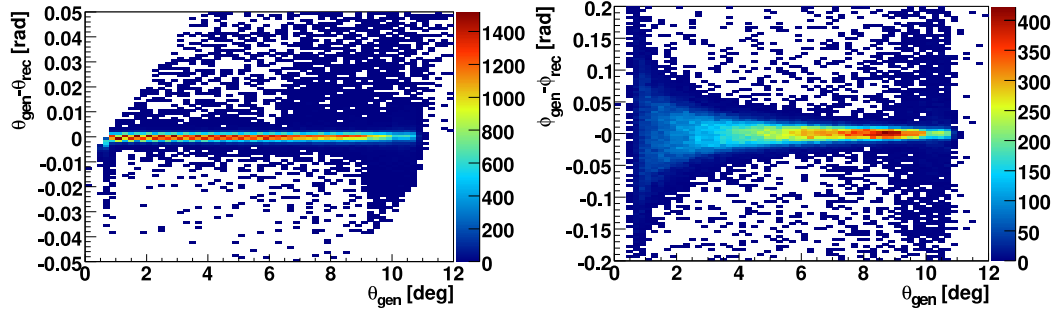
Figure 6.10: Polar (left) and azimuthal (right) angle errors vs. generated polar angle after energy/depth corrections were applied. Figure from Ref. [137]. *(original in colour)*

purely neutral decays.

6.3.4 Expected Photon Distributions

From the simulation of PYTHIA events for a 9 GeV photon beam on a proton target, the distributions in momentum and polar angle for decay photons can be examined. This distribution is illustrated in Fig. 6.11a. Insight can be gained into the required dynamic range of the detectors from the expected photon distribution as well, as the regions where good efficiency is required are highlighted. The generator level information from PYTHIA indicates that 71% of the total number of photons have a polar angle in the region covered by the BCAL with the majority near the downstream end; 27% of the total number of photons will enter the FCAL, as seen in Fig. 6.11b. Fig. 6.11c shows that 90% of the photons entering the BCAL have momentum less than 1 GeV, 95% less than 1.4 GeV and 99% less than 3.5 GeV. Fig. 6.11d shows that 90% of the photons entering the FCAL have momentum less than 3.3 GeV, 95% less than 4.1 GeV and 99% less than 5.8 GeV. In an ideal system, the dynamic range of the readout and detector would cover all of the phase space, but cost and detector space limitations dictate that linearity and acceptance might need be sacrificed at

the extremes of these ranges. However, where the polar region transitions from the BCAL to the FCAL near $\theta = 10.5°$ is not at an extreme and the efficiency here is important.

Thrown momentum vs. theta for gammas

Pythia Photons

(a)

(b)

Pythia Photons [BCAL only]

Pythia Photons [FCAL only]

(c)

(d)
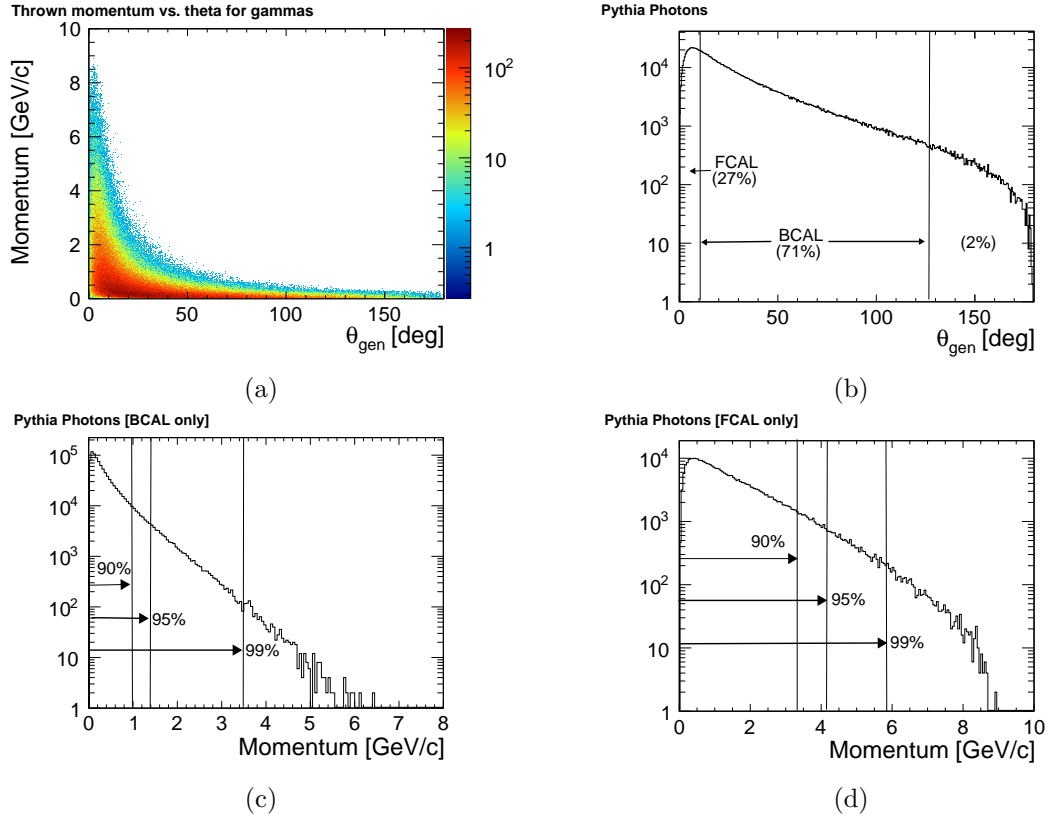
Figure 6.11: (a) Generated momentum vs. θ distribution for photons from PYTHIA decays. (b) The projection of (a) onto the θ axis. (c) The momentum distribution for photons which would strike the BCAL only. (d) The momentum distriubtion for photons which would strike the FCAL only. *(original in colour)*

6.3.4.1   Reconstruction efficiency

The efficiencies of the calorimeters are greatly affected by material in front of the detectors which convert some fraction of the photons into e^+e^- pairs. These e^+e^- may still deposit their energy in the calorimeters but the magnetic field may separate them further and produce multiple showers in the calorimeters resulting in multiple

clusters. Since the full HDGEANT simulation contains all the detectors and their materials, this efficiency has been studied and is well understood.

Fig. 6.12a shows the single photon conversion probability between the target and one of the calorimeters. The CDC and FDC were identified in simulations by other collaborators as large contributors to photon conversion that degrades the resolution of the calorimeters as well as reduces the reconstruction efficiency. The CDC end-plate and the FDC support structures have been modified to reduce the amount of material a photon would encounter before striking one of the calorimeters to minimize efficiency losses. Not all photons that convert are lost in some cases, however, as the e^+e^- may still produce a single cluster in the calorimeter. This is especially true of photons that convert in the plexiglass in front of the FCAL and photons that convert in the signal cables in front of the BCAL, even such that their resolutions are not degraded.

The reconstruction efficiency for photons in the forward region are shown in Figs. 6.12b, c and d. A photon is considered reconstructable if the reconstructed energy is greater than 50% of the thrown energy, shown with black data points. The significantly reduced efficiency at ~10.5° is the gap region between the BCAL and FCAL calorimeters. The green data points in Figs. 6.12c and d include only photons within $3\sigma_E$ of the generated energy for the appropriate calorimeter and within 0.05 rad of the generated polar angle. The photon conversion rate and reconstruction efficiencies for the entire angular region of the BCAL and FCAL, 0° to 120° are shown in Fig. 6.13. The lower efficiencies for photons less than 200 MeV along the length of the BCAL are seen in Fig. 6.13b. The average reconstruction efficiency for the BCAL, however, is on the order of 90%.

(a)

(b)

(c)

(d)
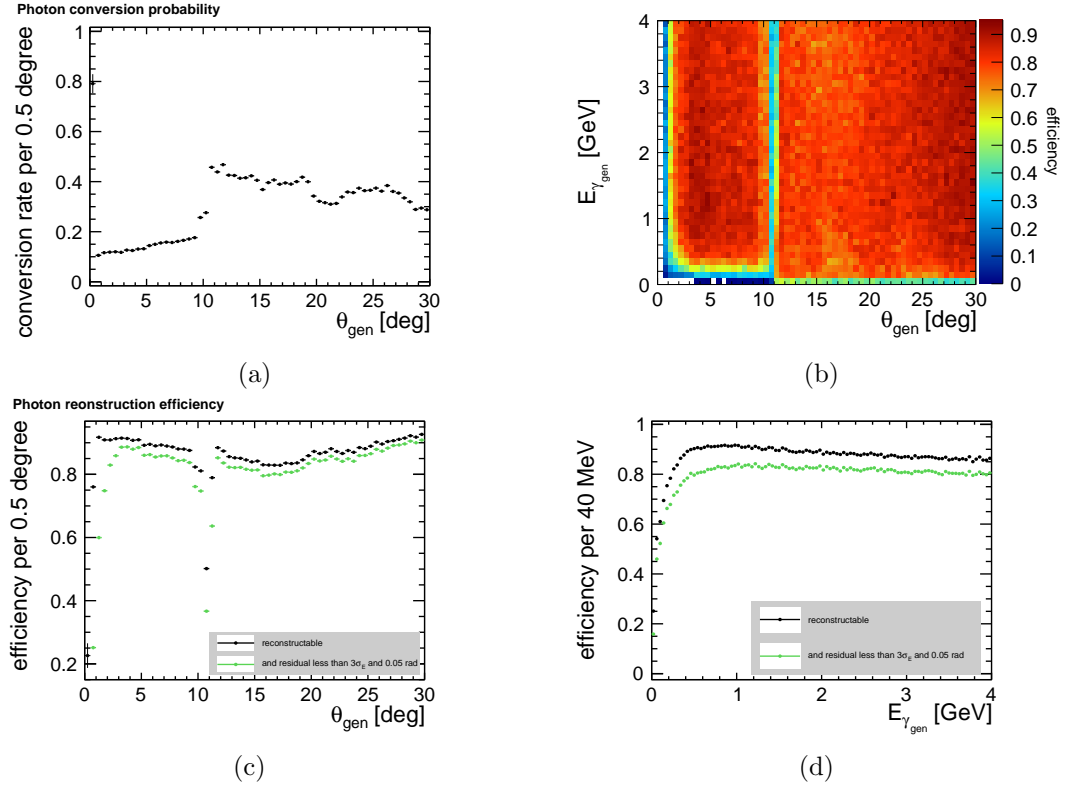
Figure 6.12: (a) Single photon conversion probability as a function of incident polar angle for 0° to 30°. The CDC end plate and FDC support rings can be indentified by the steps in conversion probablity. (b) Single photon reconstruction efficiency as a function of energy and polar angle. The gap between the BCAL and FCAL is clearly visible. Thresholds at low energy and low angle are also visible. (c) The polar angle projection of Fig. (b). The efficiency clearly degrades in the gap region. (d) The energy axis projection of Fig. (b). More details are given in the text. *(original in colour)*
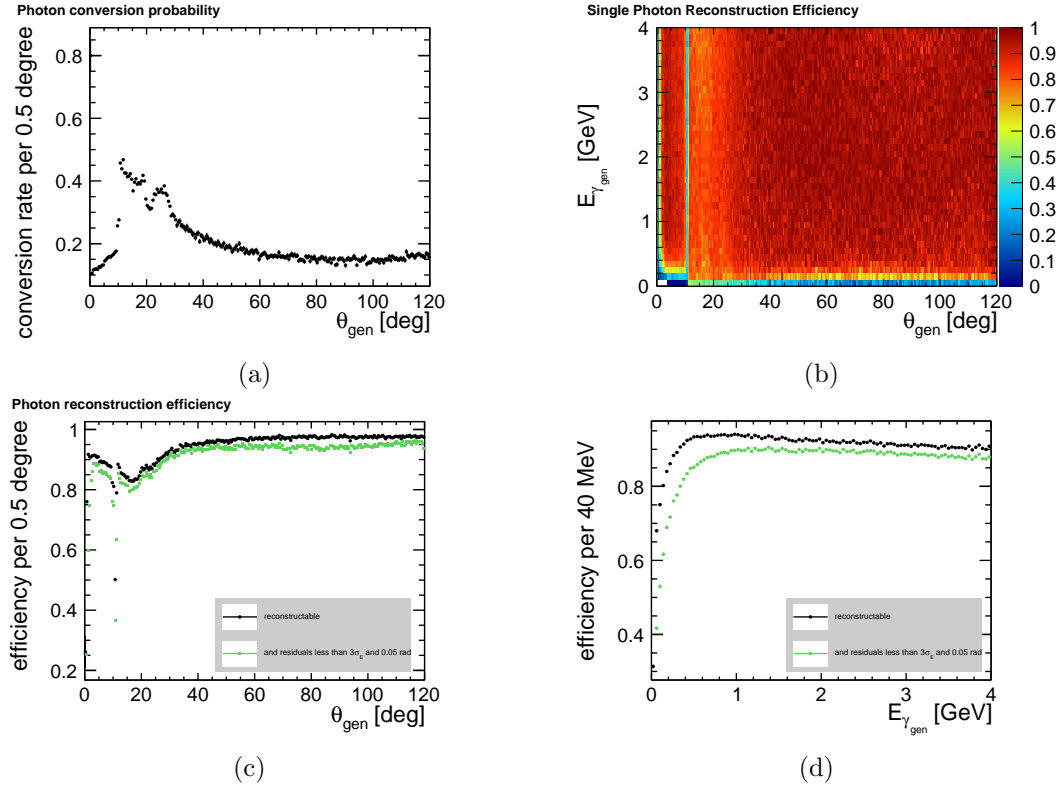
Figure 6.13: (a) Single photon conversion probability as a function of incident polar angle for 0° to 120°. The CDC endlplate and FDC support rings can be indentified by the steps in conversion probablity. (b) Single photon reconstruction efficiency as a function of energy and polar angle. The gap between the BCAL and FCAL is clearly visible. Thresholds at low energy and low angle are also visible. (c) The polar angle projection of Fig. (b). The efficiency clearly degrades in the gap region. (d) The energy axis projection of Fig. (b). More details are given in the text. *(original in colour)*

6.3.5 Determining Showers from Charged Particles

If a charged particle such as a proton or π^+ strikes the BCAL or FCAL and deposits a measurable amount of energy in multiple readout cells, the reconstruction code will still reconstruct these cells into a cluster and record them as being a possible photon hit or "DPhoton" object in Fig. 6.1. At this level, the code cannot distinguish what caused the shower cluster, only that a cluster occured with a certain amount of energy and was deposited at a certain position. However, if a charged particle has caused the shower, information from the tracking system will allow for the reconstruction algorithm to determine the source of the shower.

Currently, the charged particle tracking code is quite slow and consumes large amounts of CPU time. In its place, a simple routine was written that calculates where the particle, after momentum smearing, would strike the face of either the FCAL or BCAL had it actually have been propagated though the solenoidal magnetic field. This routine does not track the particles through the material and, as a result, multiple scattering in the material of the other detector packages is not treated. This means that the calculated position on the calorimeter face may not be the same as if the particle were propagated through the materials, resulting in some error in identifying DPhoton clusters from charged particles. Improvements to this routine are planned in order to reduce uncertainties.

This work was done as a precursor to studying the $\gamma p \rightarrow \eta \pi^0 p \rightarrow 4\gamma p$ reaction where the majority of the protons strike the BCAL. DPhoton clusters produced by the final state protons need to be separated from ones produced by the decay photons. To study the cuts that would need to be applied to tag DPhoton showers as being from charged particles, protons and pions were generated with momenta from 0 to 2 GeV/c from the target in HDGEANT such that they would illuminate the face of

BCAL evenly in z and the calculated positions of the charged particle on the face of the BCAL was compared to the reconstructed position of the DPhoton shower. The differences in z and ϕ for protons are shown in Fig. 6.14. The distributions are similar for pions. Negatively charged pions and protons show a similar offset from zero in the negative direction. Based on the width of the distributions, a 3σ cut is used to tag DPhoton showers as being from a charged particle. Similar work is being done by other collaborators for the FCAL.

6.4 Charged Particle Track Reconstruction

While the full charged particle track reconstruction was not used in this work, some mention of how it functions is included in this thesis for completeness. Reference [138] describes the track fitting studies in greater detail. Charged particle tracking in the GLUEX detector in Hall-D primarily involves two detector systems: The Central Drift Chambers (CDC) and the Forward Drift chambers (FDC). The BCAL will have some ability to distinguish pions from protons, but this is not included in any reconstruction algorithms as of yet.

The reconstruction algorithm for hits in the CDC is a seed-based track finder. Hits in the X-Y plane of each layer of axial wires and stereo wires are analysed to form a cluster which is the basis of a seed. In a uniform magnetic field pointing along the beam-axis, hits on a track form a circle when projected onto a plane normal to the beam-axis. A seed is fit to the circle and the intersection of the stereo wires with the circle is used to find the z-location of the stereo-wire hits. The location of the wire in the X-Y plane provides a point in 3D space such that the polar angle θ and z-location of the vertex can be found. The circle fit to hits in the axial wires is used to estimate the transverse momentum and the azimuthal angle ϕ can be estimated.
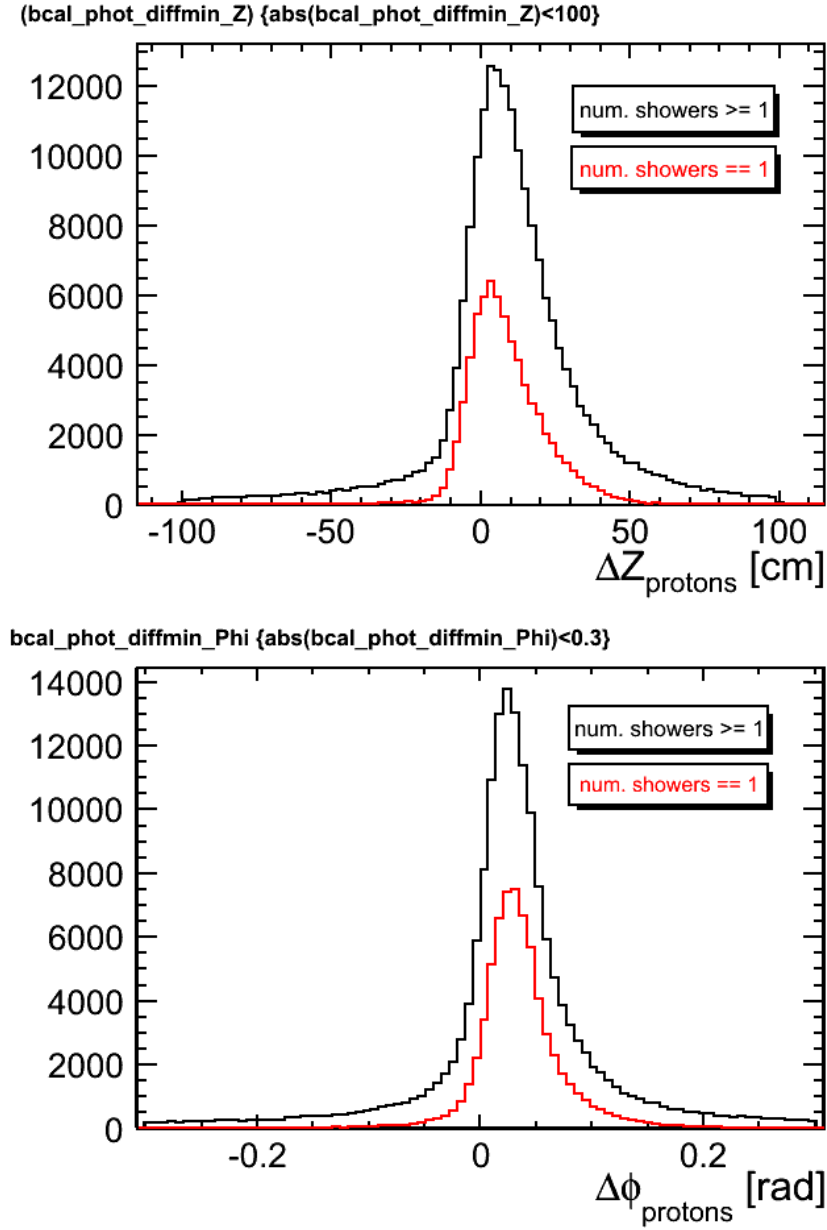
Figure 6.14: The difference between calculated calorimeter position z (top) and ϕ (bottom) and reconstructed DPhoton cluster position for protons. *(original in colour)*
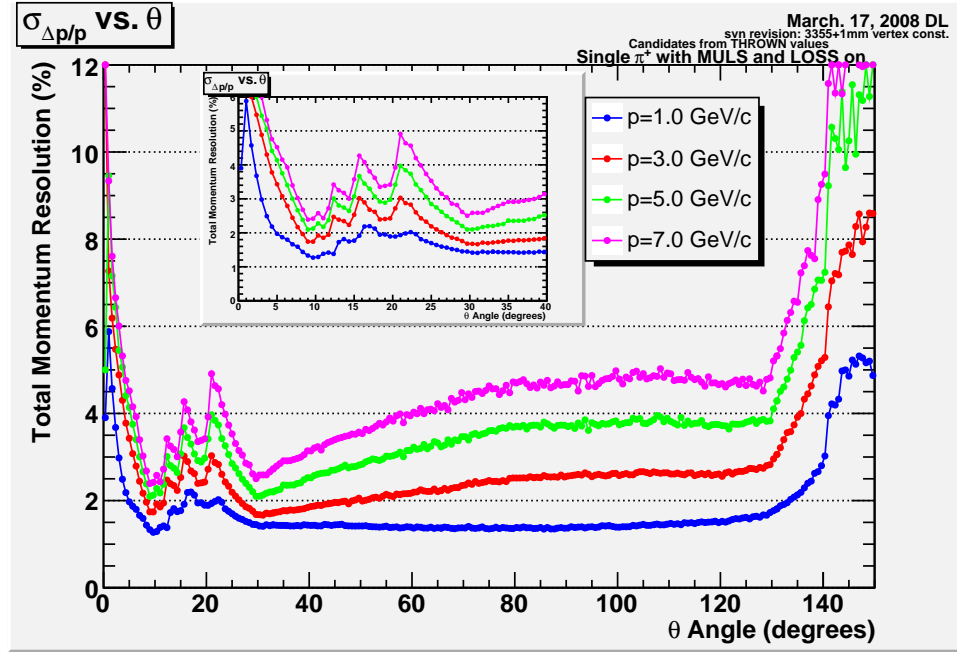
Figure 6.15: Total momentum resolution as a function of θ for various values of the total mometum. From Ref. [138]. *(original in colour)*

The reconstruction of tracks in the FDC is done similar to what is done for the CDC, by fitting circles to hits in the wire and cathode planes. However, as the FDC consists of four packages with separate positions in z, each package forms a segment of a track which is used as a seed for forming the entire track using a helical track model. The candidate track momentum and vertex positions are determined from the parameters of the helix. Momenta resolutions from MC are shown in Fig. 6.15.

6.5 BCAL Readout Segmentation Options Study

Before the final design of the BCAL readout was decided, there was a great deal of discussion concerning the photosensors that would be used. The large area silicon photomultiplier was still going through stages of research and development and had
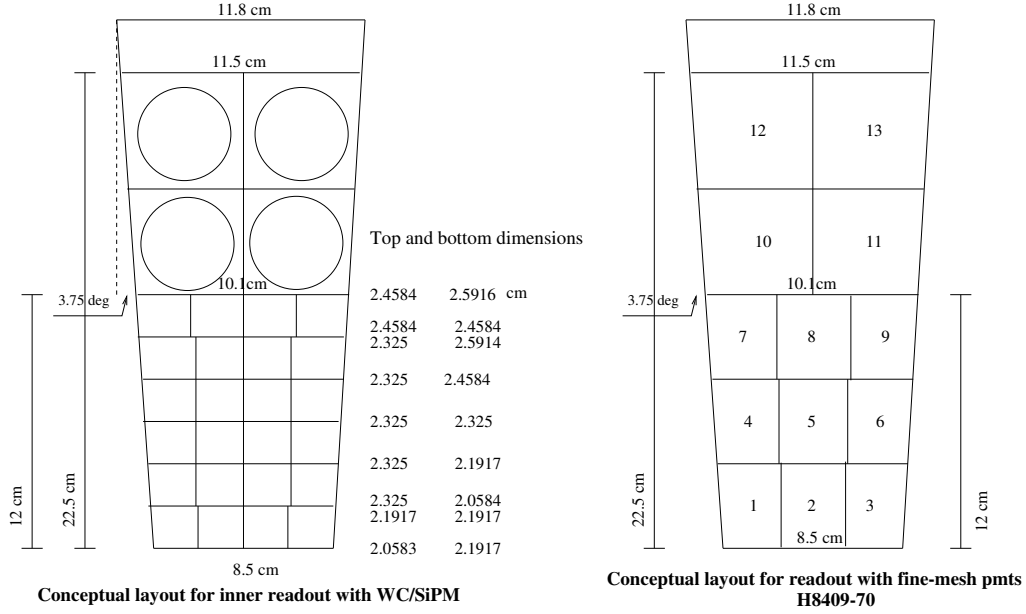
Figure 6.16: Layout on the face of one module showing the segmentation for the two options considered for readout of the BCAL. On the left is the SiPM readout for the inner region and FM PMTs for the outer region. On the right is the option for the segmentation using FM PMTs only.

not yet met the criteria for noise, stability and gain requirements. The other option being discussed was a magnetic field resistant fine-mesh photomultiplier tube (FM PMT). FM PMTs were used in the KLOE detector [139], but their operation is limited to fields below 0.5 T, and they exhibit considerable sensitivity to the orientation of the field relative to the PMT axis. The GlueX collaboration has studied these two readouts in great detail weighing the pros and cons of each option. The different readout geometries are illustrated in Fig. 6.16.

The FM PMTs require long light guides and create a larger gap (by a factor of three) in the efficiency in the gap region between the BCAL and FCAL. The SiPM option also detects about four times more photoelectrons than the FM PMT configuration. This is slightly offset by the large dark rate (currently measured to be 60 MHz/sensor) in the SiPMs, compared to the negligible dark rate in the FM PMTs.

However, the effect of both of these factors results in a minimum energy threshold for the SiPM in the range of 50–54 MeV, compared to the threshold of 58–60 MeV in the case of the FM PMTs. This translates into a loss of accepted photons from about 15% to 20% for physics reactions of interest. The dynamic range covered by both options is approximately 1:500.

The work presented below was a study conducted by the author to measure the effect on the photon resolution of the different readout options in the Hall-D MC. Using the nominal HDGEANT MC simulation for the 6×4 SiPM configuration and a separate build of HDGEANT which contained the 3×3 FM PMT configuration, photons were thrown evenly along the length of the BCAL. Comparisons of the reconstructed energy, polar angle and azimuthal resolutions are presented in Figs. 6.17a, b and c. The far right panel in each figure is the ratio of the resolutions obtained for the 3×3 geometry compared to the 6×4 geometry. The energy resolutions are quite similar for the two different configurations but the polar and azimuthal angle resolutions are $\sim$30% better for the 6×4 SiPM configuration for higher energies near the downstream end of the BCAL. The slightly worse angular resulutions of the 3×3 configuration near the end of the BCAL are likely due to the lower multiplicity of cells that have recorded hits and larger cell size where shower fluctuations have a greater impact
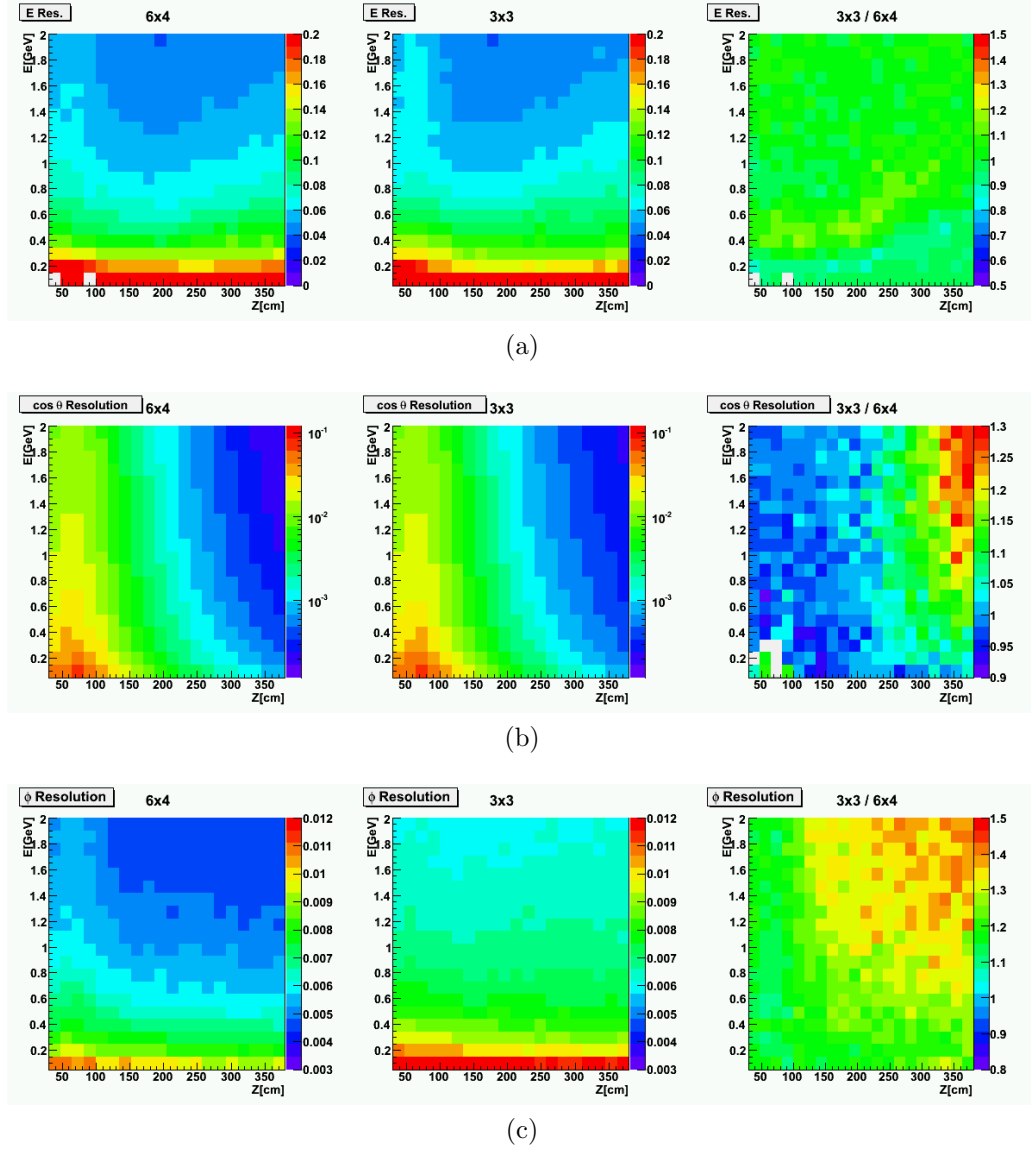
Figure 6.17: The (a) fractional energy, (b) $cos(\theta)$ and (c) ϕ resolutions as a function of energy and position of the 6×4 geometry and 3×3 geometry are shown in the left and middle panels respectively. The right panel is the ratio of the resolutions of the two geometries. *(original in colour)*

Chapter 7

Physics Signal Simulation and Reconstruction

The ultimate goal of the GLUEX project is to reconstruct exotic physics signals. However, before any exotic discovery can be claimed, it must be shown that the detector can reconstruct well understood systems. The experimental physics analyses will not be limited by statistics, due to the high flux of the photon beam, but will instead be limited by systematic uncertainties in the detector performance and systematic uncertainties in the phenomenology of the exotic hybrid mesons. These are states, after all, that have yet to be unambiguously identified. High statistics will also help to reduce the uncertainties in the phenomenology but the sensitivity to exotics and acceptance of the detector must be well understood. Validation of the detector design and an early attempt at understanding the systematics of the detector are done through Monte Carlo simulation of physics signals in the GLUEX detector, with reconstruction, aided by elements of the Hall-D software package.

The key issues in evaluating the performance of the GLUEX spectrometer in regards to reconstructing physics signals are signal purity and acceptance. Pure

samples of exclusive final states are preferable for amplitude analysis. However, these require an understanding of the background with an ability to distinguish between various amplitudes, which depend on detector acceptance. The work discussed in this chapter is part of the vanguard attempt in the collaboration to reconstruct physics signals with the current versions of software in order to determine where problems lie and what improvements are needed.

7.1 Event Generation

7.1.1 Signal Generators

There are two signal event generators used in GLUEX. GENR8 [140] is a C-based program that generates peripheral phase space Monte Carlo events. The events produced can be a result of a complex decay chain of intermediary states with both meson and baryon decays allowed. However, the decays must be limited to t-channel production processes and are produced isotropically. The distribution of the four-momentum transfer squared, $|t|$ follows the form:

$$\frac{d\sigma}{dt} \propto e^{-b|t|} \, . \tag{7.1}$$

Various models predict different values for b depending on the exchange mechanism involved, (e.g. two-gluon, Pomeron exchange or others). A slope parameter of $b = 5 \ (\text{GeV/c})^{-2}$ produces a reasonable approximation to experimental data for ρ and ϕ photoproduction for low momentum transfer $(-t \leq 0.4 \ (\text{GeV/c})^2)$ [141] and was used for this work. The momentum transfer squared generated in Monte Carlo, however, exceeds this and falls within the range $0 < -t < 2 \ (\text{GeV/c})^2$. Experimental data for meson photoproduction with $-t > 1 \ (\text{GeV/c})^2$ is meagre, and

where data does exist, Ref. [142] shows a smaller value for the slope parameter, $b = 3.4 \ (\text{GeV/c})^{-2}$. The effect of this parameter on reconstruction should be studied in future work.

The second generator, part of AMPTOOLS [143], produces events with defined amplitudes and proper angular distributions. This was needed as a generator for testing partial wave analysis (PWA) algorithms at IU. Since the orignal ultimate goal of this reconstruction and other related work was to attempt a simple PWA on the data passed through the GLUEX detector, the AMPTOOLS generator was used to generate sample resonances. However, the extended effort required to assemble a working set of reconstruction algorithms, to understand the function of the code and to generate and reconstruct the vast quantities of background data needed, necessitated that any amplitude analysis of signal and background be left to future efforts by others.

For both signal and background generation, the photon beam energy is set exactly at $E_\gamma = 9$ GeV, though the actual energy spectra of the photon beam for the experiment has a distribution with a peak at 9 GeV, similar to Fig. 2.5.

7.1.2 Background Generation and Filtering

The hadronic background was generated using the tuned version of PYTHIA, discussed previously. The relatively large cross section, compared to various signal channels of interest, requires a large amount of CPU time and disk space if a moderate amount of experimental beam time is to be simulated. In anticipation of studying the $\gamma p \rightarrow \eta \pi^0 \rightarrow 4\gamma$ reaction, it was found that, by studying a smaller PYTHIA data set, a set of cuts could be determined by examinining which events could possibly be mistaken for the all neutral decay of the $\eta \pi^0$ system. These were applied to the larger PYTHIA

data set before any detector simulation occured. The cuts that were found to be effective have the desired result of reducing the events that need to be simulated in HDGEANT to 4% of the original data set.

Since the signal event of interest for this thesis is an all-neutral final state with a recoil proton, a simple cut was identified by looking at the total number of charged particles for events that passed reconstruction. Fig 7.1 shows the multiplicity of charged particles in each generated event and the multiplicity of charged particles that pass the requirements needed for reconstruction. The events that also pass a kinematic fit probability cut (discussed below) are also shown. From that figure, it can be seen that there are very few events which have more than one charged particle and still pass reconstruction. This can be explained by the fact that the acceptance of charged particles in the GLUEX spectrometer is quite good. Among the 200,000 PYTHIA events simulated, no event with more than one charged particle passed a cut on the probability, from the kinematic fitter, of at least 1%. Since a probability cut is used to examine the signal, events having more than one charged particle, prior to any meson decay, were filtered out of the PYTHIA data set. These cuts will provide a good estimate for the background; however, they may not be a perfect estimate as the cuts are applied on truth (generator level) information directly from the generation process, rather than on data after reconstruction. To reduce the massive amounts of CPU time and disc space to manageable levels, some sacrifices in the faithful simulation of a real experiment must be made at this stage in reconstruction development.

Signal $\gamma p \rightarrow \eta \pi^0 p$ events produced in PYTHIA were removed in the filtering process as well in order to result exclusively in background event sets. PYTHIA was programmed not to decay the mesons to their final states so that the $\eta \pi^0 p$ states can

be removed from the generated data set. The mesons are later allowed to decay in the HDGEANT simulation. This has the unfortunate side effect of having final states in which the neutral kaons have predominantly decayed to charged pions or leptons, with some smaller fraction having decayed to neutral pions. The η's in background events are also left to decay to neutral or charged modes. These charged final states will be cut in reconstruction but are still available in the filtered background data set and available to be passed through the detector simulation. The default flags for the GEANT detector simulation are listed in Appendix A.
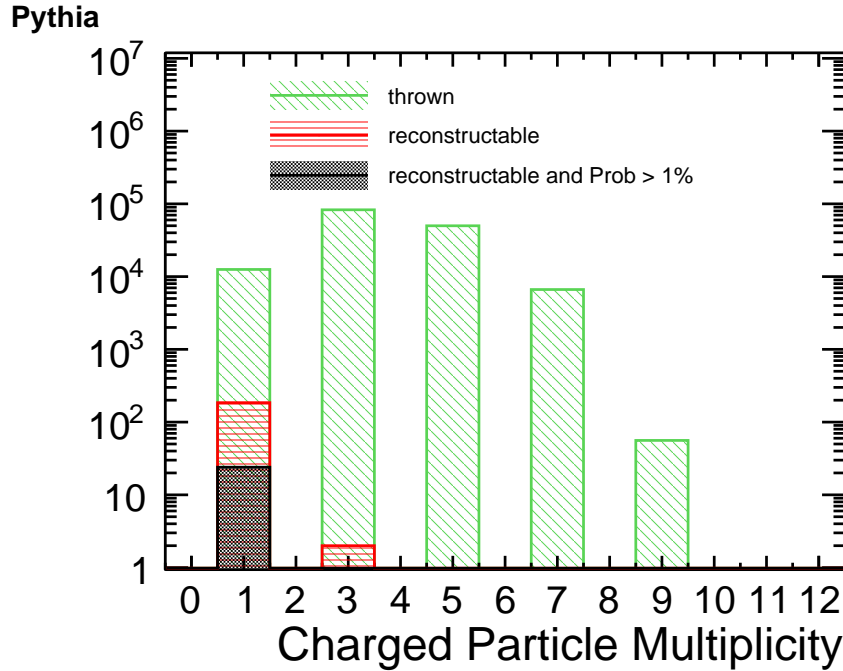
Figure 7.1: The charged particle multiplicity for 2×10^5 PYTHIA events and the events that pass reconstruction. *(original in colour)*

Considering that the final state for the signal is neutral, except for the recoil proton, the total energy of the neutral particles will have a narrow spectrum near 9 GeV. The PYTHIA background, however, will have a very broad total energy spectrum for neutral particles. Fig. 7.2 shows this for all PYTHIA events, $\eta\pi^0 \to 4\gamma$ signal

events, and PYTHIA events which are reconstructed; the total neutral energy for the $\eta\pi^0$ is overlayed. From the figure, a cut on the total energy of neutral particles with less than 7.5 GeV and greater than 9 GeV will further reduce the number of background events that should be simulated since those that fail the energy cut will not be possible reconstructed signal events. In reality, the resolution of the detectors and the possibility of missing energy in events with total neutral energy higher than this, would mean that some small number of background events are being excluded with this cut, where the possibility exists that these few events could have passed after detector simulation and reconstruction. Nearly all signal events would pass this cut, though in reality the resolution and acceptance of the detector will not be this precise and looser cuts may be required. The effect of the energy cuts cuts on the PYTHIA data set can be seen in Fig. 7.3.

7.1.3 Event Rates

The total hadronic cross-section, σ_t, for the reaction:

$$\gamma p \rightarrow \text{Anything}$$

is known to be about $\sigma_t = 124\mu b$ at $9\,GeV$ [63]. This number is used to set the rates at which GlueX takes data. To better understand the event rates, the $30\,cm$ long liquid hydrogen target in GlueX is examined. The number of target centres per unit area, N_t is:

$$N_t = 12.6 \times 10^{23}\ cm^{-2} = 1.26\ b^{-1}.$$
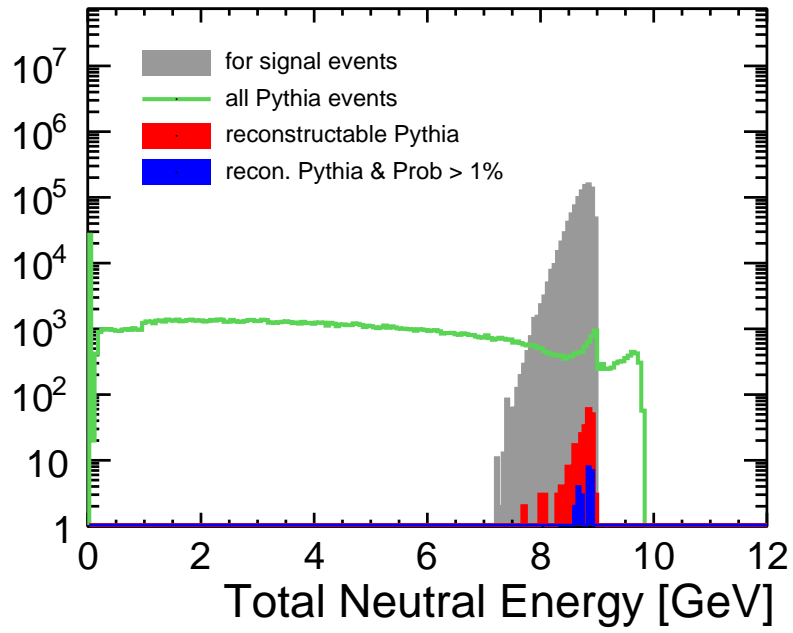
Figure 7.2: The total neutral energy for for all PYTHIA events, signal events, and PYTHIA events which pass reconstruction. The number of events which pass both a cut on charged particle multiplicity and total energy of neutral particles is approximately 4% of the total number of events. Mesons have been decayed to their final states. *(original in colour)*
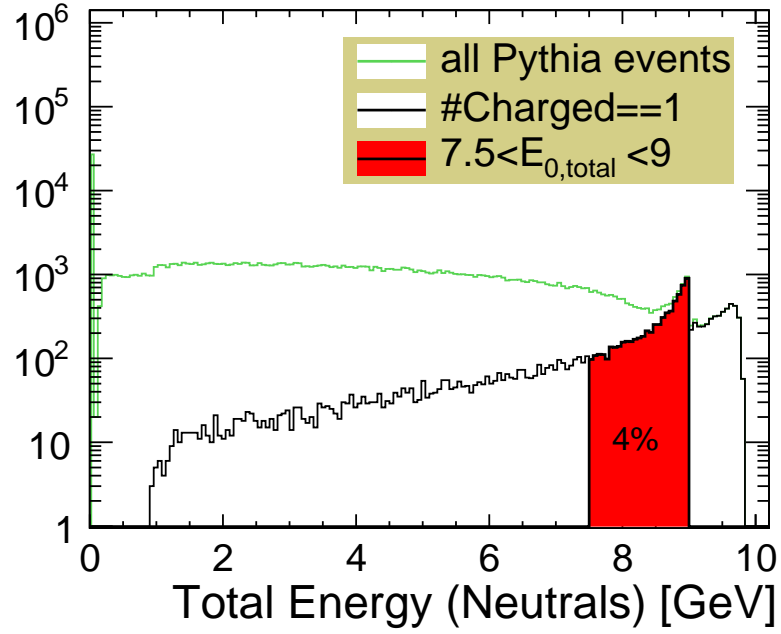
Figure 7.3: The total energy for all neutral particles for all PYTHIA events and PYTHIA events with only 1 charged particle. The solid red region are those events which fall within 7.5 and 9 GeV. *(original in colour)*

Assuming a tagged photon rate, N_γ of:

$$N_\gamma = 1 \times 10^7 \ \gamma/s$$

the event rate can be written as:

$$\begin{aligned}
\mathcal{R} &= \sigma_t \times N_t \times N_{gamma} \\
&= (124 \ \mu b) \times (1.26 \ b^{-1}) \times (10^7 \ s^{-1}) \\
&= 1.55 \ kHz
\end{aligned}$$

This is in agreement with the rates in the GlueX design report [80].

Typically, the estimated cross sections for various resonances of interest in searching for hybrid mesons are on the order of 0.1–3 μb. The photoproduction cross-section for $\eta\pi^0$ is estimated to be 0.8 μb, which will decay to four photons 40% of the time [144]. Taking the upper limit for the photoproduction cross-section of $\gamma p \rightarrow a_2^0(1320)p$ to be 0.4 μb [145], a branching fraction for $a_2(1320)p \rightarrow \eta\pi^0 p$ of 0.14, the upper limit for $\gamma p \rightarrow a_2(1320)p \rightarrow \eta\pi^0 p \rightarrow 4\gamma p$ is 22.5 nb.

Calculating the event rate for $\gamma p \rightarrow a_2(1320)p \rightarrow \eta\pi^0 p \rightarrow 4\gamma p$ in a similar way, gives:

$$\begin{aligned}
\mathcal{R} &= \sigma \times N_t \times N_{gamma} \\
&= (22.5 \times \ 10^{-9} \ b) \times (1.26 \ b^{-1}) \times (10^7 \ s^{-1}) \\
&= 0.284 \ Hz
\end{aligned}$$

Following similar arguments, for $\gamma p \rightarrow \eta\pi^0 \rightarrow 4\gamma$, the expected event rate for

this process is about 4 Hz. These event rates can be used to estimate the equivalent experimental data rates and volumes in order to simulate a realistic data sample.

7.1.4 Data Volume and CPU time

The realities of physics simulations require that enough data storage and time are available in order to analyze a reasonable set of data. Current (easily) available disc space is on the order of a few terabytes and typical CPU clock speeds of 3 GHz allow for only a few events per second to be simulated and analyzed on each computing node. The available quantity of computing resources limit reasonable data volumes to a few hundred gigabytes and a few hundred million events for each data sample. The available resources are expected to grow as reconstruction efforts increase in the collaboration and, more significantly, when experimental data are finally available. With this in mind, the largest background data set to date within the collaboration was created on two separate computing clusters simulating approximately one week's worth of equivalent experimental data. Resources at Indiana University and the OpenScience Grid [146] at the University of Connecticut were used to generate, simulate and store the data used in this chapter.

Table 7.1: Estimated file sizes per event and computer time on the IU cluster. Including log files, the total disc space required is nearly 23 kB per event. Pruning the final HDDM file to remove unneeded hit information reduces this down to 30 to 40% of the original size (7 to 10 kB/event).

Software file	kByte/event	CPU time
bggen.hddm (PYTHIA input)	0.81	negligible
hdgeant.hddm detector MC output	21.7	~ 1.2 sec/event
analysis.root reconstruction	0.33	~ 0.015 sec/event

The software packages used in the production and analysis of the data produces data files of sizes listed in Table 7.1. Since the HDDM file output by HDGEANT

Table 7.2: Expected event rates for various reactions from photo-production for a $10^7 \gamma/\text{s}$ photon beam . The σ column is the estimated cross section. A beam rate of $10^8 \gamma/s$ will increase the magnitudes of the number of events and data volumes by one order.

reaction	σ	number of events		
		day^{-1}	week^{-1}	$\text{year}(10^7\text{s})^{-1}$
$\gamma p \rightarrow$ anything	$124\,\mu\text{b}$	1.34×10^8	9.37×10^8	1.55×10^{10}
$\gamma p \rightarrow \eta\pi^0 p$	$0.80\,\mu\text{b}$	3.46×10^5	2.42×10^6	4.0×10^7
$\gamma p \rightarrow a_2(1320)p \rightarrow \eta\pi^0 p \rightarrow 4\gamma$	22.5 nb	2.45×10^4	1.72×10^5	2.84×10^6

Table 7.3: Expected data volumes for example reactions for a $10^7\gamma$/s photon beam. Filtering of the data is removing 96% of the original data volume by event selection. Pruning reduces the data to 40% of the original volume.

reaction	MC data record size (GB)		
	day^{-1}	week^{-1}	year^{-1}
$\gamma p \to$ anything	4.37×10^3	2.16×10^4	3.57×10^5
(filtered and pruned)	6.99×10^1	3.46×10^2	5.71×10^3
$\gamma p \to \eta\pi^0 p$	7.96	55.7	920
(pruned)	3.18	22.3	368
$\gamma p \to a_2(1320) \to \eta\pi^0 p \to 4\gamma$	0.56	3.95	65.4
(pruned)	0.23	1.58	26.1

contains all the hit information of all the detectors within the simulation, it is possible to prune off the information not required for reconstructing our specific event afterwards, such as hits in the charged particle tracking detectors. A new HDDM template was defined which contains only FCAL and BCAL hit information after the detector simulation and the original generator-level information for each event. This has the effect of reducing the file size by 60 to 70% and reducing the overall disc space requirements from 23 kB/event to 7 to 10 kB/event, depending on the volume of hit information from each detector.

The expected event rates and associated data volumes for background and a_2^0 signal Monte Carlo are shown in Table 7.2. The volumes for a PYTHIA data set are shown for before and after removing unnecessary events and data records. With the expected data volumes and event rates shown in Tables 7.1, 7.2 and 7.3, and available computing resources, it was reasonable to produce only a few days worth of equivalent experimental data.

7.2 Kinematic Fitting

The kinematic fitter used in GLUEX is derived from the fitter used in the CLAS experiment [147]. The fitting process uses Lagrangian multipliers to handle the physical constraints, energy-momentum conservation in this case, and the fitting is done using the method of least squares. The full method is thoroughly presented by the CLAS collaboration in [147].

The fitter is an iterative process where the algorithm minimizes a quantity $\vec{\delta}^T C^{-1} \vec{\delta}$ where $\vec{\delta}$ is the matrix of least square estimates of the deviations, $\vec{\delta}^T$ is its transpose and C is the covariance matrix which describes the errors in the measurement. This is also referred to as the total error matrix. The errors in the detectors must be

understood very well in order to reconstruct the covariance matrix properly, since it is in turn constructed from error matrices of the reconstructed particles. The error matrices for the reconstructed particles are constructed from MC and beam test information and are a result of physical processes, such as sampling fluctuations in the barrel calorimeter and photo-statistics.

The least squares measurement error estimates can be described by the vector

$$\vec{\epsilon} = \vec{\eta} - \vec{y} \tag{7.2}$$

where $\vec{y}$ are the improved measurements from the final iteration of the minimization algorithm and $\vec{\eta}$ are the measured values. In the case where $\vec{\eta}$ are independent measurements, the quantity $\vec{\delta}^T C^{-1} \vec{\delta}$ becomes $\sum_{j=1}^{n} \frac{\epsilon_j^2}{\sigma(\epsilon_j)^2}$ for n measurements.

7.2.1 Probability and Pull Distributions

After the final iteration of the fit, the goodness of the fit, or the agreement between data and the hypothesis, can be determined from the confidence level or "Probability" and "Pull" distributions.

7.2.1.1 Probability

The probability that the values from the fit are a good representation of the data can be expressed as

$$\wp = Probability = \int_{\chi^2}^{\infty} f(z; n) dz \tag{7.3}$$

where $f(z; n)$ is the χ^2 probability density function with n degrees of freedom, where errors are assumed to be normally distributed. This is the probability that a χ^2 from the theoretical distribution is greater than the χ^2 from the fit.

In the absence of background, and with a detector with perfect acceptance, $\wp$ follows a flat distribution from 0 to 1. Events that do not satisfy the hypothesized constraint equations produce a sharp rise near $\wp = 0$. In the case of this work, the sum of the final four-momenta must be equal to the sum of the initial beam and target four-momenta with additional constraints on the η and π^0 masses. The kinematic fit constraints are in addition to the requirements on the number of charged particles and photons needed for event reconstruction. Cutting out events with low $\wp$ provides a good way of removing background in a controlled and understandable way. However, complications can arise from poor acceptance of signal events in certain regions of the detector, where signal events will no longer fit the hypothesis.

7.2.1.2   Pull

To effectively use $\wp$ to remove background, a good understanding of the errors in each fit quantity is needed, otherwise a non-flat probability distribution will be produced. The quantity that describes how far the improved measurement is stretched from the true measured value for the i'th value or "Pull" is defined as

$$Pull = z_i = \frac{\eta_i - y_i}{\sqrt{\sigma_{\eta_i}^2 - \sigma_{y_i}^2}} \tag{7.4}$$

where η_i is initial measured value of a parameter and y_i is the final "true" value after adjustment by the kinematic fitter, with errors σ_{η_i} and σ_{y_i}. If the error for the i'th measured value is described properly, z_i should be normally distributed about zero with $\sigma = 1$. A systematic error in one of the measured quantities, η_i, can be seen as an overall shift in the distribution of the corresponding *Pull* (z_i) away from zero. Similarly, if σ_{η_i} is consistently overestimated (underestimated), the *Pull* distribution will be too narrow (wide). Hence, the *Pull* distribution can give a good indication

of how well the uncertainties in the reconstruction have been determined.

7.3 Reconstruction of the $\eta\pi^0$ System

Channels that decay purely into photons are expected to be challenging to identify and may be difficult to cleanly separate from the background. In what follows, the focus is on the efficiency for reconstructing an all neutral signal and the anticipated background from other hadronic events. Again, the tuned version of PYTHIA is used to reproduce the known photoproduction cross sections of charged and neutral particles. To ensure that the data set originates from pure background hadronic photoproduction processes, the identities of the particles provided by PYTHIA are examined and events that match the exclusive signal topology are excluded. Meson decays are done within HDGEANT rather than PYTHIA for simplicity. The AMP-TOOLS generator is then used to generate pure signal events. Of particular interest is the ratio of signal to background efficiency, which is key to estimating the sensitivity to a particular physics channel. The analysis is not meant to perfectly describe the background and signal, but is meant to be the first exploration of the challenges of reconstructing all-neutral events in the GLUEX spectrometer. For this reason, a flat distribution for the $\eta\pi^0$ invariant mass was chosen.

A relatively simple two-body channel such as $\gamma p \rightarrow Xp \rightarrow \eta\pi^0 p \rightarrow 4\gamma p$ was examined, where X is some resonance, as it is a multi-neutral final state and there is some expectation that hybrids may decay through this channel. The resonance mass was given a flat distribution from 0.7 to 2.2 GeV/c^2, since it is expected that hybrids will be found in this mass range. The ability to reconstruct multi-neutral events will be important for studying conventional mesons produced through photoproduction as well as for discovering hybrid mesons.

An important aspect of partial wave analysis is the need for good acceptance in phase-space in order to be able to separate hybrid waves from conventional mesons. The expected momentum versus polar angle distributions for the photons are shown in Fig. 7.4 in the top plot. These are similar to the PYTHIA distributions shown earlier, though more of the photons are in the region intercepted by the FCAL. The gap in the efficiency can be seen near 10 degrees in the bottom plot. However, the gap covers a small part of phase-space, and therefore is not overly worrying.

Fig. 7.5 shows the multiplicity of reconstructed photons in both the FCAL and BCAL calorimeters from a sample of 350,000 signal events and 220 million background events. The signal photon cluster multiplicity appears as expected, with some number of extra clusters seen due to split-offs or conversion before the calorimeters. However, the PYTHIA photon multiplicity shows very many more clusters than what is expected (Fig. 7.6). Meetings with other members of the collaboration, who are also studying reconstruction of physics events, have concluded that charged particles in the calorimeter create many split-off or spurious clusters that are not currently being associated with the charged particles and, thus, cannot be suppressed. Hadronic interactions in the BCAL appear to create many other charged particles that curl out of the BCAL in the solenoid field and create additional clusters separate from the central one created by the incident particle. Algorithms from previous experiments are currently being explored to deal with this, as these extra clusters present a significant problem.

Signal $\eta\pi^0$ candidates are selected by requiring that there be at least four clusters in the BCAL or FCAL, not associated with charged particles, and one positively charged particle with a mass near that of the proton. The charged particle multiplicty and mass should be extractable from the PID system (CDC, FDC and TOF)
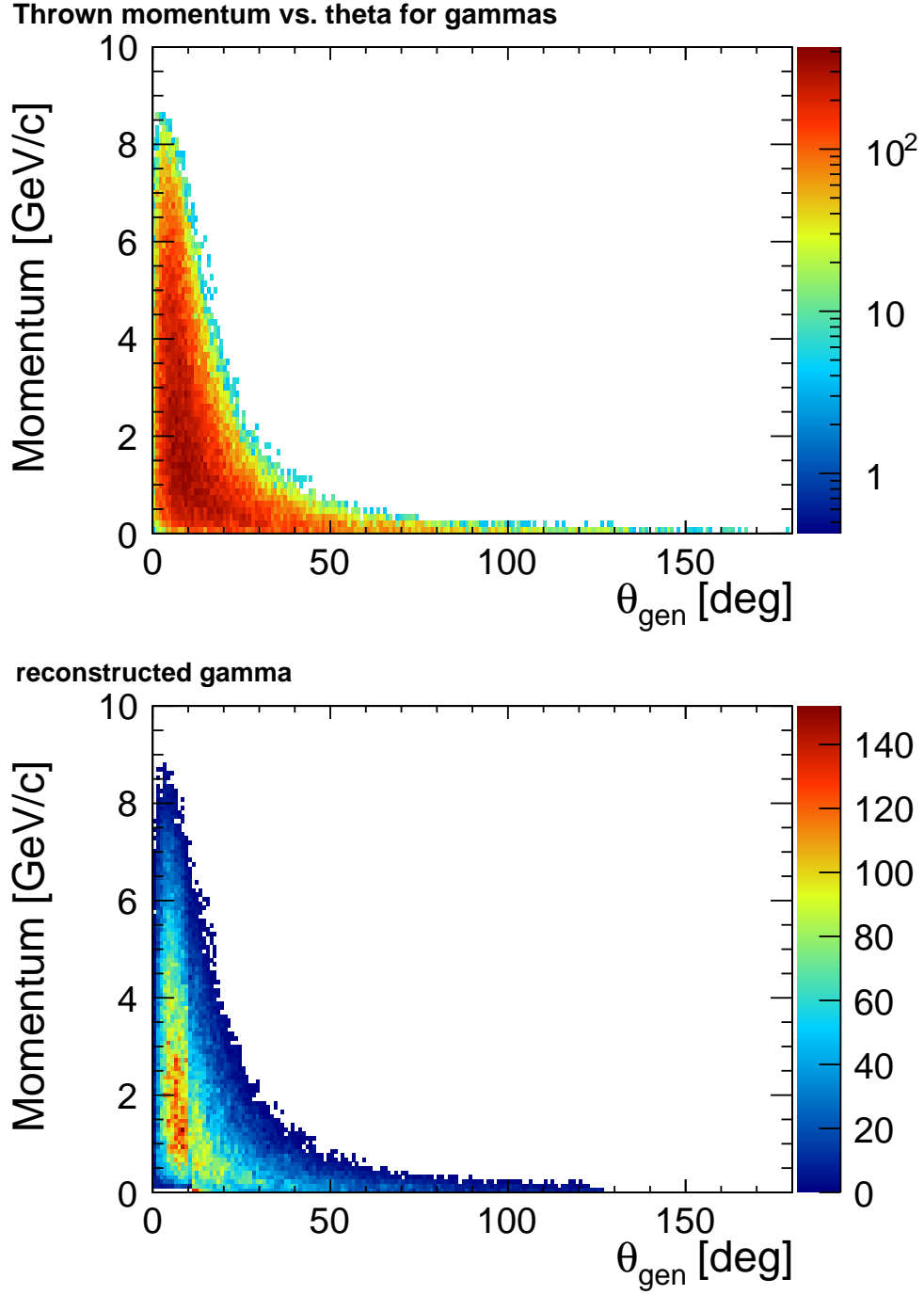
Figure 7.4: The momentum versus polar angle distribution for photons from $\eta\pi^0$ decays. Thrown events are shown on top and reconstructed events are shown on the bottom with a linear scale to show the gap in efficiency at $\theta_{gen} = 10^0$ more clearly. *(original in colour)*
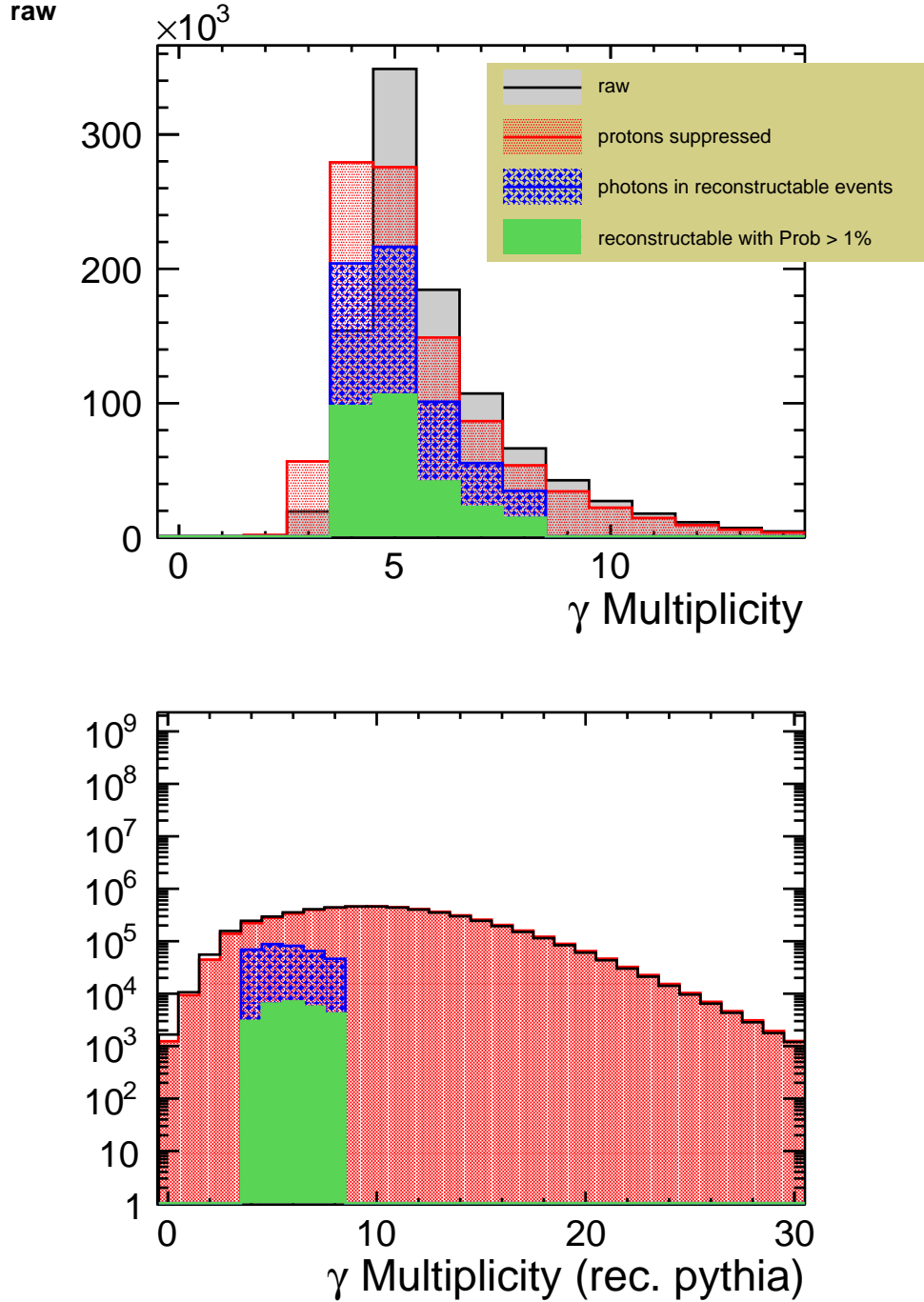
Figure 7.5: Photon multiplicity for reconstructed $\eta\pi^0$ signal (top) and background (bottom) events. The plots show the raw reconstructed photon multiplicty, and the multiplicity after clusters due to charged particles are suppressed. Multiplicity of photons for any reconstructible event and events which pass a probability cut of greater than 1% are shown in the figure. *(original in colour)*
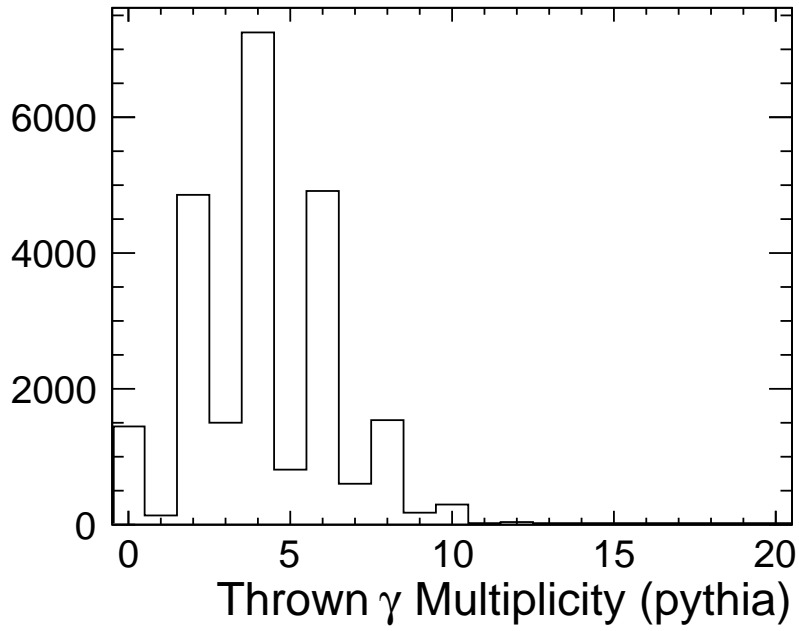
Figure 7.6: Expected photon multiplicity for filtered background events. Photons from π^0, η and neutral kaon decays are included in the histogram. The distribution is drastically different than what is seen in Fig. 7.5. The larger number of even multiplicity events are from meson decays to 2γ. It should be noted that the number of events in the sample examined for this plot is much smaller than in Fig. 7.5.

in experiment, but this work used smeared generator information from HDParSim. The photons in each event are looped over and a kinematic fit is applied to four of the calorimeter clusters (photons) with constraints on the η and π^0 masses, and total initial and final four-momenta. The calorimeter clusters are presumed to be photon showers after suppressing the clusters from charged particles. The clusters are reconstructed using the full Hall-D reconstruction software package. The number of possible candidates for the signal reaction are seen in Fig. 7.7, where a candidate has at least four calorimeter clusters, one proton and a fit probability greater than 1%. Proton momentum smearing, acceptance and error matricies are handled by the parametric Monte Carlo, HDParSim. The fit with the highest probability from the kinematic fitter is chosen as the primary candidate.

The reconstructed four-photon invariant mass is shown in Fig. 7.8 for signal events and Fig. 7.9 for background events. 2.2×10^8 PYTHIA events and 142,000 signal events were simulated for a relative cross section ratio of 124μb:80nb. On average, the reconstruction efficiency for $\eta \pi^0$ signal events before any probability cut is 60%. A cut on the kinematic fit probability for events less than 1% reduces the reconstruction efficiency for signal events to 45%.

The signal to background ratio for all reconstructible events with a kinematic fit probability greater than 1% is shown in Fig. 7.10. For partial wave analysis, the desired ratio is on the order of 10 to one or better. Currently, however, for a flat $\eta \pi^0$ distribution, the ratio is much lower at 3 to 1. The is due to the large number of background events which pass the probability cut, as seen in Fig. 7.11. All $\eta \pi^0 p$ events have been removed from the PYTHIA data set, so no event should match the hypothesis very well. The high kinematic fit probability is most likely due to cluster misidentification, missing or extra clusters and just poor resolution for some photons.
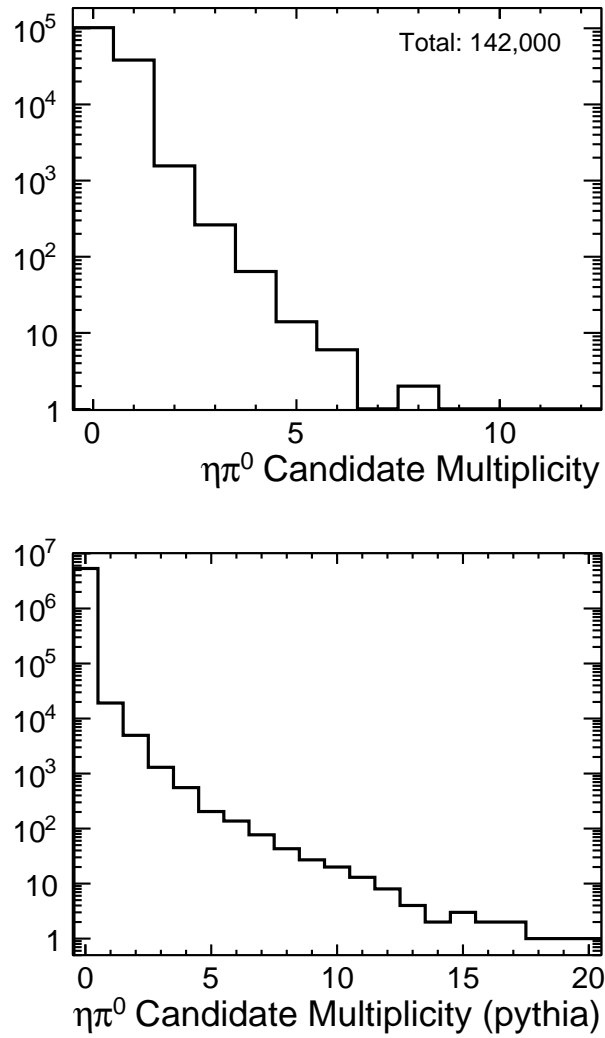
Figure 7.7: The candidate multiplicity for 142,000 generated signal events (top) and 700,000 background PYTHIA events (bottom) after reconstruction requirements are applied.
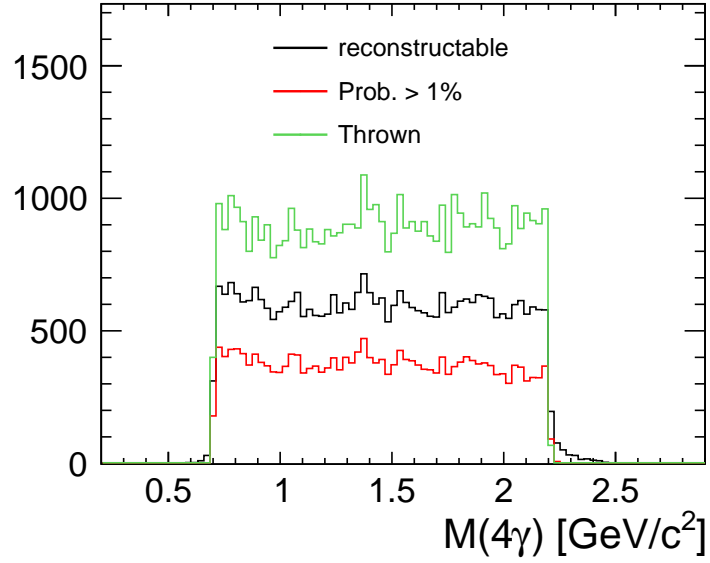
Figure 7.8: The reconstructed 4-photon invariant mass for a flat $\eta\pi^0$ distribution for signal events (top) and background (bottom). The green data are all generated signal events. Black are all events that meet the reconstruction requirements and the red data are the reconstructible data after applying a 1% probability cut. *(original in colour)*
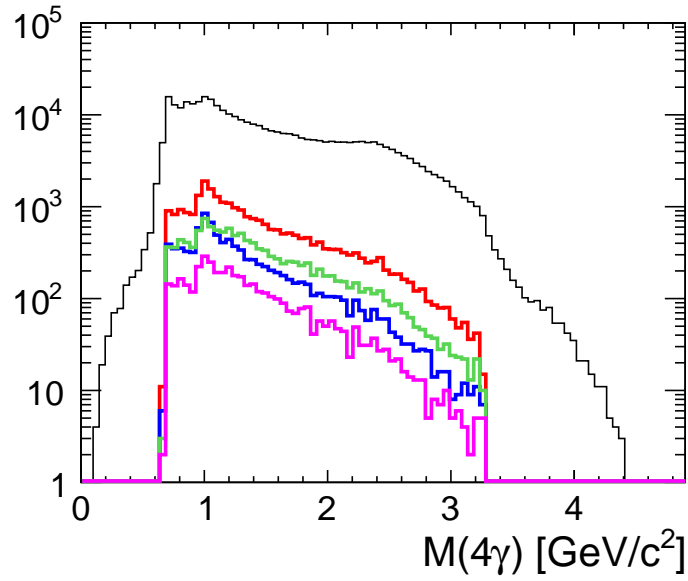
Figure 7.9: The reconstructed 4-photon invariant mass for a flat $\eta\pi^0$ distribution for background pythia events. The black data are all events which meet the reconstruction requirements. The red data are reconstructible events which pass the 1% probability cut. The blue data are events which pass a 10% probability cut. The green data are events which pass a 1% probability cut with less than six good photon clusters. The magenta data are events which pass a 10% probability cut with less than six good photon clusters. *(original in colour)*

This is not certain and will require a more careful examinition of the clusters in each event but will be left for future work. The number of clusters due to photons in the background should be quite low, but the large number of misidentified clusters are included in the reconstruction and pass as possible $\eta\pi^0$ candidates. Development of a better algorithm to exclude these clusters should improve the background to signal ratio. Also, real physics resonances will have peaks in the invariant mass distribution and will rise above the backgorund, therefore an improved signal to noise ratio should be seen.
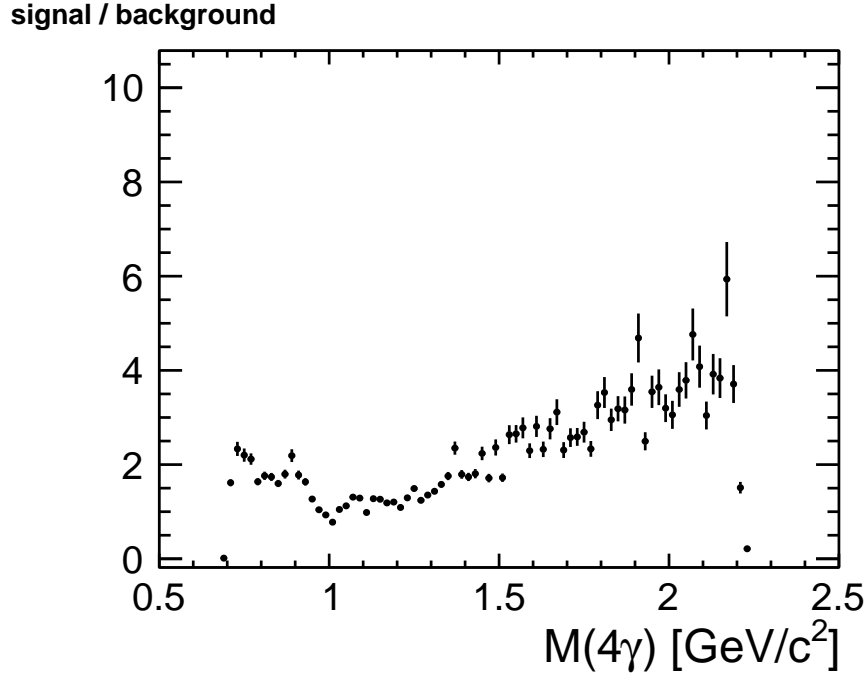
Figure 7.10: The ratio of signal to background events as a function of invariant mass.

7.3.1   Background reactions

An examination of the background events that are mistaken for $p\eta\pi^0$ and pass the reconstruction criteria with a kinematic fit probability greater than 1% are: $p\pi^0$, $p\eta$,
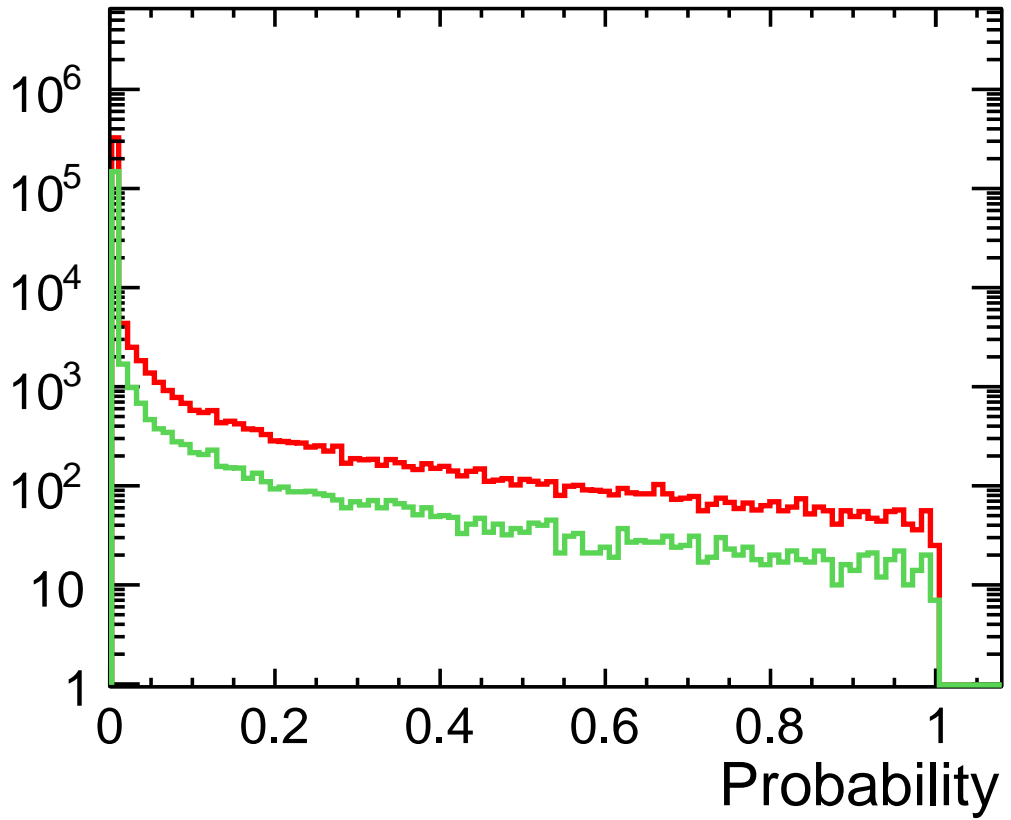
Figure 7.11: The kinematic fit probability for simulated PYTHIA events. The red data are all events which pass the reconstructon criteria. The green data are all events which pass the reconstruction criteria but with with less than six clusters.

$p\eta\pi^0\pi^0$, $p\pi^0\pi^0\pi^0$, $p\pi^0\pi^0$, and other similar all neutral decays where there is a good chance that a cluster is missed, or conversions and split-off showers contribute to extra clusters in the calorimeters. Of the 4% of PYTHIA events that pass the initial neutral energy and charged particle multiplicty cuts, 0.6% of the filtered events pass a cut on the kinematic fit probability of 1%. This means, as a fraction of the inital 124 μb cross-section, the cross-section of events which are reconstructed with good probability of being $\eta\pi^0$ have an equivalent cross-section to the signal, $\sim$29 nb.

Background events typically excluded by the reconstruction requirements or kinematic fit include $n\pi^+\pi^0$, $n\eta\pi^+\pi^0$, nK^+K_L, pK_LK_S. Events with neutral kaons in an intermediate state are generally excluded because K_L typically decays to semileptonic modes with charged pions and leptons in the final state with a branching fraction of $\sim 70\%$, but will decay to an all neutral $3\pi^0$ $\sim$20% of the time. K_S will typically decay to two pions, $\pi^0\pi^0$ (31%) or $\pi^+\pi^-$ (60%). The requirement for only one positively charged particle with a mass near the proton mass (this information should be extractable from PID in the experiment) will exclude most events with a kaon as well as events with a neutron and a π^+ or K^+.

7.3.2 Pulls and Probability

The probability distribution for reconstructing only signal events can be seen in Fig. 7.12. For a perfect detector, the distribution should be flat from zero to one. However, efficiency, photon conversions and cluster split-offs contribute to events which are poorly reconstructed and have a very low kinematic fit probability. Fig. 7.12 shows a large fraction of the events with a probability less than 1% and a non-flat distribution afterwards with a slight peak near one. A plot of probability versus invariant mass, Fig. 7.13, shows that the skewed probability has a peak near

one for larger invariant mass. This may indicate a relationship between the ability to identify photon showers and the invariant mass of a resonant decay.

Fig 7.11 shows the kinematic fit probability for purely background events that pass the reconstruction criteria. It is suspected that events with a large probability of matching the $\eta\pi^0$ hypothesis also suffer from problems with photon conversions and cluster split-offs. An event by event examination of the background shows that many of these events have a neutral particle multiplicity differerent from that of the signal.
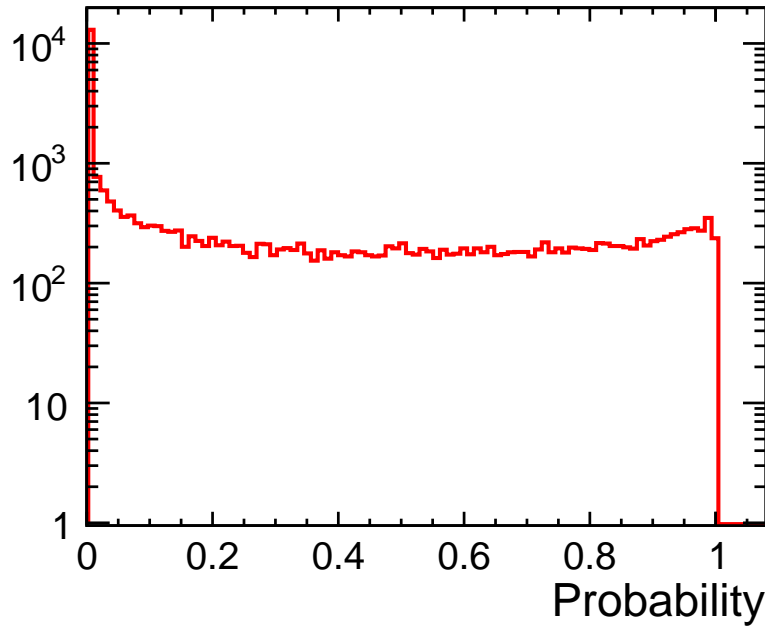
Figure 7.12: The kinematic fit probability for reconstructed $\eta\pi^0$ decays.

An examination of the three *Pull* distributions for the momenta, z_{p_x}, z_{p_y}, z_{p_z}, of each photon, should give an indication of whether the uncertainties in the calorimeters are determined properly and are possibly having an effect on the kinematic fit. From Eq. 7.4, the distributions should have a standard deviation of one, where larger
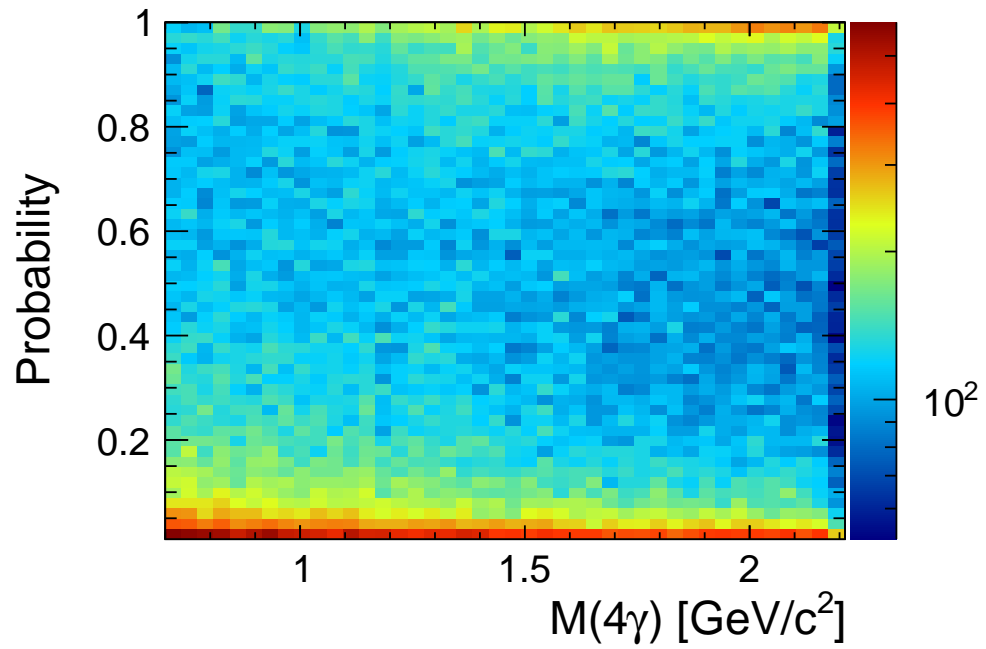
Figure 7.13: The kinematic fit probability versus 4γ invariant mass for reconstructed $\eta\pi^0$ decays. Notice the larger number of events with probability near one for larger invariant mass. *(original in colour)*

(smaller) values indicate an under (over)-estimation of the uncertainties. Fig. 7.14 shows the *Pull* distributions for one of the photons in the $\eta\pi^0$ signal reconstruction. A cut on polar angle was applied to divide the data into three regions: photons that enter only the FCAL ($\theta < 9°$), photons that enter only the BCAL ($\theta > 11°$) and photons that strike the near the gap in polar angle acceptance between the FCAL and BCAL ($9° < \theta < 11°$) , where it is suspected that the errors are not modeled correctly. As well, the energy resolution of the BCAL is not modeled with any dependence on position, only a dependence on energy. The mean and standard deviation, σ, of each *Pull* distribution was determined by fitting the data with a Gaussian function, and are shown in Table 7.4.

Table 7.4: The means, $\bar{z}_i$, and standard deviations, σ_{z_i} for photon momenta *Pull* distributions. These are determined by fitting the data to a Gaussian function, where the fits are shown in Fig. 7.14. A *Pull* distribution is expected to be centered around zero with a standard deviation of one if the errors are modeled correctly.

	$\bar{z}_{p_x}$	$\sigma_{z_{p_x}}$	$\bar{z}_{p_y}$	$\sigma_{z_{p_x}}$	$\bar{z}_{p_z}$	$\sigma_{z_{p_x}}$
BCAL	0.00±0.01	0.95±0.01	0.07±0.02	1.04±0.01	-0.02±0.01	0.97±0.01
FCAL	0.02± 0.01	0.98±0.01	0.15±0.01	1.22±0.01	0.00±0.01	1.00 ±0.01
Gap	-0.04±0.02	1.01±0.02	0.22±0.03	1.22±0.02	-0.03±0.02	1.00 ±0.02

The p_x and p_z *Pull* distributions for the BCAL and FCAL, including the gap region, both show a mean near zero, with standard devations near one, indicating that the errors for photons have been modeled correctly in the Monte Carlo. However, the p_y *Pull* distribution displays a significant shift from zero, as well as a standard deviation greater than one, indicating that there is a systematic error in this uncertainty, as well as an underestimation of the size of this uncertainty. This effect is small for the BCAL, but is quite significant for the FCAL and in the gap region and should be studied further to correct this. As a result of the cylindrical symmetry of the GLUEX detector, this underestimation of the uncertainy in p_x is most likely in

the transverse momentum error. However, the fact that z_{p_x} is centered around zero with a σ near one, would indicate that this is not certain and other causes for the shift and extra width should be looked for.

7.4   Future work

The large multiplicity of showers in the background, as well as excess showers in the signal, indicate problems in the reconstruction software where it is most likely that minor clusters are being identified as separate from their primary cluster. Some extra clusters are expected due to conversions before the calorimeters but it seems a disproportionate number are being created in the backgound. As alluded to by the data, the code is not yet suitable to handle split-offs and conversions resulting in event-set contamination. This problem warrants further investigation of how clusters are merged or associated with charged particles. As well, the uncertainties associated with the detectors must be examined further, as the kinematic fitter pulls indicate an underestimation of the uncertainties and a systematic shift in the value for z_{p_x}.

To this end, a large-scale effort is commencing within the GLUEX collaboration to implement additional algorithms within the code to properly handle split-off clusters as well as examine the reconstruction software for other innefficiencies or deficiencies and try to find solutions for these.
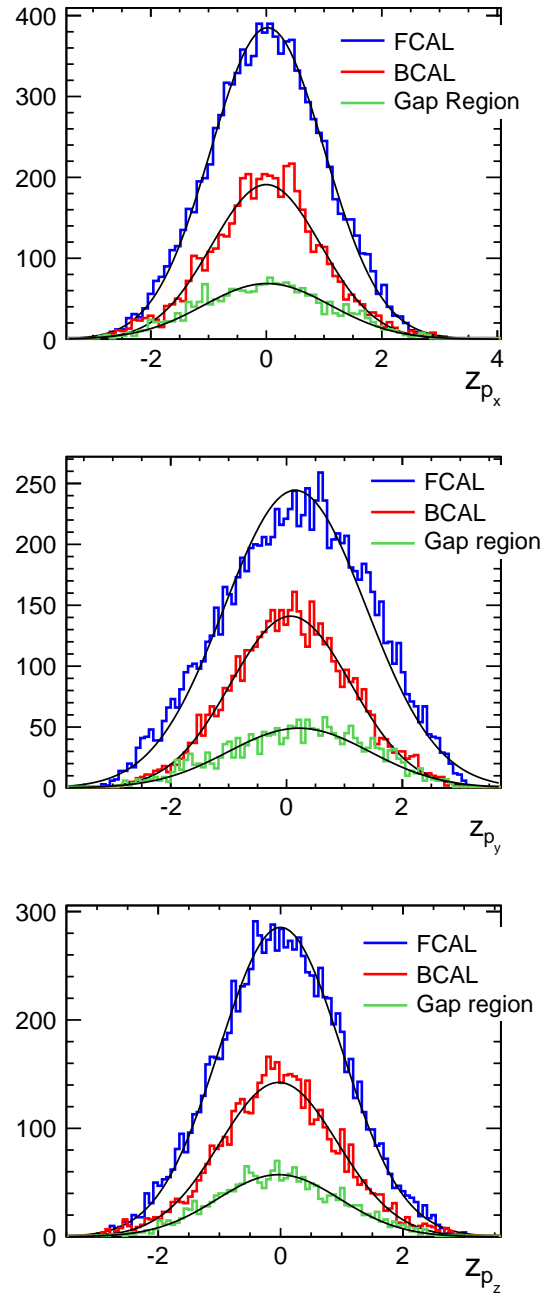
Figure 7.14: The three pull distributions for momentum for a single photon for the BCAL ($\theta > 11°$), FCAL ($\theta < 9°$) and the gap near polar angle acceptance ($9° < \theta < 11°$). The distributions should be centered around zero with a σ of 1 if the measurement errors are determined properly. The fits to the data are Gaussian functions (black lines). The mean and standard deviation of each fit is shown in Table 7.4. *(original in colour)*

Chapter 8

Conclusions

Over the course of this work, many aspects of the BCAL have been examined as a vanguard effort for the GLUEX collaboration in many areas.

As a result of the photon beam test at Jefferson Lab in Hall-B, the energy resolution at the centre of a single module was determined to be

$$\frac{\sigma_E}{E} = \frac{5.4\%}{\sqrt{E(\text{GeV})}} \oplus 2.3\% \ ,$$

with a time difference resolution of

$$\sigma_{\Delta T/2,7-10} = \frac{75 \text{ ps}}{\sqrt{E(\text{GeV})}} \oplus 30 \text{ ps.}$$

This timing resolution results in a position resolution of $\sigma_z = 1.1 \text{ cm}/\sqrt{E(\text{GeV})}$ for a 1 GeV photon. The beam test also yielded a mean value of $\sim$660 photoelectrons per GeV for photons over the energy range of the beam test. These results are very similar to those seen in the KLOE experiment for a similarly designed calorimeter.

Monte Carlo simulations of the single calorimeter prototype module extracted a sampling fraction of 12.5% for the prototype calorimeter module with an expected

contribution to the energy resolution from the sampling fluctuations of $4.6\%/\sqrt{E} \oplus$ 1.6%. The rest of the energy resolution is expected to be from from photoelectron statistics.

The two types of fibres measured in this thesis showed similar bulk attenuation lengths of 428 ± 23 cm (PHT-044 blue) and 400 ± 23 cm (BCF-20 green) when measured with a photo-spectrometer. The quantum efficiency for a traditional vaccuum PMT is greater in the blue part of the optical spectrum and poor in the green region. On the other hand, the quantum efficiency of the silicon photomultiplier is not strongly dependent upon wavelength. For this reason, and the greater attenuation of the shorter wavelengths of light in the fibre, the blue PHT-044 fibres exhibit a shorter bulk attenuation length when coupled to either photo-detector. However, even when coupling the PHT-044 to a PMT, the expected attenuation length of 353 ± 18 cm still exceeds the design requirements for the BCAL of attenuation length greater than 300 cm. Coupling the green BCF-20 fibres to a silicon photomultiplier results in an expected attenuation length of 408 ± 25 cm.

The light-guide design presented in this thesis relies only on total internal reflection and the appropriate choice of surfaces that maximize collection and transport efficiency with an area reduction by a factor of $\sim$3. The efficiency is near 90% assuming that a non-air gap coupling is chosen at the calorimeter face and the readout face. An air gap would result in nearly 30% of the light being total internally reflected back away from the light sensor.

Using the parameters measured above, the BCAL in the full HDGEANT detector simulation was encoded to return realistic fluctuations in the measured energy with expected contributions from readout-electronics noise. The calibration of the detector in the MC was then performed to return corrected energies after reconstruction for

single clusters from photons thrown at the BCAL. Any modification to materials or the readout geometry will require a recalibration of the detector in the MC. Special attention was paid to the last few cm's of the module as this is a problem region of the BCAL due to its shorter number of effective radiation lengths in thickness. Some corrections can be made, but this region of the BCAL has very poor resolution and acceptance. This region lies in the centre of the phase space populated by the physics reactions of interest to GLUEX, though, fortunately, occupies only a small region of phase space for the key reactions examined.

Examination of the position resolution, σ_z, from the HDGEANT detector simulation, indicated a z-dependence with σ_z increasing from 1 cm near the target up to 1.5 cm near the downstream end of the module. An offset in the position difference from thrown information indicates that a correction to the shower position in the reconstruction algorithm is also required. The polar angle resolution was observed to be ~10 mrad near the target and improved quickly to 1 mrad near the downstream end. The azimuthal resolution was determined to be about 5 mrad for the majority of the length of the BCAL module and degraded by a factor of 2-3 over the last few cm's of the calorimeter.

Efficiency studies for reconstructing single photon showers clearly illustrate the gap in acceptance between the FCAL and BCAL at 10.5°. The charged particle tracking detectors and other material between the target and calorimeters indicate a conversion rate of up to 40% in some regions of polar angle. Further studies will be needed to determine whether it is possible to properly reconstruct these showers.

Previous to the final determination of the readout configuration, a 6×4 SiPM and a 3×3 FM PMT configuration were compared, and showed similar energy resolutions. However, the 6×4 configuration showed better polar and azimuthal resolutions at

higher photon energy and downstream positions. This is attributed to the granularity of the readout and the sampling fluctuations.

In a first attempt within the collaboration to reconstruct a large signal data set and to determine the associated background to the signal, many technical hurdles were overcome and some deficiencies in the reconstruction code were found. An experimental equivalent of one week's worth of data was produced with the background simulation and reconstruction being the largest portion of the data volume. An all-neutral signal was chosen to illustrate the performance of the calorimeters. However, in order to match clusters from charged particle to charged particle tracks, the tracking packages were also needed. By examining the signal and background events which pass and fail reconstruction, a set of data cuts was developed to improve the signal to background signal in conjunction with the kinematic fitter.

It also became apparent in reconstructing the background that events that pass reconstruction have true photon multiplicities different than the signal photon multiplicity. Most of the events which pass the backgrounds cuts and reconstruction have a single recoil proton with neutral meson decays. This indicates that conversions, split-offs and detector acceptance are contributing to the signal background. More work will be needed to examine these events on an individual basis to find the reasons they are passing reconstruction and kinematic fitter probability cuts.

In conclusion, this thesis presents a comprehensive look at most of the crucial elements of the BCAL, from expected resolutions to reconstruction of events and the harbinger study of signal to noise background. The areas of software development, reconstruction and analysis is expected to be further developed by the collaboration for the next few years until data-taking begins in 2014.

<p align="center">The End.</p>

Appendix A

GEANT Input Card

This input card sets some of the parameters for the HDGEANT simulation.

```
C This is the control file for the GEANT simulation.  Parameters defined
C in this file control the kind and extent of simulation that is performed.
C The full list of options is given in section BASE-40 of the GEANT manual.
C
C In addition, some new cards have been defined to set up the input source
C for the simulation.  Three kinds of simulation runs are available, selected
C by which of the following three "cards" are present below.
C    1. Input from Monte Carlo generator (card INFILE)
C    2. Built-in coherent bremsstrahlung source (card BEAM)
C    3. Built-in single-track event generator (card KINE)
C The order of the list is significant, that is if INFILE is present then the
C BEAM and KINE cards are ignored, otherwise if BEAM is present then KINE is
C ignored.  For example, the 3-card sequence:
INFILE 'output.hddm'
C SKIP 5000
C    TRIG 100
C instructs HDGeant to open *.hddm, skip the first 5000 events and then
C process the following 100 input events and stop.  If the end of the file is
C reached before the event count specified in card TRIG is exhausted then the
C processing will stop at the end of file.

TRIG 5000
```

```
BEAM 12. 9.
C RUNG 1


OUTFILE '/home/fs1/leverin/etapi0flat/hdgeant_001/hdgeant_001.hddm'


C The following card enables single-track generation (for testing)
c    particle  momentum  theta  phi  delta_momentum delta_theta delta_phi


KINE    101     2.0   ANGLE   0.      4.0      RANGE       360.
SCAP    0.      0.      65.


c The following lines control the rate (GHz) of background beam photons
c that are overlayed on each event in the simulation, in addition to the
c particles produced by the standard generation mechanism.  A value of
c 1.10 corresponds to nominal GlueX running conditions at an intensity of
c 10^7 tagged photons on target per second.  To disable the generation of
c random beam background, comment this line out or set the value of BGRATE
c to zero.  Background beam photons are generated during the time interval
c given by the BGGATE card, whose two arguments specify the earliest and
c latest times (ns relative to the time of the original photon that caused
c the event) that a random beam photon could produce background hits
c somewhere in the detector.  Note that for this to work, the BEAM card
c must be present (see above).  This means that background generation is
c disabled when the simulation operates in particle gun mode.
c If Emin is set in the BEAM card (see above), the rate of background photons
c is automatically rescaled as follows:
c        Rate(E_gamma > Thr)  =  Rate(E_gamma = 0.12 Gev) * K,
c where K is a scale factor calculated inside uginit.F:
c        K = 1 for Thr = 0.12 GeV,
c        K > 1 for Thr < 0.12 GeV.
c Note, K is calculated assuming the beam energies Emax = 12, Epeak = 9.
cBGRATE 0.
 BGRATE 1.10
BGGATE -200. 200.


C The following card seeds the random number generator so it must be unique
C for each run.  There are two ways to specify the random see for a run.
C  1. One argument, must be an integer in the range [1,215]
C  2. Two arguments, must be a pair of positive Integer*4 numbers
```

```
C In the first case, one of a limited set of prepared starting seeds is
C chosen from a list.  These seeds have been certified to produce random
C sequences that do not repeat within the first 10^9 or so random numbers.
C For cases where more choices are needed, the two-argument form gives
C access to a total of 2^62 choices, with no guarantees about closed loops.
RNDM 1


c The following line controls the cutoffs for tracking of particles.
c CUTS cutgam cutele cutneu cuthad cutmuo bcute bcutm dcute dcutm ppcutm tofmax
c  - cutgam = Cut for gammas (0.001 GeV)
c  - cutele = Cut for electrons (0.001 GeV)
c  - cutneu = Cut for neutral hadrons (0.01 GeV)
c  - cuthad = Cut for charged hadrons (0.01 GeV)
c  - cutmuo = Cut for muons (0.01 GeV)
c  - bcute  = Cut for electron brems. (CUTGAM)
c  - bcutm  = Cut for muon brems. (CUTGAM)
c  - dcute  = Cut for electron delta-rays. (10 TeV)
c  - dcutm  = Cut for muon delta-rays. (10 TeV)
c  - ppcutm = Cut for e+e- pairs by muons. (0.01 GeV)
c  - tofmax = Time of flight cut (1.E+10 sec)
c  - gcuts  = 5 user words (0.)
CUTS 1e-5 1e-5 1e-4 1e-4 1e-4


c The following line controls a set of generic flags that are used to
c control aspects of the simulation generally related to debugging.
c For normal debugging runs these should be left at zero (or omitted).
c At present the following functionality is defined (assumes debug on).
c  SWIT(2) = 0 turns off trajectory tracing
c          = 2 turns on step-by-step trace during tracking (verbose!)
c          = 3 turns on trajectory plotting after tracking is done
c          = 4 turns on step-by-step plotting during tracking
c  SWIT(3) = 1 stores track trajectories for plotting after tracking is done
c  SWIT(4) = 0 trace trajectories of all particle types
c          = 3 trace only charged particle trajectories
SWIT 0 0 0 0 0 0 0 0 0 0


C The following card enables the GelHad package (from BaBar)
C   on/off  ecut   scale   mode   thresh
GELH  1     0.2     1.0     4      0.160
```

```
c The following card selects the hadronic physics package

c    HADR 0      no hadronic interactions

c    HADR 1      GHEISHA only (default)

c    HADR 2      GHEISHA only, with no generation of secondaries

c    HADR 3      FLUKA (with GHEISHA for neutrons below 20MeV)

c    HADR 4      FLUKA (with MICAP for neutrons below 20MeV)

HADR 1


c The following cards are needed if optical photons are being

c being generated and tracked in the simulation.  The CKOV directive

c enables Cerenkov generation in materials for which the refractive

c index table has been specified.  The LABS card enables absorption

c of optical photons.  The ABAN directive controls a special feature

c of Geant which allows it to "abandon" tracking of charged particles

c once their remaining range drops below the distance to the next

c discrete interaction or geometric boundary.  Particles abandoned

c during tracking are stopped immediately and dump all remaining energy

c where they lie.  The remaining energy is dumped in the correct volume

c so this is OK in most cases, but it can cut into the yield of

c Cerenkov photons (eg. in a lead glass calorimeter) at the end of

c a particle track.  If this might be important, set ABAN to 0.

CKOV 1

LABS 1


c The following card prevents GEANT tracking code from abandoning the

c tracking of particles near the end of their range, once it determines

c that their fate is just to stop (i.e. electrons and protons).  This

c behaviour is normal in most cases, but in the case of Cerenkov light

c generation it leads to an underestimate for the yields.

c    ABAN 1      abandon stopping tracks (default)

c    ABAN 0      do not abandon stopping tracks

ABAN 0


c The following card sets up the simulation to perform debugging on

c a subset of the simulated events.

c DEBUG first last step

c  - first (int) = event number of first event to debug

c  - last (int) = event number of last event to debug
```

```
c  - step (int) = only debug one event every step events
DEBUG 1 10 1000


c The following card can be used to turn off generation of secondary
c particles in the simulation, ordinarily it should be 0 (or omitted).
NOSECONDARIES 0


c The following card tells the simulation to store particle trajectories
c in the event output stream.  This output can be verbose, use with caution.
c The value set here determines the amount of output recorded:
c
c TRAJECTORIES = 0  don't store trajectory info
c TRAJECTORIES = 1  store birth and death points of primary tracks
c TRAJECTORIES = 2  store birth and death points of all particles
c TRAJECTORIES = 3  store full trajectory of primary tracks
c TRAJECTORIES = 4  store full trajectory of primary tracks and birth/death points of secondaries
c TRAJECTORIES = 5  store full trajectory for all particles
c
TRAJECTORIES 0


c The following tracking parameters are defined for each tracking medium
c    TMAXFD (REAL) maximum angular deviation due to the magnetic field
c                  permitted in one step (degrees)
c    DEEMAX (REAL) maximum fractional energy loss in one step (0< DEEMAX <=0.1)
c    STEMAX (REAL) maximum step permitted (cm)
c    STMIN  (REAL) minimum value for the maximum step imposed by energy loss,
c                  multiple scattering, Cerenkov or magnetic field effects (cm)
c Normally they are assigned appropriate values calculated automatically by
c Geant when the geometry is defined, overwriting the values declared by
c the user code in the GSTMED() call.  Users who know what they are doing can
c force Geant to instead use the values passed in the arguments to GSTMED()
c by removing the comment in front of the following card.  Any parameters with
c zero values are still assigned automatic values even when AUTO is turned off.
cAUTO 0


END
```

Bibliography

[1] F. E. Close. Gluonic Hadrons. *Rep. Prog. Phys.*, 51:833, 1988.

[2] M. Fritzch, M. Gell-Mann, and H. Leutwyler. *Phys. Lett.*, 47B:365, 1971.

[3] D. J. Gross and F. Wilczek. *Phys. Rev.*, D8:3497, 1973.

[4] S. Weinberg. *Phys. Rev. Lett.*, 31:494, 1973.

[5] G. Zweig. CERN preprint 8419/TH.412; 8182/TH.401, 1964.

[6] M. Gell-Mann. Schematic Model Of Baryons And Mesons. *Phys. Lett.*, 8:214, 1964.

[7] R. Gupta. Introduction to lattice QCD. *arXiv:*, hep-lat:9807028, 1998.

[8] S. Capitani. Lattice Perturbation Theory. *arXiv:*, hep-lat:0211036, December 2002.

[9] V.E. Barnes et al. Observation of a Hyperon with Strangeness Number Three. *Physical Review Letters*, 12 (8):204, 1964.

[10] R.L. Jaffe and K. Johnson. *Phys. Lett.*, 60B:201, 1976.

[11] T. Barnes, editor. *The Exotic Atoms of QCD: Glueballs, Hybrids and Baryonia.* School of Physics of Exotic Atoms, 1984.

[12] T. Barnes, editor. *The Bag Model and Hybrid Mesons*, SIN School of Strong Interactions, Zuoz Switzerland, 1985.

[13] M. Chanowitz. *Phys. Lett.*, B132:413, 1983.

[14] M. Chanowitz. *Nucl. Phys.*, B222:211, 1983.

[15] S.-U. Chung, editor. *S. Godfrey , An Overview of Hybrid Meson Phenomenology*, Upton, New York, 1989. BNL Workshop on Glueballs,Hybrids, and Exotic Hadrons, AIP.

[16] S.-U. Chung, editor. *N. Isgur, Hadron Spectroscopy: An Overview with Strings Attached*, Upton, New York, 1989. BNL Workshop on Glueballs, Hybrids, and Exotic Hadrons, AIP.

[17] T. Barnes. *unpublished*. PhD thesis, Caltech, 1977.

[18] T. Barnes, F. E. Close, and F. de Viron. *Nucl. Phys.*, B224:241, 1983.

[19] D. Horn and J. Mandula. *Phys. Rev.*, D17:898, 1978.

[20] N. Isgur and J. Paton. *Phys. Lett.*, B124:247, 1983.

[21] N. Isgur and J. Paton. *Phys. Rev.*, D31:2910, 1985.

[22] N. Isgur, R. Kokoski, and J. Paton. *Phys. Rev. Lett*, 54:869, 1985.

[23] J.L. Latorre et al. *Phys. Lett.*, 147B:169, 1984.

[24] G. Bali, K. Schilling, A. Hulsebos, A. Irving, C. Michael, and P. Stephenson. *Phys. Lett.*, B309:378, 1993.

[25] C. Michael. Proceedings of the Seventh International Conference on Hadron Spectroscopy. page p. 657, New York, August 1998. Brookhaven National Laboratory, AIP Conference Proceedings 432, Woodbury New York.

[26] A. Vaccarino and D. Weingarten. unpublished, 1998.

[27] C. Morningstar and Peardon. *Phys. Rev.*, D56:4043, 1997.

[28] K. Chen, J. Sexton, A. Vaccarino, and D. Weingarten. *Nucl. Phys. B. (Proc. Suppl)*, 34:357, 1994.

[29] D. V. Bugg, M. Peardon, and B. S. Zou. The Glueball Spectrum. *Physics Letters B*, 486:49–53, July 2000.

[30] F.E. Close and A. Kirk. Scalar glueball- mixing above 1 GeV and implications for lattice QCD. *The European Physical Journal C*, 21:531, 2001.

[31] S. Godfrey and J. Napolitano. Light meson spectroscopy. *Rev. Mod. Phys.*, 71:1411, 1999.

[32] T. Barnes and F. E. Close. *Phys. Lett.*, B123:89, 1983.

[33] T. Barnes and F. E. Close. *Phys. Lett.*, B128:277, 1983.

[34] P.R. Page. *Phys. Lett.*, B401:313, 1997.

[35] P.R. Page. *Phys. Lett.*, B402:183, 1997.

[36] Yu. S. Kalashnikova. *Z. Phys.*, C62:323, 1994.

[37] F. E. Close and P. Page. *Nucl. Phys.*, B443:233, 1995.

[38] C.A. Meyer. GlueX-doc-380-v2, A Summary of Hybrid Masses and Decays. Technical report, The GlueX Collaboration, 2004.

[39] F. E. Close and J. J. Dudek. Forbidden' decays of hybrid mesons to $\pi\rho$ can be large. *Phys. Rev. D*, 70(9):094015, Nov 2004.

[40] P. Lacock et al. *Phys. Lett. B*, 401:309, 1997. `hep-lat/9611011`.

[41] C. Bernard et al. *Phys. Rev. D*, 56:7039, 1997.

[42] C. Bernard et al. Exotic meson spectroscopy from the clover action at $\beta = 5.85$ and 6.15. *Nucl. Phys. B(Proc. Suppl.)*, 73:264, 1999. `hep-lat/9809087`.

[43] P. Lacock and K. Schilling. Hybrid and Orbitally Excited Mesons in Full QCD. *Nucl. Phys. Proc. Suppl.*, 73:261, 1999. (SESAM Collaboration), `hep-lat/9809022`.

[44] Zhong-Hao Mei and Xiang-Qian Luo. Exotic mesons from quantum chromo-dynamics with improved gluon and quark actions on the anisotropic lattice. *Nucl. Phys. Proc. Suppl.*, 119:263, 2003. `hep-lat/0206012`.

[45] C. Bernard, T. Burch, C. DeTar, Steven Gottlieb, E.B. Gregory, U.M. Heller, J. Osborn, R. Sugar, and D. Toussaint. *Phys. Rev. D*, 68:074505, 2003.

[46] G. Adams et al. *Submitted to Phys. Rev. Lett.*, 1998. E852 Collaboration.

[47] G. M. Beladidze et al. *Phys. Lett.*, B313:276, 1993. VES Collaboration.

[48] J.R. Sanford, editor. *Gouz, Yu.P.*, volume p.572, Dallas, 1993. Proc. of the 26th ICHE.

[49] S. Fukui et al. *Phys. Lett.*, B267:293, 1991.

[50] H. Aoyagi et al. *Phys. Lett.*, B314:246, 1993.

[51] D. Aston et al. *Phys. Lett.*, B215:199, 1988. LASS Collaboration.

[52] F. E. Close and P. Page. *Phys. Rev.*, D52:1706, 1995.

[53] F. P. Sassen, S. Krewald, and J. Speth. Meson model for f0(980) production in peripheral pion-nucleon reactions. *Phys. Rev. D*, 6:036003, 2003.

[54] N. Isgur, R. Kokoski, and J. Paton. *Phys. Rev. Lett.*, 54:869, 1985.

[55] A. Afanasev and P. Page. *Phys. Rev.*, D57:6771, 1998.

[56] A. Dzierba. GlueX-doc-856, Comparing PYTHIA simulation with photoproduction data at 9 GeV. Technical report, GlueX Collaboration, 2007.

[57] H. H. Bingham et al. Total and partial γp cross sections at 9.3 GeV. *Phys. Rev.*, D8:1277–1286, 1973.

[58] J. Ballam et al. Vector meson production by polarized photons at 2.8, 4.7 and 9.3 GeV. *Phys. Rev.*, D7:3150–3177, 1973.

[59] Y. Eisenberg et al. Photoproduction of ω mesons from 1.2 to 8.2 GeV. *Phys. Lett.*, B34:439–442, 1971.

[60] Y. Eisenberg et al. Study of high energy photoproduction with positron-annihilation radiation. I. Three-prong events. *Phys. Rev.*, D5:15–38, 1972.

[61] G. Alexander et al. Study of high energy photoproduction with positron-annihilation radiation. II. The reaction $\gamma p \rightarrow p\pi^+\pi^+\pi-\pi^-$. *Phys. Rev.*, D8:1965–1978, 1973.

[62] G. Alexander et al. Study of high energy photoproduction with positron-annihilation radiation. III. The reactions $\gamma p \rightarrow p2\pi^+2\pi\pi^0$ and $\gamma p \rightarrow n3\pi^+2\pi^-$. *Phys. Rev.*, D9:644–648, 1974.

[63] A.R. Dzierba. GlueX-doc-835-v1, A Summary of Photoproduction Data in the GlueX Energy Regime. Technical report, The GlueX Collaboration, 2007.

[64] A. Baldini, V. Flaminio, W. G. Moorhead, and D. R. O. Morrison. *Total Cross Sections for Reactions of High Energy Particles, , vol. 12b of Numerical Data and Functional Relationships in Science and Technology.* Springer-Verlag, 1988. the pages on photon induced reactions are available on the GlueX portal as GlueX-doc-809.

[65] T. H Bauer, R. D. Spital, D. R. Yennie, and F. M. Pipkin. *Rev. Mod. Phys.*, 50:261, 1978. Erratum, 1979, Rev. Mod. Phys. **51**, 407.

[66] P. Szczepaniak and M. Swat. *Phys. Lett.*, B516:72, 2001.

[67] K. Peters. A Primer on Partial Wave Analysis. *arXiv:*, hep-ph:0412069v1, 2004.

[68] S. Chung. Formulas for partial-wave analysis. *note (BNL)*, 1988. (BNL).

[69] S. Chung and T. Trueman. Positivity conditions on the spin density matrix: A simple parametrization. *Physical Review D*, 11 (3):633, 1975.

[70] J. P. Cummings and D. P. Weygand. An Object-Oriented Approach to Partial Wave Analysis. *ArXiv Physics e-prints*, September 2003.

[71] C. A. Meyer. GlueX-doc-666-v1, Likelihood Fitting. Technical report, The GlueX Collaboration, 2006.

[72] R. Mitchel. GlueX-doc-591-v1, Analysis of E852 Data at Indiana University. Technical report, The GlueX Collaboration, 2006.

[73] M. Shepherd. GlueX-doc-1420-v1, Using GPUs for GlueX PWA. Technical report, The GlueX Collaboration, 2010.

[74] The Gluex Collaboration.

[75] H. Grunder. CEBAF Commissioning and Future Plans. Technical report, Proceedings of PAC95. p. 1-3.

[76] The Science Driving the 12 GeV Upgrade of CEBAF. Technical report, Jefferson Lab, 2001.

[77] J. Stewart. GlueX-doc-1127-v4. Technical report, The GlueX Collaboration, 2009.

[78] A. P. Szczepaniak and A. Afanasev. *hep-ph/9910268*, 1999.

[79] C. A. Meyer. Angular Distributions for the PWA Study. Technical report, The GlueX Collaboration, 2000.

[80] GlueX/Hall D Collaboration. The Science of Quark Confinement and Gluonic Excitations, GlueX/Hall D Design Report, Ver.4. Technical report, 2002.

[81] C. A. Meyer et al. GlueX-doc-1063-v4, Physics and Detector Performance Metrics for the GlueX Experiment. Technical report, The GlueX Collaboration, 2008.

[82] David Lawrence. M.C. Studies of GlueX Solenoidal Field. Technical report, GlueX Collaboration, 2009.

[83] C. A. Meyer and Yves van Haarlem. GlueX-doc-990-v11, The GlueX Central Drift Chamber. Technical report, GlueX Collaboration, 2008.

[84] H. Wirth et al. Particle Identification with the JETSET Straw Chambers. *Nucl. Instrum. Methods*, A367:248, 1995. The JETSET Collaboration.

[85] D. S. Carman and S. Taylor. GlueX-doc-754-v10, The GlueX Central Drift Chamber. Technical report, GlueX Collaboration, 2007.

[86] A. R. Dzierba, M. Shepherd, and B. Zihlmann. GlueX-doc-988-v1, FCAL – The Forward Calorimeter (GlueX/Hall D Calorimeter Conceptual Design Report). Technical report, GlueX Collaboration, 2008.

[87] A. R. Dzierba. GlueX-doc-873-v1 Overview of the BNL E852 Experiment. Technical report, GlueX Collaboration, 2007.

[88] J. V. Jelley. *Br. J. Appl. Phys.*, 6:227–232, 1955.

[89] A. Brunner et al. A Cockcroft-Walton base for the FEU84-3 photomultiplier tube. *Nucl. Instrum. Meth.*, A414:466–476, 1998.

[90] J. Dickey, E. Scott, M. Shepherd, P. Smith, and S.Teige. GlueX-doc-657-v1. Temperature dependence of FEU84-3 PMT's and IU Cockcroft-Walton bases. Technical report, GlueX Collaboration, 2006.

[91] M. Adinolfi et al. *Nucl. Instr. Meth.*, A461:344, 2001.

[92] M. Adinolfi et al. *Nucl. Instr. Meth.*, A482:364, 2002.

[93] M. Adinolfi et al. *Nucl. Instr. Meth.*, A494:326, 2002.

[94] T. Sjöstrand, S. Mrenna, and P. Skands. Pythia 6.4 Physics and Manual. Technical report, Lund University, 2006.

[95] GEANT 3.21 Detector Description and Simulation Tool. Technical report, CERN Program Library Long Writeup, W5013, Geneva, 1993.

[96] R. Wigmans. *Nucl. Instr. Meth.*, A494:277, 2002.

[97] Z. Papandreou. GlueX-doc-840-v2. Technical report, GlueX Collaboration, 2007.

[98] Scintillating Optical Fibers Brochure 605. Technical report, St. Gobain Crystals, Paris, France.

[99] C.P. Achenbach. *arXiv:*, nucl-ex/0404008v1, 2004.

[100] Z. Papandreou. GlueX-doc-918-v2. Technical report, GlueX Collaboration, 2007.

[101] G. Koleva. GlueX-doc-824-v2. Master's thesis, U. of Regina, 2006.

[102] B.D. Leverington. GlueX-doc-827-v3. Technical report, GlueX Collaboration, 2007.

[103] M.J. Berger and S.M. Seltzer. Tables of energy losses and ranges of electrons and positrons. Technical report, NASA, Washington, DC, 1964.

[104] B. Rossi. *High Energy Particles*. Prentice-Hall, Inc., Englewood Cliffs, NJ, 1952.

[105] A. Dzierba. Introduction to the PID discussion and status of TOF for the March 2007 GlueX meeting. Technical report, The GlueX Collaboration, 2007.

[106] F.J. Barbosa. GlueX-doc-747-v15, Summary of Hall D Detector Systems. Technical report, GlueX Collaboration, 2009.

[107] E. Chudakov and A. Somov. GlueX-doc-1043-v1. Technical report, The GlueX Collaboration, 2008.

[108] P. Achenbach and J. H. Cobb. Computational studies of light acceptance and propagation in straight and curved multimodal active fibres. *arXiv:*, nucl-ex:0606024v1, 2006. J.Opt. A5 (2003) 239-249.

[109] R.J. Potter, E. Donath, and R. Tynan. Light-collecting properties of a perfect circular optical fiber. *Opt. Soc. Am.*, 53:256–260, 1963.

[110] A.J. Davis et al. *Nucl. Instr. and Meth.*, A276:347, 1989.

[111] Yu.G. Kudenko, L.S. Littenberg, V.A. Mayatski, O.V. Mineev, and N.V. Yershov. *Nucl. Instr. and Meth.*, A469:340, 2001.

[112] C.P. Achenbach. *arXiv*, nucl-ex/0404008 v1, 2004.

[113] A. Pla-Dalmau. 2-(2'-Hydroxyphenyl)benzothiazoles, -benzoxazoles, and -benzimidazoles for plastic scintillation applications. *The Journal of Organic Chemistry*, 60:5468–5473, 1995.

[114] J.B. Birks. *The Theory and Practice of Scintillation Counting.* Pergamon Press, New York, 1964.

[115] T. Förster. *Discuss. Faraday Soc.*, 27:7, 1959.

[116] R.C. Ruchti. *Ann. Rev. Nucl. Part. Sci.*, 46:281, 1996.

[117] Z. Papandreou, B.D. Leverington, and G.J. Lolos. Spectral response of scintillating fibers. *Nuclear Instruments and Methods in Physics Research Section A: Accelerators, Spectrometers, Detectors and Associated Equipment*, 596(3):338 – 346, 2008.

[118] J. E. Moyal. *Phil. Mag.*, 46:263, 1955.

[119] G. Drexlin, V. Eberhard, D. Hunkel, and B. Zeitnitz. *Nucl. Instr. and Meth.*, A360:245, 1995.

[120] L. Archambault et al. *Med. Phys.*, 32 (7):2271, 2005.

[121] K.V. Alexandrov et al. *Nucl. Instr. and Meth.*, A459:123, 2001.

[122] H. Gast et al. *arXiv:*, 0711.4694v1, Nov 2007.

[123] B.D. Leverington et al. GlueX-doc-1071-v1. Technical report, The GlueX Collaboration, 2007. submitted to Nucl. Instr. and Meth. A (2008).

[124] A. Antonelli et al. *Nucl. Instr. and Meth.*, A370:367, 1996.

[125] W.T. Welford and R. Winston. *The Optics of Nonimaging Concentrators.* Academic Press, 1978.

[126] Eric W. Weisstein. Eric Weisstein's World of Physics, http://scienceworld.wolfram.com/physics/WinstonCone.html.

[127] D.I. Sober et al. *Nucl. Instr. Meth.*, A440:263, 2000.

[128] F.J. Barbosa, E. Jastrzembski, J. Profitt, and J. Wilson. In *Nuclear Science Symposium Conference Record, 2002 IEEE*, volume 1 of *1:135-139*, pages 10–16, 2002.

[129] A. Antonelli et al. *Nucl. Instr. Meth.*, A354:352, 1995.

[130] A. Antonelli et al. *Nucl. Instr. Meth.*, A379:511, 1996.

[131] M. Shepherd and B. Leverington. Internal email to GlueX Collaboration.

[132] C. Zorn. GlueX-doc-1406-v1, Evaluation Summary for Hamamatsu and SensL Ceramic Arrays. Technical report, The GlueX Collaboration, 2010. GlueX January 2010 Collaboration Meeting.

[133] H. Dong et al. Integrated tests of a high speed VXS switch card and 250 MSPS flash ADCs. In NSS '07. IEEE, editor, *Nuclear Science Symposium Conference Record*, volume 1, pages 831–833, Oct. 2007.

[134] A. Semenov. GlueX-doc-1069. Number of photoelectrons measured with the SiPMPlus-array and Module 2. Technical report, The GlueX Collaboration, 2008.

[135] M. Barbi, G. M. Huber, Z. Papandreou, and C. Xu. GlueX-doc-569-v1, The GlueX BCAL Reconstruction Code - Preliminary Results. Technical report, The GlueX Collaboration, 2007.

[136] A. R. Dzierba. GlueX-doc-644-v1, FCAL - Status and Plans. Technical report, The GlueX Collaboration, 2006.

[137] C.A. Meyer. GlueX-doc-989-v1. Calorimeter Final Design and Safety Review Section 5: Calorimeter Simulations. Technical report, GlueX Collaboration, 2008.

[138] D. Lawrence. GlueX-doc-1004, Track Finding and Fitting in GlueX: Development Report IV. Technical report, The GlueX Collaboration, 2008.

[139] A. Antonelli et al. Performance of fine mesh photomultiplier tubes in magneticfields up to 0.3-T. *Nucl. Instrum. Meth.*, A368:628–634, 1996.

[140] P. Eugenio. GlueX-doc-11-v1, *Genr8*: A general monte carlo event generator. Technical report, Carnegie Mellon University, 1998.

[141] J. M. Laget and R. Mendez-Galain. Exclusive photo- and electroproduction of vector mesons at large momentum transfer. *Nuclear Physics A*, 581:397–428, 1995.

[142] T. Mibe et al. *Phys. Rev. Lett. C*, 95:182001, 2005. (LEPS Collaboration).

[143] M. Shepherd. AmpTools: a collection of libraries that is useful for doing amplitude analysis. Indiana University.

[144] C. Amsler et al. Particle data group. *Phys. Lett. B*, 667:1, 2008.

[145] J. Ballam et al. γp interactions at 5.25 GeV. *Physics Letters B*, Volume 30 Issue 6:421–425, 1969.

[146] Open Science Grid: A distributed computing grid for data intensive research. http://www.opensciencegrid.org/.

[147] M. Williams and C.A. Meyer. CLAS note 03-017, Kinematic Fitting in CLAS. Technical report, 2003. http://www.jlab.org/Hall-B/notes/clas_notes03.html.